Fluid Flows and Boundaries on Logarithmic Lattices

PhD Thesis

by
Ciro Sobrinho Campolina Martins

Advisor: Alexei A. Mailybaev

Instituto de Matemática Pura e Aplicada (IMPA)

Rio de Janeiro, November 2022

A thesis submitted in fulfilment of the requirements for the degree of Philosophy Doctor at the Insituto de Matemática Pura e Aplicada (IMPA).

Approved on November 30, 2022, by the committee:

Prof. Alexei Mailybaev (Instituto de Matemática Pura e Aplicada, advisor)

Prof. André Nachbin (Instituto de Matemática Pura e Aplicada)

Prof. Bérengère Dubrulle (Université Paris-Saclay)

Prof. Fábio Ramos (Universidade Federal do Rio de Janeiro)

Prof. Luca Biferale (Università degli Studi di Roma Tor Vergata)

Prof. Simon Thalabard (Université Côte d'Azur, Nice)

Tuus totus ego sum, et omnia mea tua sunt,
o Virgo super omnia benedicta

Acknowledgements

I would like to express my deepest gratitude to the One and Triune God: the Father, the Son and the Holy Spirit. I also extend my greatest acknowledgments to the Virgin Mary, Mother of God, whose constant assistance was fundamental for this accomplishment, especially during the most difficult times of my bad health condition. Totus tuus Mariæ.

I am deeply grateful to my advisor, Alexei Mailybaev, for his close guidance and friendship during my whole graduate program.

I thank Luca Biferale, Bérengère Dubrulle, Marie Farge, Uriel Frisch and Simon Thalabard for the useful discussions and suggestions on this work.

I thank André Nachbin and Fabio Ramos for the comments on this manuscript.

I thank Bérengère Dubrulle and her team for the warm reception in Saclay. The financial support from CEA during my visit is also greatly acknowledged.

I thank the Fluid Dynamics group of IMPA, for the stimulating research environment.

To my grandmother, Selma, for the lovely home during most of my stay in Rio.

To my parents Antonio Henrique and Claudia, and my brothers Joana, André and Antônio, for their constant support during my whole journey.

To my wife, Luíza, for all her love and friendship. I hope this work is just one brick out of many that we are going to use in building our home.

To Tiago, Cintya and Matheus, for welcoming me as part of their beautiful family.

To Fr. Rafael Martins, for his spiritual guidance.

Finally, I would like to thank CNPq and FAPERJ for the financial support.

Abstract

Several open problems in fluid dynamics are related to the multi-scale nature of turbulence and the effects of boundary conditions. To overcome the limited resolution of direct numerical simulations, simplified toy-models are commonly employed in the study of large spatial range flows. In the construction of such models, one modifies equations of motion, preserving only certain parts believed to be important. In this thesis, we propose a different approach. Instead of simplifying equations, one introduces a simplified configuration space: we define velocity fields and boundary effects on multi-dimensional logarithmic lattices in Fourier space. Operations upon these variables are provided in a rigorous mathematical framework, so equations of motion are written in their exact original form. As a consequence, the resulting models preserve the same symmetry groups, inviscid invariants and regularity properties. The strong reduction in degrees of freedom allows computational simulations of incredibly large spatial ranges. Using the new simplified models, we address two important open problems: the finite time singularities in ideal flow and the vanishing viscosity limit in the presence of solid boundaries. We observe strong robustness of the chaotic blowup scenario in the three-dimensional incompressible Euler equations and promising results towards the investigation of potentially singular behavior close to solid boundaries.

Table of contents

Chapter 1

Introduction

Multi-scale nonlinear flows and, in particular, *turbulence* are everywhere. We encounter turbulent flows in our daily lives, when, for example, we mix milk with coffee on a cup—see Fig. 1.1(a). But the same phenomenon is present in the atmosphere of planets and even in the formation of galaxies—Fig. 1.1(b). A number of industrial applications and technological products, such as aircraft aerodynamics, chemical mixers and combustion engines, are related to turbulent motion. Despite its ubiquity, turbulence remains as one of the major unsolved problems of Classical Physics.

One of the greatest challenges in turbulence lies on how to recover its phenomenological theory from first dynamical principles, or, in other words, from the governing equations of Fluid Dynamics.

1.1 Turbulence, energy dissipation and flow regularity

It is widely accepted that simple fluids are described by the *incompressible Navier-Stokes equations*, which in dimensionless form read

$$\partial_t \mathbf{u} + \mathbf{u} \cdot \nabla \mathbf{u} = -\nabla p + \frac{1}{Re} \Delta \mathbf{u}, \quad \nabla \cdot \mathbf{u} = 0, \tag{1.1}$$

where $\mathbf{u} = (u_1, u_2, u_3)$ is the velocity field and p is the scalar pressure; Re is the Reynolds number defined as $Re = UL/\nu$, where U and L are characteristic velocity and length of the flow, respectively, and $\nu \geq 0$ is the kinematic viscosity. The divergence free condition $\nabla \cdot \mathbf{u} = 0$ is the mathematical translation of flow incompressibility. The viscous force $\frac{1}{Re}\Delta \mathbf{u}$ has the form of a diffusion term and contributes to flow

(a) (b)

Fig. 1.1 Ubiquity of turbulence. (a) Turbulent mixing of milk with coffee. The largest scale of motion has the size of the cup. (b) The Great Red Spot, a persistent high-pressure region in the atmosphere of Jupiter producing an anticyclonic turbulent storm. The size of this region has the approximate diameter of the earth.

regularization. For small Re, the diffusion term is dominant and the flow is smooth and regular. As Re increases, the nonlinearities prevail, and the fluid motion becomes more chaotic and unpredictable. In this setting, *ideal turbulence* is usually associated to the *infinite Reynolds limit* $Re \to \infty$, or equivalently the *vanishing viscosity limit* $\nu \to 0$.

When the viscosity is set to zero, $\nu = 0$, the equations (1.1) become

$$\partial_t \mathbf{u} + \mathbf{u} \cdot \nabla \mathbf{u} = -\nabla p, \quad \nabla \cdot \mathbf{u} = 0, \tag{1.2}$$

and are referred to as the *incompressible Euler equations*. The flow is said to be *ideal*, since the viscous dissipative term is dropped. In fact, smooth solutions $\mathbf{u}$ of this system conserve the energy $E = \frac{1}{2}\int |\mathbf{u}|^2 d\mathbf{x}$ in time.

By regarding equations (1.2) as the limit case $Re \to \infty$ of the Navier-Stokes system, the Euler equations are expected to describe the dynamics of turbulent flows. However, an experimental fact apparently defies this intuitive idea: the energy dissipation $\varepsilon = \nu|\nabla \mathbf{u}|^2$ seems to not vanish in the limit $\nu \to 0$ [87, 127], a phenomenon known as *anomalous dissipation*—see Fig. 1.2(a). Since for small viscosities is typical to have injection of energy concentrated at large scales and energy dissipation restricted to small scales, a dissipation anomaly is related to the development of a constant energy flux in the intermediate scales, a fact confirmed by numerical simulations—see Fig. 1.2(b).

This residual dissipation in the vanishing viscosity limit might look paradoxical at first sight, since the Euler equations constitute a conservative system. Nevertheless,

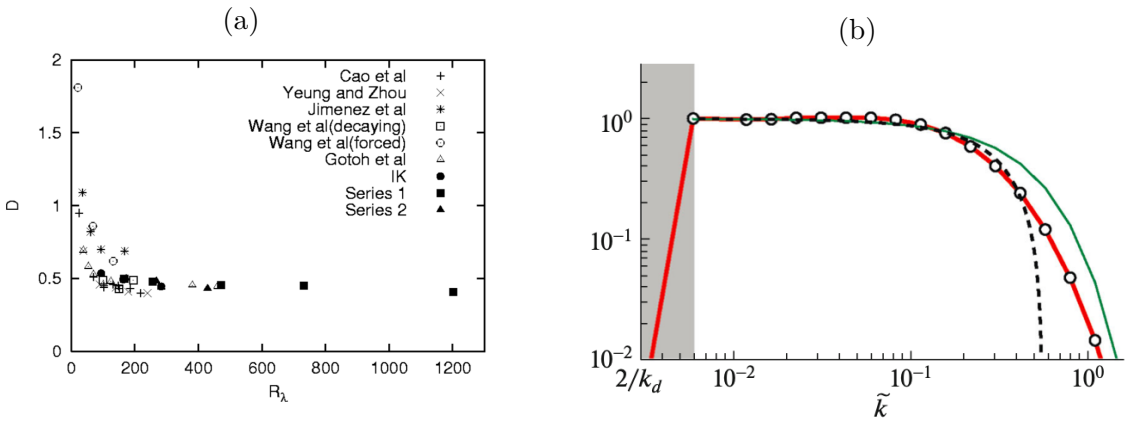

Fig. 1.2 Experiments and numerics of anomalous dissipation. (a) Normalized energy dissipation rate $D = \langle\varepsilon\rangle L/U^3$ versus Taylor microscale Reynolds number R_λ from numerical experiments. The energy dissipation attains a nonzero value in the limit $R_\lambda \to \infty$. Figure reproduced from [87]. (b) Normalized energy flux $\tilde{\Pi}(\tilde{k})$ along normalized wave number $\tilde{k}$ from DNS (in red) and some inertial range prediction models (in green and black dashed lines). The energy flux becomes constant in the inertial range, which extends to higher $\tilde{k}$'s as the Reynolds number increases. Figure reproduced from [154].

Onsager [125, 64] was the first to notice that Euler solutions need not to conserve energy if they are not sufficiently regular. He conjectured that non-vanishing energy dissipation in high-Reynolds-number turbulence is associated to singular (distributional) solutions of the incompressible Euler equations, a statement under active research nowadays [63, 38, 20, 85, 21]. Thus, Onsager linked the physical feature of anomalous dissipation in turbulent flows to the mathematical regularity of Euler solutions. Accordingly, aiming a deep understanding of turbulence, one may ask how regular are the solutions of the Euler equations, or, more precisely, if an Euler flow is able to maintain its regularity as time evolves.

To discuss the regularity of Euler solutions, it is usefull to introduce the *vorticity field* $\boldsymbol{\omega} = \nabla \times \mathbf{u}$. If we take the curl of equations (1.2), one obtains, after some manipulations, a dynamical equation for the vorticity field

$$\partial_t \boldsymbol{\omega} + \mathbf{u} \cdot \nabla \boldsymbol{\omega} = \boldsymbol{\omega} \cdot \nabla \mathbf{u}, \tag{1.3}$$

usually called the *Helmholtz equation*.

In a 2D flow, the vorticity is perpendicular to the plane of motion, and therefore equations (1.3) reduce to the advection equation

$$\frac{D\boldsymbol{\omega}}{Dt} := \partial_t \boldsymbol{\omega} + \mathbf{u} \cdot \nabla \boldsymbol{\omega} = 0, \tag{1.4}$$

where the material derivative $D\boldsymbol{\omega}/Dt$ represents the variation of the vorticity field along particle trajectories. The simpler equations (1.4) preserve the enstrophy of the flow, defined as $\Omega = \frac{1}{2}\int |\boldsymbol{\omega}|^2 d\mathbf{x}$, half of L^2 norm of the vorticity field. Taking advantage of this fact, one proves global-in-time regularity for the solutions of the 2D equations [156, 113].

However, due to the presence of the nontrivial nonlinear term on the left-hand side of (1.3), the 3D case establishes a completely different scenario. The flow does not preserve the enstrophy anymore and, thus, the arguments of global regularity used in the 2D equations are no longer valid.

1.1.1 Blowup in ideal flow

The question about the regularity of 3D Euler solutions is partially answered by the many local-in-time existence theorems, *e.g.*, [102, 57, 88, 147]. They assert that if the velocity field is initially smooth at $t = 0$, then it remains smooth up to a certain finite time $T > 0$ depending on the initial data. However, we know little about the solution beyond this particular instant. What could prevent the solution from being smoothly extended for all times is the development of a singularity in finite time, *i.e.*, the loss of regularity at a certain instant $t_b > 0$. Such event is called *finite-time blowup*, or simply *blowup*, and the time instant t_b at which it occurs is the blowup time. The name is motivated by the fact that some norm, related to the degree of regularity of the field, becomes arbitrarily large ("blows up") as t approaches t_b.

One of the problems we address in this thesis is:

(P.I) Blowup problem in ideal flow. *Does there exist a regular solution of the 3D incompressible Euler equations* (1.2) *that becomes singular (blows up) in a finite time?*

The existence of blowup in incompressible ideal flow is a long-standing open problem both for physics and mathematics. On the physical side, such blowup is anticipated by Kolmogorov's theory of developed turbulence [69], predicting that the vorticity field diverges at small scales as $\delta\omega \sim \ell^{-2/3}$, while the time of energy transfer between the integral and viscous scales remains finite in the inviscid limit, $\nu \to 0$. In this context,

the blowup would reveal an efficient mechanism of energy transfer from large to small scales.

From the mathematical perspective, the inkling of blowup comes from the quadratic nonlinearity of the Euler equations. It is heuristically argued [10] that, if we identify the velocity gradient to the vorticity $\nabla \mathbf{u} \approx \boldsymbol{\omega}$ in the Helmholtz equation (1.3), one obtains a quadratic equation for the vorticity

$$\frac{D\omega}{Dt} \approx \omega^2. \tag{1.5}$$

Equation (1.5) is the common textbook example of an ordinary differential equation that blows up in finite time. Its solution for initial data $\omega(t=0) = \omega_0 > 0$ is given by

$$\omega(t) = \frac{1}{t_b - t}, \quad t_b = \omega_0^{-1}, \tag{1.6}$$

which grows to infinity as t approaches the blowup time t_b, *i.e.*,

$$\omega(t) \to \infty, \text{ as } t \to t_b. \tag{1.7}$$

The above argument is far from rigorous, but it displays some true features of possible singularities in the Euler equations. Indeed, the finite-time blowup is characterized by the spontaneous development of infinitely large vorticity, as established by the following

Theorem 1.1 (Beale-Kato-Majda Theorem [6])**.** *Let* $\mathbf{u}$ *be a smooth solution of the Euler equations and suppose there is a time* t_b *such that the solution cannot be smoothly continued to* $t = t_b$*; assume that* t_b *is the first such time. Then*

$$\int_0^{t_b} ||\boldsymbol{\omega}(\cdot, s)||_\infty ds = \infty, \tag{1.8}$$

and in particular

$$\limsup_{t \nearrow t_b} ||\boldsymbol{\omega}(\cdot, t)||_\infty = \infty. \tag{1.9}$$

The Beale-Kato-Majda Theorem has two important consequences. First, it shows that the maximum vorticity controls the blowup. Second, if the maximum vorticity diverges with the assymptotic behavior

$$||\boldsymbol{\omega}(\cdot, t)||_\infty \sim (t_b - t)^{-\beta}, \tag{1.10}$$

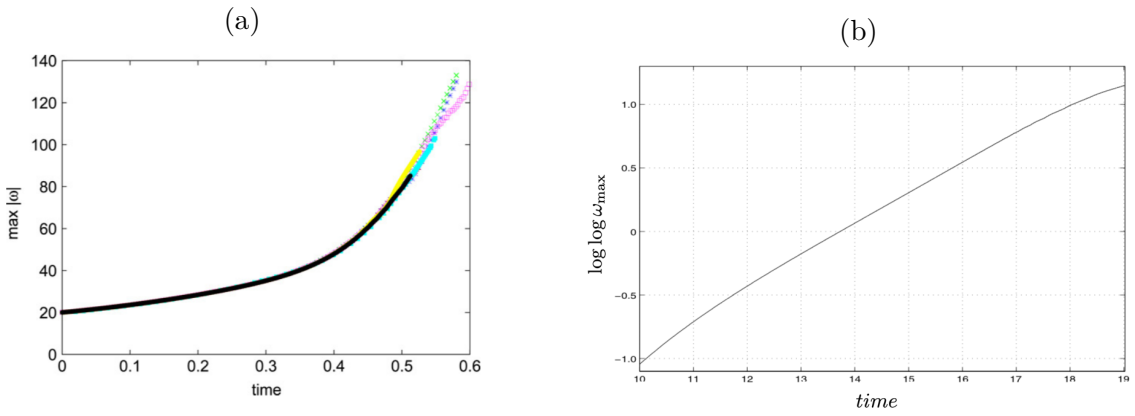

Fig. 1.3 Direct numerical simulations of the three-dimensional incompressible Euler equations. (a) Growth of maximum vorticity for different numerical schemes. Figure reproduced from [76]. (b) Plot of $\log\log\omega_{\max}$ versus time, obtained from DNS at resolution $1536 \times 1024 \times 3072$. The growth is not greater than double exponential for the whole simulation. Figure reproduced from [82].

then, for the integral (1.8) to diverge, we must necessarily have $\beta \geq 1$. Clearly, from dimensional analysis, we expect the equality to hold, *i.e.*, $\beta = 1$, since the vorticity field has dimension of inverse time. Nevertheless, we remark that Theorem 1.1 is a conditional statement: it characterizes the possible singularities in the Euler equations, but it does not claim them to happen.

With such criterion in hand, it is appealing to look for a plausible singularity formation through numerical simulations. Indeed, the unique quantity that needs to be tracked is the maximum vorticity, while the theorem also constraints how it should behave in the case of blowup. We briefly review the numerical investigations now.

Direct Numerical Simulations

Besides purely mathematical studies, *e.g.*, [6, 33, 146], a crucial role in the blowup analysis is given to direct numerical simulations (DNS). The chase after numerical evidence of blowup in the 3D incompressible Euler equations has a long history [72]. Most early numerical studies were in favor of blowup, *e.g.* [134, 91, 77]. But the increase of resolution owing to more powerful computers showed that the growth of small-scale structures may be depleted at smaller scales, even though it was demonstrating initially the blowup tendency [84, 76, 82]. This may be explained by the self-organization of the flow into quasi-two-dimensional vorticity structures, a regularizing phenomenon [2] (recall that 2D flows are proved to retain smoothness).

Figure 1.3(a) displays the typical picture of DNS results: the growth of vorticity is usually moderate (not greater than 20 times the initial condition), there is no clear tendency of asymptotics, and the solutions are strongly sensitive to perturbations (even to numerical noise), a fact that resembles a chaotic nature [136]. Some numerical studies [92, 82] report that the growth of vorticity is not greater than double exponential, which would prevent the blowup to occur if such rate of growth persisted for longer times—see Fig. 1.3(b).

Besides Beale-Kato-Majda Theorem, other criteria have been used on numerical attempts to verify blowup. Examples are the track of singularities on the complex plane [70], also known as *analyticity-strip method* [23], and the limit of Voigt regularization [99]. Such investigations, however, suffer from the same limited resolution from computational simulations and, despite their new perspectives and insights, they do not settle the problem.

It is fair to say that, now, there is a lack of consensus even on the more probable answer (existence or not) to the blowup problem. It remains an active area of numerical research [92, 18, 99], but computational limitations are still the major obstacle. Indeed, a typical state-of-the-art DNS will not exceed a resolution of 8192^3 node points. This represents a spatial range of approximately 4×10^3 in Fourier space, which appears to be insufficient for the blowup analysis.

We remark that the blowup problem (**P.I**) is also formulated in the presence of solid boundaries [93]. Robust numerical evidences [104] and recent rigorous mathematical proofs [60, 35] are in favor of blowup in this set up. Nevertheless, this is a different problem.

Simplified Models

Numerical limitations of the DNS can be overcome using simplified models [151, 56, 108]. They were developed in lower spatial dimensions, like the Burgers equation [22] and the Constantin-Lax-Majda model [45, 124], or by exploring the cascade ideas in the so-called shell models [73, 123, 105]. Other approaches consider the restriction of the Euler or Navier-Stokes dynamics to a self-similar set of wave vectors, *e.g.*, the reduced wave vector set approximation (REWA) model introduced in [59, 79] and the geometrical formulation proposed in [80].

Despite being rather successful in the study of turbulence [78, 11, 16] and serving as a useful testing ground for mathematical analysis [90, 39], these models fall short of reproducing basic features of Euler's blowup phenomenon. Most of them are one-dimensional models and, thus, lack incompressibility. The Burgers equation is a

compressible model and it develops shock singularities, which do not occur in the incompressible Euler flow. Regarding regularity and singularities, shell models are closer to the Burgers equation than the Euler system [110]. The Constantin-Lax-Majda model presents a self-similar blowup, which is atypical in the Euler solutions [32, 34]. Among the available simplified models, the REWA model is the most structurally similar to the Euler equations, being a three-dimensional like model and presenting incompressibility constraint. Nevertheless, it shares with other models a geometric simplicity in its formulation, which prevents all of them from reproducing the observed vorticity structures from full DNS, *e.g.* two-dimensional depletion.

1.1.2 Vanishing viscosity limit and boundaries

The study of fully developed turbulence is related to infinite Reynolds limit, or, equivalently, vanishing viscosity limit. Mathematically, a natural question to ask is if the Navier-Stokes solutions converge to Euler's. As we discussed about dissipative anomaly and Onsager's conjecture, turbulent flows dissipate energy, and therefore possible convergences can only take place when velocity fields lack regularity. On the other hand, flows initially regular remain smooth for at least a short period of time. In two dimensions, for example, the flow is even globally regular. One may ask about whether the convergence takes place within their mutual regularity time interval.

In the absence of boundaries, this question is settled, and several proofs [116, 145, 88, 115] guarantee convergence. In the presence of boundaries, however, the scenario is completely different, because of the mismatch of boundary conditions: while the Navier-Stokes equations are supplemented with no-slip boundary condition $\mathbf{u} = \mathbf{0}$, Euler's are demanded to satisfy only no penetration boundary condition $\mathbf{u} \cdot \mathbf{n} = 0$. Therefore, the second main problem we address in this thesis is the following:

(P.II) Vanishing viscosity limit problem. *Do the Navier-Stokes solutions converge to Euler's when viscosity goes to zero in the presence of solid boundaries?*

This problem remains to a large extend unresolved and has been extensively investigated [95]. What could prevent the convergence is a boundary layer detachment [140], which is commonly linked to a finite time singularity in the Prandtl boundary layer equations [121].

The ideas stated above can be visualized in the vorticity snapshots in Fig. 1.4. The flow is confined between two solid boundaries from left and right. We impose periodic boundary conditions in the top and the bottom. We initialize the equations

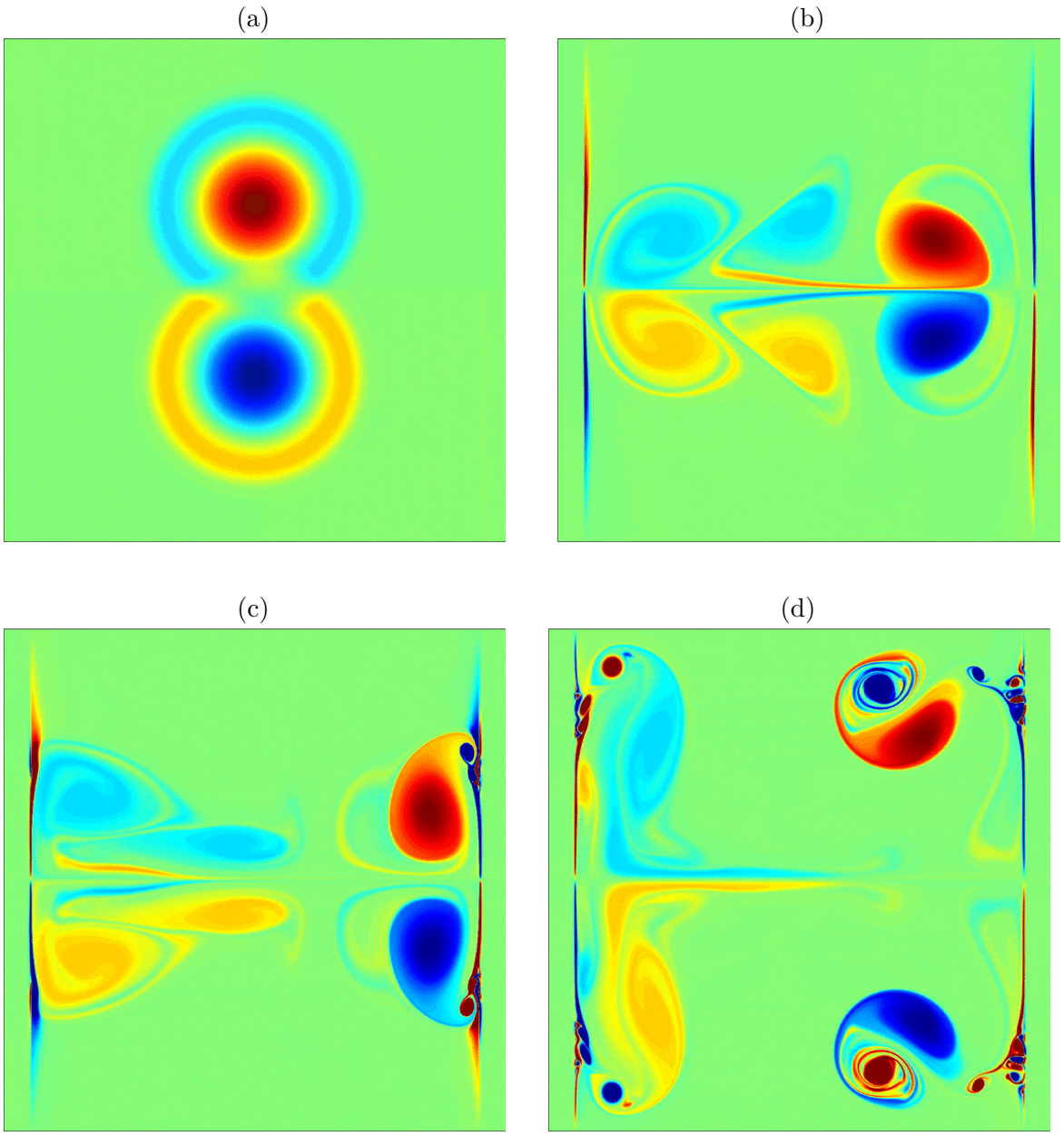

Fig. 1.4 Direct Numerical Simulations of a dipole vortex colliding with a solid wall. Snapshots are for vorticity field. The flow is confined by two solid boundaries on left and right. Periodic boundary conditions are imposed on top and bottom. The Navier-Stokes equations (1.1) are integrated using a pseudospectral method [149] and the solid boundary is modeled by a volume penalization method [122]. We time-step with a classical 4th order Runge-Kutta scheme using an integration factor.

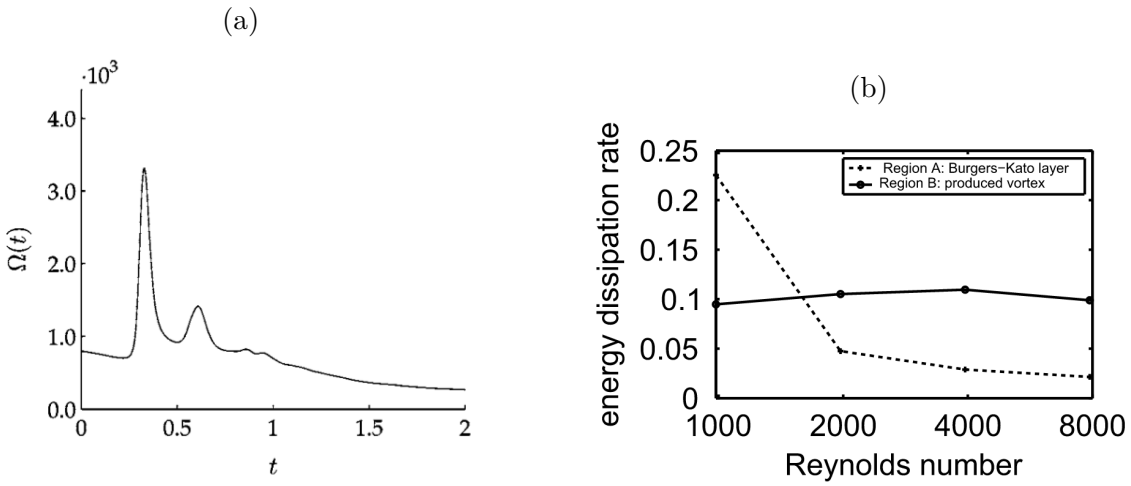

Fig. 1.5 Direct numerical simulations of dipole-wall collision. (a) Time evolution of total enstrophy $\Omega(t)$ of the flow. Figure reproduced from [94]. (b) Energy dissipation rate of the dipole-wall collision with respect to Reynolds numbers. The two lines represent specific highly dissipative regions of the flow. Figure reproduced from [122].

with a dipole of opposite vorticities in the center of the domain—Fig. 1.4(a). After the initialization, the cores of the dipole drift towards right. A sharp vorticity strip is developed very close to the bondaries—Fig. 1.4(b). This is Prandtl boundary layer, which becomes closer and closer to the boundary as viscosity decreases [140]. When the dipole collides with the wall, small but intense vorticity structures arise from the boundary—Fig. 1.4(c). They have the opposite sign of the vortex. This sharp adverse vorticity field arising from the walls is usually known as the boundary layer detachment. As a consequence, the large scale flow of the dipole rebound away from the wall—Fig. 1.4(d)—, while small scale structures continue to be generated at the boundaries.

All this phenomenology of boundary layers is strongly tight to the no-slip boundary condition and a very small viscosity. The inviscid case, however, is completely different. Euler's flow cannot penetrate boundaries, but it can slip along them, and this is what happens to inviscid solutions—consult [121, pp. 712-713] for snapshots of this same dipole-wall collision but evolved by Euler equations. These two contrasting states after collision—rebounded vortices for Navier-Stokes and its slippery Euler counterpart—strongly indicate a possible lack of convergence.

Besides qualitative observation and phenomenological statements, one may ask about quantities that may be used as a criterion for the convergence of Navier-Stokes to Euler's solutions. An answer is given by

Theorem 1.2 (Kato Equivalence Theorem [89])**.** *Let* $\mathbf{u}^0$ *be the unique local smooth solution of the Euler equations* (1.2) *and let* $\mathbf{u}^\nu$ *be a sequence of weak solutions of the Navier-Stokes equations* (1.1)*. Suppose they are all defined on a same interval of time* $[0, T]$*. Then,* $\mathbf{u}^\nu \to \mathbf{u}^0$ *in* L^2 *uniformly in* $[0, T]$ *as* $\nu \to 0$ *if and only if the total dissipation vanishes, i.e.* $\nu \int |\nabla \mathbf{u}|^2 d\mathbf{x} \to 0$*.*

In his original paper [89], Kato states more than that, but this formulation is sufficient for our purposes.

Roughly speaking, convergence may not take place if total dissipation is not vanishing. Recent DNS [122, 121] investigating problem (**P**.**II**) track the total (and local) dissipation of the flow for increasing Reynolds numbers. In Fig. 1.5 we see results from DNS of the dipole-wall collision. Fig. 1.5(a) shows the time evolution of the total enstrophy $\Omega(t)$ of the flow, which sharply increases and achieves a maximum when the vortex dipole collides against the wall [94]. This maximum is expected to grow as the Reynolds number raises, since the boundary layer becomes stronger. Such abrupt growth in dissipation is usually linked with a possible finite time singularity in the inviscid limit. In Fig. 1.5(b), we see that the dissipation within certain regions of the flow do not appear to vanish, but instead to reach a constant plateau value [122]. A subsequent work [121], performing different numerical methods, confirmed this behavior for even larger Reynolds numbers, reaching $Re \approx 10^5$. Still, direct numerical simulations are affected by the problems we already mentioned on the discussion about blowup: they have limited resolution, spatial ranges are confined to three or four decades in Fourier space, further increase of Reynolds number is very difficult. All those limitations are debilitating in the study of a phenomenon which is strongly based on high Reynolds numbers and spontaneous development of small scale structures.

1.2 Multi-scale dynamics and logarithmic lattices

The theory of multi-scale nonlinear flows and, in particular, the phenomenon of hydrodynamic turbulence comprise a multitude of yet unresolved problems: the global regularity of Navier-Stokes equations [66], explanation of intermittency [69], dissipation anomaly [64] and, of course, the blowup in ideal flow (**P.I**) and the vanishing viscosity limit (**P.II**) problems explained before. Many of these problems determine the state-of-the-art in nonlinear science and open new areas in mathematics and physics. Direct

numerical simulations often face computational difficulties due to limited resolution. In these studies, toy-models employed as caricatures of complex phenomena have been proved to be indispensable as the testing ground for new ideas and theories. Such models retain some basic features believed to be important, while the remaining content is simplified as much as possible. The conventional simplifications are related to reducing the spatial dimension, *e.g.* the one-dimensional Burgers equation [22] or the Constantin-Lax-Majda model [45] with further generalizations [124, 41]. The number of degrees of freedom can be drastically decreased by exploring the cascade ideas in the so-called shell models of turbulence [11]. In these models, multi-scale properties are mimicked by geometrical progressions of scales, resulting in the popular GOY [73, 123] and Sabra models [105], the reduced wave vector set approximation (REWA) [59, 79] and tree models [7, 9], as well as more sophisticated geometric constructions [80, 81]. Toy-models rely on the intuitive decision of what unimportant properties of the original system can be neglected. Of course, dealing with open problems, such decision has the risk of missing essential features of motion. Especially, this concerns neglected symmetries and conserved quantities, since fluid systems are known to possess highly nontrivial (infinite dimensional) symmetry groups and conservation laws [157, 113], *e.g.* the Kelvin Circulation Theorem.

In the present work, we propose a different approach for constructing simplified models, in which instead of simplified equations one introduces a simplified configuration space with proper algebraic operations and calculus. Basic ideas were introduced in our works [29, 26], where we employ velocity fields defined on discrete multi-dimensional lattices with logarithmically distributed nodes in Fourier space. These lattices are designed such that the equations of motion can be used in their exact original form and, as a consequence, the symmetry groups and conservation laws automatically carry over to the new system. The resulting models possess much higher degree of similarity to the exact equations as compared to conventional toy-models and, at the same time, share the property of being easily accessible for numerical analysis. Their strong reduction in degrees of freedom allows the simplified models to be easily simulated on a computer within a extremely large spatial range. This method was successfully applied to important problems in fluid dynamics, such as the blowup and shock solutions in the Burgers equation [26], the chaotic blowup in ideal flow [29], and the Navier-Stokes turbulence [30]. More generally, this technique is ready-to-use on any differential equation with quadratic nonlinearity.

With the framework of logarithmic lattices, we have a robust and promising tool for the investigation of several problems surrounding multi-scale nonlinear flows,

singularities and the spontaneous development of small-scale structures. In this thesis, we use the logarithmic lattice formalism to study problems (**P.I**) and (**P.II**), among others.

1.3 Structure of this thesis

This thesis is divided into three parts.

In **Part I**, we give a complete and rigorous mathematical structure to logarithmic lattices (§ 2) and to the functions defined on them (§ 3). Some generalizations are also proposed (§ 4). This is the framework upon which we construct the simplified models in the subsequent parts.

In **Part II**, we study flows without boundaries on logarithmic lattices. We start by ideal incompressible flow (§ 5), with great emphasis on the blowup problem (**P.I**) in the incompressible 3D Euler equations (§ 5.3). Next, we present some results for viscous incompressible flow (§ 6), such as anomalous dissipation (§ 6.1) and statistics of Fourier modes (§ 6.2).

In **Part III**, we show how to add solid boundaries to logarithmic lattice models. We first present our strategy through the immersed boundary method (§ 7), to later apply it on logarithmic lattices (§ 8). Our first application is on simple one-dimensional shear flows (§ 9). Through classical examples, we develop intuition on how to interpret the effect of boundaries on Fourier variables. Our last application lies on two-dimensional boundary layers (§ 10). The idea is to show how logarithmic lattice models with boundaries can be exploited to attack the vanishing viscosity limit problem (**P.II**).

We end the thesis with conclusions (§ 11).

Additional information and extensions of ideas are distributed among several appendices, compiled in the end of each part.

Part I

Logarithmic lattices and their structure

Chapter 2

Logarithmic lattices

In this chapter, we perform a systematic study of logarithmic lattices with certain geometric properties, providing the domain on which the dynamical models shall be defined in the rest of the thesis. We start with one-dimensional lattices, similar to those used in shell models, and then consider the multi-dimensional case.

Given a real number $\lambda > 1$, the *logarithmic lattice* with spacing factor λ is the set

$$\mathbb{\Lambda} = \{\pm\lambda^n\}_{n\in\mathbb{Z}}, \tag{2.1}$$

consisting of positive and negative integer powers of λ—see Fig. 2.1. This set has two properties important for applications. First, $\mathbb{\Lambda}$ is scale-invariant, *i.e.*, $\mathbb{\Lambda} = k\mathbb{\Lambda}$ for any $k \in \mathbb{\Lambda}$. Secondly, the points of the lattice grow geometrically with n. Thus, with only a few nodes we span a large range of scales. However, logarithmic lattices are not closed under addition as $p + q \notin \mathbb{\Lambda}$ for general $p, q \in \mathbb{\Lambda}$. Three points $k, p, q \in \mathbb{\Lambda}$ on a logarithmic lattice form a *triad* if $k = p + q$. In this case, we say that k *interacts* with p and q. The lattice is called *nondegenerate* if every two nodes interact through a finite sequence of triads. We are interested in a twofold task:

(i) to determine which spacings λ provide nondegenerate lattices, and

(ii) to classify all triads of nondegenerate lattices.

Because of the scale invariance, it is sufficient to describe the triads at unity, *i.e.*, $1 = p + q$.

Lattices $\mathbb{\Lambda}$ with nontrivial triad interactions exist only for certain values of λ. Let us first present three specific nondegenerate lattices. The lattice with $\lambda = 2$ has three possible types of triads described in Tab. 2.1(a) and Fig. 2.1(a). For any $k \in \mathbb{\Lambda}$, these triads are $k = \lambda k - k$, $k = -k + \lambda k$ and $k = \lambda^{-1}k + \lambda^{-1}k$. The next example is

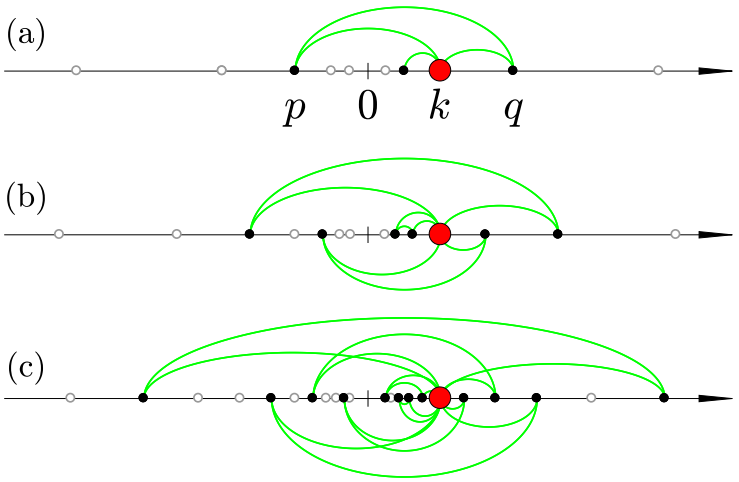

Fig. 2.1 Triad interactions on logarithmic lattices (2.1) with different spacing factors: (a) $\lambda = 2$; (b) $\lambda = (1+\sqrt{5})/2$, the golden mean; (c) $\lambda = \sigma$, the plastic number (2.2). The red node $k \in \mathbb{\Lambda}$ can be decomposed into sums $k = p + q$, where all possible $p, q \in \mathbb{\Lambda}$ are shown by the green lines. All figures are given in the same scale.

$\lambda = \varphi$, where $\varphi = (1+\sqrt{5})/2 \approx 1.618$ is the *golden mean*. All triads are obtained from permutations and rescalings of the identity $1 = \varphi^2 - \varphi$, providing the richer sample of interactions in Tab. 2.1(b). In this case, each point interacts with six different neighbors—see Fig. 2.1(b). Another example is provided by the *plastic number* of Dom Van der Laan [53]

$$\sigma = \frac{\sqrt[3]{9+\sqrt{69}} + \sqrt[3]{9-\sqrt{69}}}{\sqrt[3]{18}} \approx 1.325, \tag{2.2}$$

which is the common real solution of equations $\sigma^3 - \sigma - 1 = 0$ and $\sigma^5 - \sigma^4 - 1 = 0$. The lattice with spacing $\lambda = \sigma$ has twelve types of interacting triads, enumerated in Tab. 2.1(c) and depicted in Fig. 2.1(c). Because immediate neighbors are coupled, these are examples of nondegenerate lattices. On the other hand, if $\lambda = \sqrt{2}$, the lattice is degenerate: there are no interactions that couple points $\pm 2^n$ with $\pm 2^n\sqrt{2}$.

The main result of this chapter is the classification of nondegenerate logarithmic lattices with respect to their triad interactions, given by the following

Theorem 2.1. *The following three cases describe all nondegenerate lattices with spacing factors* $\lambda \geq 1.05$*:*

(i) $\lambda = 2$*, and all triads at the unity are given in Tab. 2.1(a);*

(ii) $\lambda = \sigma$*, the plastic number* (2.2)*, and all triads at the unity are given in Tab. 2.1(c);*

(a)

i	1	2	3
p_i	2	-1	1/2
q_i	-1	2	1/2

(b)

i	1	2	3	4	5	6
p_i	λ^b	$-\lambda^a$	λ^{b-a}	$-\lambda^{-a}$	λ^{-b}	λ^{a-b}
q_i	$-\lambda^a$	λ^b	$-\lambda^{-a}$	λ^{b-a}	λ^{a-b}	λ^{-b}

(c)

i	1	2	3	4	5	6	7	8	9	10	11	12
p_i	σ^3	$-\sigma$	σ^2	$-\sigma^{-1}$	σ^{-3}	σ^{-2}	σ^5	$-\sigma^4$	σ	$-\sigma^{-4}$	σ^{-5}	σ^{-1}
q_i	$-\sigma$	σ^3	$-\sigma^{-1}$	σ^2	σ^{-2}	σ^{-3}	$-\sigma^4$	σ^5	$-\sigma^{-4}$	σ	σ^{-1}	σ^{-5}

Table 2.1 Triads at the unity $1 = p_i + q_i$ for different spacing factors: (a) $\lambda = 2$; (b) λ satisfies $1 = \lambda^b - \lambda^a$ for integers $0 \le a < b$. For example, $\lambda = \varphi$ is the golden mean for $a = 1$ and $b = 2$; (c) $\lambda = \sigma$, the plastic number.

(iii) λ *satisfies* $1 = \lambda^b - \lambda^a$*, where* (a, b) *are mutually prime integers not larger than* 62*, excluding also the pairs* $(a, b) = (1, 3)$ *and* $(4, 5)$*. All triads at the unity are given in Tab. 2.1(b).*

Remark 2.2. We used the lower bound $\lambda \ge 1.05$ in order to make the numerically assisted proof possible. Still, we conjecture that Theorem 2.1 is valid for arbitrary $\lambda > 1$, with no upper bound for a and b in the item *(iii)*. A partial result in this direction is the theorem proved in [1], which states that the plastic number is the only common root greater than unity of any two distinct polynomials $\lambda^a - \lambda^{a-1} - 1$ and $\lambda^b - \lambda - 1$ with $a, b \ge 2$.

Proof. Let us consider the trinomial equation

$$p_{a,b}(\lambda) = \lambda^b - \lambda^a - 1 = 0, \tag{2.3}$$

with integer powers $0 \le a < b$. This equation has a single root in the interval $\lambda > 1$ because the function $p_{a,b}(\lambda)$ is strictly increasing in $\lambda \in [1, \infty)$ with image $[-1, \infty)$. Relation (2.3) yields the three equalities

$$1 = \lambda^b - \lambda^a = \lambda^{b-a} - \lambda^{-a} = \lambda^{-b} + \lambda^{a-b}. \tag{2.4}$$

There are six triads $1 = p + q$ corresponding to expressions (2.4) as described in Tab. 2.1(b). Let us show that the lattice is degenerate when a and b have a common divisor $m > 1$. For the sublattice $\mathbb{\Lambda}' = \{\pm\lambda^{mn}\}_{n\in\mathbb{Z}}$ to be coupled with the remaining

points, the spacing λ should satisfy another trinomial equation (2.3) with exponents (a', b') not multiples of m. However, this is not possible, as it follows from case (b) of Lemma 2.3 below. This leaves only the mutually prime pairs (a, b) to our consideration. Now, the theorem is a direct consequence of Lemma 2.3, where all triads are generated by the relations in (2.4): the case *(i)* corresponds to $(a, b) = (0, 1)$; the case *(ii)* to $(a, b) = (1, 3)$ and $(4, 5)$; and the case *(iii)* to all other possibilities. □

Lemma 2.3. *Consider two distinct trinomials* (2.3) *with integer powers* (a_1, b_1) *and* (a_2, b_2)*, where* $0 \leq a_1 < a_2$*. These trinomials have a common root* $\lambda \geq 1.05$ *if and only if*

(a) $\lambda = \sigma$ *is the plastic number* (2.2)*. In this case,* $(a_1, b_1) = (1, 3)$ *and* $(a_2, b_2) = (4, 5)$ *are mutually prime;*

(b) $\lambda = \sigma^{1/m}$ *with* $m = 2, \ldots, 5$*. In this case* $(a_1, b_1) = (m, 3m)$ *and* $(a_2, b_2) = (4m, 5m)$ *have the same common divisor* m*.*

Proof. Let us denote by $\lambda(a, b)$ the unique root of (2.3) in the interval $\lambda > 1$. Note that $\lambda(a, b) < \lambda(a', b)$ if $0 \leq a' < a$ because the polynomials $p_{a,b}(\lambda)$ are strictly increasing starting at $p_{a,b}(1) = p_{a',b}(1) = -1$ and $p_{a,b}(\lambda) < p_{a',b}(\lambda)$ for $\lambda > 1$. Therefore, if we fix the exponent b of trinomial $p_{a,b}(\lambda)$, then $\lambda(a, b)$ is maximized when $a = b - 1$. Next, $\lambda(b - 1, b)$ form a decreasing sequence with respect to b, since $p_{b-1,b}(\lambda) < p_{b,b+1}(\lambda)$. Finally, one may check that $p_{62,63}(1.05) > 0$, so $\lambda(62, 63) < 1.05$. Therefore $\lambda(a, b) \geq 1.05$ only if $b < 63$. This bound leaves a finite number of trinomials to our consideration. Since the plastic number σ satisfies $\sigma^5 - \sigma^4 - 1 = \sigma^3 - \sigma - 1 = 0$, we obtain the two cases *(a)* and *(b)* of the lemma. It remains to check that trinomials with different powers have no common root. This was accomplished via Validated Numerics [118], a computer assisted proof using the following strategy. Given two trinomials $p_{a,b}$ and $p_{a',b'}$, we estimate their respective roots λ_1 and λ_2 with Newton's Method up to machine double precision. Next, using Symbolic Algebra [44], we evaluate exactly the product $p_{a,b}p_{a',b'}$ at the middle point $\lambda_m = (\lambda_1 + \lambda_2)/2$ of their approximate roots. For all cases, it was verified a negative number at this point, which guarantees that $\lambda(a, b) \neq \lambda(a', b')$. □

The above results for one-dimensional logarithmic lattices can be extended to higher dimensions. The *d-dimensional logarithmic lattice* with spacing $\lambda > 1$ is given by the cartesian power $\mathbb{\Lambda}^d = \mathbb{\Lambda} \times \cdots \times \mathbb{\Lambda}$ (with d factors), *i.e.*, $\mathbf{k} = (k_1, \ldots, k_d) \in \mathbb{\Lambda}^d$ if each component $k_j \in \mathbb{\Lambda}$. Three points $\mathbf{k}, \mathbf{p}, \mathbf{q} \in \mathbb{\Lambda}^d$ on the lattice form a triad if $\mathbf{k} = \mathbf{p} + \mathbf{q}$.

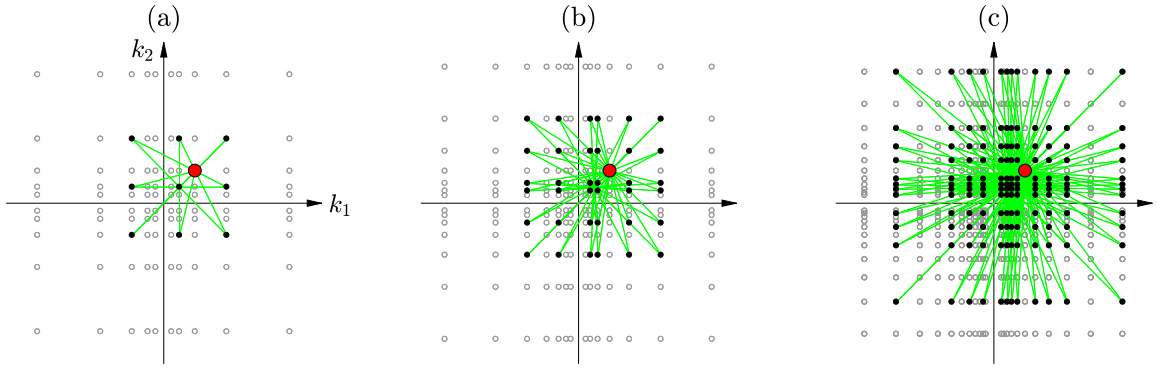

Fig. 2.2 Triad interactions on two-dimensional logarithmic lattices for different spacing factors: (a) $\lambda = 2$; (b) $\lambda = \varphi$, the golden mean; (c) $\lambda = \sigma$, the plastic number. The red node $\mathbf{k}$ can be decomposed into sums $\mathbf{k} = \mathbf{p} + \mathbf{q}$ where all possible nodes $\mathbf{p}$ and $\mathbf{q}$ are indicated by the green lines. All figures are given in the same scale. From (a) to (c), both the density of nodes and the number of triads per each node increase.

All nondegenerate lattices $\mathbb{\Lambda}^d$ are given by the spacings λ listed in Theorem 2.1 and all triads are combinations of the one-dimensional triads for each component—see Fig. 2.2 for the two-dimensional picture.

Chapter 3

Calculus on logarithmic lattices

Let us consider complex-valued functions $f(\mathbf{k}) \in \mathbb{C}$ on a nondegenerate logarithmic lattice $\mathbb{\Lambda}^d$, where $\mathbf{k} \in \mathbb{\Lambda}^d$ is interpreted as a wave vector in Fourier space. Motivated by the property of the Fourier transform of a real-valued function, we impose the reality condition

$$f(-\mathbf{k}) = \overline{f(\mathbf{k})}, \tag{3.1}$$

where the bar denotes complex conjugation. Thus, $f(\mathbf{k})$ is analogous to the Fourier transform of a real function, and now we are going to introduce basic operations.

Functions $f(\mathbf{k})$ possess a natural structure of a linear space with real scalars. Since we are working with Fourier-space representation, the spatial derivative ∂_j in the j-th direction is defined by the Fourier factor,

$$\partial_j f(\mathbf{k}) = ik_j f(\mathbf{k}), \quad j = 1, \dots, d, \tag{3.2}$$

where i is the imaginary unit. Clearly, higher order derivatives are products of such Fourier factors. Given two functions f and g, one defines their *inner product* naturally as

$$(f, g) = \sum_{\mathbf{k} \in \mathbb{\Lambda}^d} f(\mathbf{k}) \overline{g(\mathbf{k})}. \tag{3.3}$$

Just like the L^2-inner product of real functions, expression (3.3) is real valued because of reality condition (3.1). It also induces the associated ℓ^2 norm

$$\|f\| = (f, f)^{1/2} = \left(\sum_{\mathbf{k} \in \mathbb{\Lambda}^d} |f(\mathbf{k})|^2 \right)^{1/2}. \tag{3.4}$$

The notion of differentiability on the lattice retains some important calculus identities, like the integration by parts

$$(\partial_j f, g) = -(f, \partial_j g), \quad j = 1, \dots, d, \tag{3.5}$$

which follows from the fact that the inner product (3.3) couples $f(\mathbf{k})$ and $\overline{g(\mathbf{k})} = g(-\mathbf{k})$. We next define the product of two functions on the logarithmic lattice, which in Fourier space is understood as a convolution. Here and below, all functions are assumed to be absolutely summable

$$\sum_{\mathbf{k}\in\mathbb{\Lambda}^d} |f(\mathbf{k})| < \infty. \tag{3.6}$$

Definition 3.1. A *product on the logarithmic lattice* $\mathbb{\Lambda}^d$, denoted by $*$, is a binary operation between absolutely summable functions on $\mathbb{\Lambda}^d$, which satisfies the following properties:

(P.1) (Reality condition) $(f * g)(-\mathbf{k}) = \overline{(f * g)(\mathbf{k})}$;

(P.2) (Bilinearity) $(f + \gamma g) * h = f * h + \gamma(g * h)$, for any $\gamma \in \mathbb{R}$;

(P.3) (Commutativity) $f * g = g * f$;

(P.4) (Associativity in average) $(f * g, h) = (f, g * h)$;

(P.5) (Leibniz rule) $\partial_j(f * g) = \partial_j f * g + f * \partial_j g$, for $j = 1, \dots, d$;

Additional properties, which are related to the spatial symmetries of the lattice, may be imposed:

(S.1) (Scaling invariance) $\mathcal{S}_\lambda(f * g) = \mathcal{S}_\lambda f * \mathcal{S}_\lambda g$, where we denoted $\mathcal{S}_\lambda f(\mathbf{k}) = f(\lambda\mathbf{k})$, the rescaling of f by the lattice spacing λ;

(S.2) (Isotropy and parity) $(f * g) \circ R = (f \circ R) * (g \circ R)$, where we denoted $(f \circ R)(\mathbf{k}) = f(R\mathbf{k})$ and $R \in \mathsf{O}_\mathsf{h}$ is any element of the group of cube symmetries; *cf.* [97, §93]—it includes all transformations $(k_1, \dots, k_d) \mapsto (\pm k_{\alpha_1}, \dots, \pm k_{\alpha_d})$, where $(\alpha_1, \dots, \alpha_d)$ are permutations of $(1, \dots, d)$.

Remark 3.2. Lebniz rule readily implies *translation invariance* on the lattice, expressed as $\tau_{\boldsymbol{\xi}}(f * g) = \tau_{\boldsymbol{\xi}} f * \tau_{\boldsymbol{\xi}} g$, where $\tau_{\boldsymbol{\xi}} f(\boldsymbol{k}) = e^{-i\boldsymbol{k}\cdot\boldsymbol{\xi}} f(\boldsymbol{k})$ mimics the physical-space translation (in Fourier representation) by any vector $\boldsymbol{\xi} \in \mathbb{R}^d$;

The required properties for the product are chosen in order to mimic as much as possible a common pointwise product (or, equivalently, a convolution in Fourier space) of real functions defined in the Euclidean space. The symmetries of scaling invariance *(S.1)* and isotropy *(S.2)* can only be satisfied in a discrete form, because only discrete scalings and rotations are symmetries of the lattice itself. More importantly, we will prove shortly that the product cannot be associative. Nevertheless, the weaker property of associativity in average *(P.4)* is satisfied, which turns out to be sufficient for our purposes.

We first establish the general form of the product on one-dimensional lattices. Later, it will be generalized to higher dimensions. Bilinearity *(P.2)*, Leibniz rule *(P.5)* and scaling invariance *(S.1)* yield the following general form of the product

$$(f * g)(k) = \sum_{p_j+q_j=1} c_j f(p_j k) g(q_j k), \quad k \in \mathbb{\Lambda}. \tag{3.7}$$

Here, the Leibniz rule restricts the product to triad interactions, which are determined by the factors p_j and q_j from Tab. 2.1 for each lattice of Theorem 2.1. The independence of the coefficients c_j on k is a consequence of the scaling invariance. Next, reality condition *(P.1)* and parity $k \mapsto -k$, from *(S.2)*, imply that the coefficients c_j are real. Since the sum in (3.7) has a finite number of terms, the product of two absolutely summable functions is absolutely summable.

As an example, consider the case $\lambda = 2$. Then, for the three triads in Tab. 2.1(a), formula (3.7) becomes

$$(f * g)(k) = c_1 f(2k) g(-k) + c_2 f(-k) g(2k) + c_3 f(2^{-1}k) g(2^{-1}k). \tag{3.8}$$

We are interested in non-trivial products (3.7), where the coefficients c_j do not vanish simultaneously.

Theorem 3.3. *Let $\mathbb{\Lambda}$ be one of the logarithmic lattices (i)–(iii) described in Theorem 2.1. For the lattices (i) and (iii), the product with properties (P.1)–(P.5) and symmetries (S.1) and (S.2) is unique, up to a real prefactor which we set to unity, and has the form*

$$(f * g)(k) = \sum_{p_j+q_j=1} f(p_j k) g(q_j k), \quad k \in \mathbb{\Lambda}, \tag{3.9}$$

where the coupling factors p_j and q_j are given in Tab. 2.1. For the lattice (ii), the general form of the product is

$$(f * g)(k) = c_1 \sum_{\substack{p_j+q_j=1 \\ j=1,\dots,6}} f(p_j k) g(q_j k) + c_2 \sum_{\substack{p_j+q_j=1 \\ j=7,\dots,12}} f(p_j k) g(q_j k), \quad k \in \mathbb{\Lambda}, \tag{3.10}$$

where c_1 and c_2 are arbitrary real prefactors.

Proof. Properties *(P.1)*, *(P.2)*, *(P.5)* and symmetries *(S.1)* and *(S.2)* were already used to reduce the product to the form (3.7). One may check that the remaining conditions *(P.3)* and *(P.4)* for the product can be written as linear equations with unit coefficients with respect to the variables c_j. The system of such equations can be solved explicitly, leading to formulas (3.9) and (3.10). Consider, for example, the case $\lambda = 2$, whose product expression is given by (3.8). Commutativity *(P.3)* requires $c_1 = c_2$. On the other hand, associativity in average *(P.4)* enforces all coefficients to be the same. □

Recall that the associativity condition is valid in average; see property *(P.4)* in Definition 3.1. At the same time, the products cannot be associative, as it follows from

Corollary 3.4. *The non-trivial products described in Theorem 3.3 are not associative: condition $(f * g) * h = f * (g * h)$ is not valid for all functions f, g and h.*

Proof. Let us show that there are $p, q, r \in \mathbb{\Lambda}$ such that $p + q, p + q + r \in \mathbb{\Lambda}$, but $q + r \notin \mathbb{\Lambda}$. From the proof of Theorem 2.1, there are integers $0 \leq a < b$ such that the spacing λ satisfies $1 = \lambda^b - \lambda^a$. Take $p = \lambda^{2b}$, $q = -\lambda^{a+b}$ and $r = -\lambda^a$. Then $p + q + r = 1 \in \mathbb{\Lambda}$ and $p + q = \lambda^b \in \mathbb{\Lambda}$. We claim that $q + r = -(1 + \lambda^b)\lambda^a \notin \mathbb{\Lambda}$, which is equivalent to the condition $1 + \lambda^b \notin \mathbb{\Lambda}$. Indeed, suppose that $1 + \lambda^b \in \mathbb{\Lambda}$. In this case, $1 + \lambda^b = \lambda^m$ for some integer $m > b$. It follows that λ is a common root of trinomials (2.3) with $(a_1, b_1) = (a, b)$ and $(a_2, b_2) = (b, m)$. However, such a solution is forbidden by Lemma 2.3, leading to a contradiction. Now, indicating by δ_k the function with $\delta_k(k) = 1$ and zero elsewhere, it follows from expression (3.9) that $(\delta_p * \delta_q) * \delta_r = \delta_{p+q} * \delta_r = \delta_{p+q+r}$, but $\delta_p * (\delta_q * \delta_r) = \delta_p * 0 = 0$. A similar argument applies to expression (3.10). □

Remark 3.5. How to reconstruct physical space from lattice variables is beyond the scope of this work. Nevertheless, the lack of associativity by Corollary 3.4 implies that such a reconstruction cannot satisfy the convolution theorem (pointwise products in physical space are mapped to convolutions in Fourier space). We recall that this is a well-known fact about Fourier-decimated dynamics [71, 24, 25].

Application of the same ideas for the two and three-dimensional cases yield similar formulas for products on these spaces, but with a larger number of free coefficients. For instance, the product on the three-dimensional lattice with spacing $\lambda = \varphi$, the golden mean, has ten free real coefficients.

It is useful to give the following expression

$$(f * g)(\mathbf{k}) = \sum_{\substack{\mathbf{p}+\mathbf{q}=\mathbf{k} \\ \mathbf{p},\mathbf{q}\in\mathbb{\Lambda}^d}} f(\mathbf{p})g(\mathbf{q}), \quad \mathbf{k} \in \mathbb{\Lambda}^d, \tag{3.11}$$

analogous to (3.9), which yields a product in any dimension and any lattice.

All operations introduced in this section are implemented in LogLatt, an efficient Matlab® library for the numerical calculus on logarithmic lattices [27, 28]. We give a detailed presentation of LogLatt in Appendix B.

Chapter 4

Generalized lattices and products

In this chapter we discuss some generalizations of logarithmic lattices and the operations upon them, which can be useful for applications.

Products with lattice volumes

Products may be generalized by taking lattice volumes into account. Considering arbitrary parameters $\alpha, \beta \in \mathbb{R}$, we define the inner-product

$$(f, g) = \sum_{\mathbf{k} \in \mathbb{\Lambda}^d} |k_1 \dots k_d|^\alpha f(\mathbf{k}) \overline{g(\mathbf{k})} \tag{4.1}$$

and the star product

$$(f * g)(\mathbf{k}) = |k_1 \dots k_d|^\beta \sum_{\substack{\mathbf{p}+\mathbf{q}=\mathbf{k} \\ \mathbf{p},\mathbf{q} \in \mathbb{\Lambda}^d}} \left| \frac{p_1 \dots p_d}{k_1 \dots k_d} \frac{q_1 \dots q_d}{k_1 \dots k_d} \right|^{\frac{\alpha+\beta}{3}} f(\mathbf{p}) g(\mathbf{q}). \tag{4.2}$$

The factors $|k_1 \dots k_d|$ are interpreted as the volume of lattice cells. Parameters α and β can be manipulated to change dimensionality and the scaling of terms. Product (4.2) satisfies all properties *(P.1)-(P.5)* and also *(S.2)*. Scaling invariance *(S.1)* is still valid, but with the prefactor

$$\mathcal{S}_\lambda (f * g) = \lambda^{\beta d} \mathcal{S}_\lambda f * \mathcal{S}_\lambda g. \tag{4.3}$$

Lattices with zero components

In order to mimic non-local interactions, one can add the origin to the logarithmic lattice

$$\mathbb{\Lambda} = \{0\} \cup \{\pm \lambda^n\}_{n \in \mathbb{Z}}. \tag{4.4}$$

In this case, every point $k \in \mathbb{\Lambda}$ interacts with the zero node: $k = k + 0 = 0 + k$, which provides additional (non-local) terms to the products. The value $f(0)$ is interpreted as the mean value of f in physical space, in analogy with the same value for continuous functions $\hat{F}(0) = \int F(x)dx$.

The same relations (3.1)–(3.6) and Definition 3.1 are used to define the product and other operations. For example, when $\lambda = 2$, the product (3.9) at $k \neq 0$ generalizes to

$$(f * g)(k) = [f(2k)g(-k) + f(-k)g(2k) + f(2^{-1}k)g(2^{-1}k)] + c[f(k)g(0) + f(0)g(k)], \tag{4.5}$$

with an arbitrary real parameter c. The product $f * g$ evaluated at $k = 0$ is given by

$$(f * g)(0) = c \sum_{k \in \mathbb{\Lambda}} f(k)g(-k) \tag{4.6}$$

with the same prefactor c, which is the consequence of associativity in average—see *(P.4)* of Definition 3.1. It is natural to set $c = 1$, in which case expression (4.6) coincides with the inner product (3.3), *i.e.*, $(f * g)(0) = (f, g)$.

Generalized logarithmic lattices

Furthermore, we can define *generalized logarithmic lattices* as arbitrary subsets $\mathbb{\Lambda}' \subset \mathbb{\Lambda}^d$ of logarithmically distributed nodes. To ensure that functions satisfying the reality condition (3.1) can be represented in $\mathbb{\Lambda}'$, we impose the property that if $\mathbf{k} \in \mathbb{\Lambda}'$ then $-\mathbf{k} \in \mathbb{\Lambda}'$. This is the case, for example, of a truncated lattice with a finite number of points

$$\mathbb{\Lambda}' = \{0, \pm 1, \pm\lambda, \ldots, \pm\lambda^N\}, \tag{4.7}$$

or the same subset excluding zero. Since a generalized lattice $\mathbb{\Lambda}'$ is not necessarily scaling invariant or isotropic, we cannot demand the corresponding product to have these symmetries. Therefore, a product on $\mathbb{\Lambda}'$ is an operation satisfying properties *(P.1)*–*(P.5)* of Definition 3.1. In the following theorem, we provide one natural form of the product that serves for all generalized lattices.

Theorem 4.1. *Let $\mathbb{\Lambda}' \subset \mathbb{\Lambda}^d$ be a generalized d-dimensional logarithmic lattice. Then, operation*

$$(f * g)(\mathbf{k}) = \sum_{\substack{\mathbf{p}+\mathbf{q}=\mathbf{k} \\ \mathbf{p},\mathbf{q} \in \mathbb{\Lambda}'}} f(\mathbf{p})g(\mathbf{q}), \quad \mathbf{k} \in \mathbb{\Lambda}', \tag{4.8}$$

defines a product on $\mathbb{\Lambda}'$ with properties (P.1)–(P.5).

Proof. Properties *(P.1)–(P.5)* are directly verified, except for the associativity in average *(P.4)*, which follows from the fact that both $(f * g, h)$ and $(f, g * h)$ can be written in the same form as

$$\sum_{\substack{\mathbf{p}+\mathbf{q}+\mathbf{r}=\mathbf{0} \\ \mathbf{p},\mathbf{q},\mathbf{r}\in\mathbb{\Lambda}'}} f(\mathbf{p})g(\mathbf{q})h(\mathbf{r}). \tag{4.9}$$

□

Note that when $\lambda = 2$ and we let $N \to \infty$, the lattice (4.7) establishes a decimation of Fourier space for 2π-periodic functions, in the spirit of *e.g.* [71, 24, 25]. Other examples, also for $\lambda = 2$ are [59, 79]. The application of lattice operations to the one-dimensional Burgers equation reproduces some well-known shell models of turbulence—see Appendix A for the details.

Appendix A

Burgers' representation for shell models

In this appendix, we show that some well-known shell models of turbulence are equivalent to the Burgers equation on a logarithmic lattice. This, in particular, reinforces the idea that self-similar blowup and non-oscillatory Kolmogorov regime in shell models follow a scenario closer to Burgers' dynamics [108, 110] than to Euler's.

The Burgers equation [22] on the one-dimensional logarithmic lattice of spacing λ is given by

$$\partial_t u + u * \partial_x u = \nu \partial_x^2 u, \tag{A.1}$$

where $\nu \geq 0$ is the viscosity. First, let us take $\lambda = 2$ and consider the corresponding product (3.9) with a prefactor of 2. The Burgers equation (A.1) takes the form

$$\partial_t u(k) = -ik \left[2u(2k)\overline{u(k)} + u^2\left(\frac{k}{2}\right)\right] - \nu k^2 u(k). \tag{A.2}$$

Define the geometric progression $k_n = \lambda^n,\ n \in \mathbb{Z}$ and consider purely imaginary solutions of type $u(\pm k_n) = \pm i u_n$ for $u_n \in \mathbb{R}$. Note that this is a property of the Fourier transform for any odd function in physical space. Then, equation (A.2) taken at $k = k_n$ reduces to the form

$$\partial_t u_n = k_n u_{n-1}^2 - k_{n+1} u_{n+1} u_n - \nu k_n^2 u_n. \tag{A.3}$$

This system is known as the Desnyansky-Novikov shell model [54], also called dyadic model.

For our second example, we take $\lambda = \varphi$, the golden mean, and consider the product (3.9) with prefactor $-\varphi$. By setting $u(k_n) = u_n$ and $u(-k_n) = \overline{u_n}$ with $k_n = \varphi^n$, the Burgers equation (A.1) is reduced to the form

$$\partial_t u_n = i[k_{n+1} u_{n+2} \overline{u_{n+1}} - (1+c) k_n u_{n+1} \overline{u_{n-1}} - c k_{n-1} u_{n-1} u_{n-2}] - \nu k_n^2 u_n, \tag{A.4}$$

with $c = -\varphi^2$. System (A.4) is the Sabra shell model [105].

A third possibility is to consider $\lambda = \sigma$, the plastic number (2.2), which reduces Eq. (A.1) to a new shell model with improved number of triad interactions. In this spirit, extended triads were considered in the context of helical shell models [50].

Model (A.1) on the logarithmic lattice retains several properties of the continuous Burgers equation, like the symmetries of time translation $t \mapsto t + t_0$ by any $t_0 \in \mathbb{R}$, physical-space translation $u(k) \mapsto e^{-ik\xi} u(k)$ by a number $\xi \in \mathbb{R}$ and, in the case of a lattice with origin, Galilean invariance $u(k,t) \mapsto e^{-ikvt} u(k,t) - \widehat{v}(k)$ for any $v \in \mathbb{R}$, where $\widehat{v}(0) = v$ and zero for $k \neq 0$. Inviscid ($\nu = 0$) regular solutions also conserve the momentum $M(t) = u(k=0)$, energy $E(t) = \frac{1}{2}(u,u)$ and the thrid-order moment $M_3(t) = (u * u, u) = (u, u * u)$, which is well-defined because of associativity in average of the product—see property *(P.4)* in Definition 3.1. All these conservation laws can be proved using only the operations on logarithmic lattices—see [26]. Conservation of energy is a well-known property of shell models while the conservation of a third-order moment was revealed in the study of Hamiltonian structure in Sabra model [106]. Unlike the continuous Burgers equation, higher-order moments are not conserved for the logarithmic models because of non-associativity on the logarithmic lattice—see Corollary 3.4—which turns higher powers not even well-defined. The non-existence of invariants of order greater than three was proved in [55] for the Sabra model. Sabra model has one more inviscid quadratic invariant of the form $I = \sum_{n \in \mathbb{Z}} c^{-n} |u_n|^2$, but this invariant do not seem to have an analogue in the Burgers equation. In studies of hydrodynamic turbulence, it was interpreted as the enstrophy for $c > 0$ (sign definite invariant) and as helicity for $c < 0$ (not sign-definite invariant).

Our methodology not only reproduces shell models but also leads to new insights about them. Inspired by Theorem 5.3 in the coming Chapter 5, consider a scalar field ρ evolving as

$$\partial_t \rho + \partial_x (\rho * u) = 0. \tag{A.5}$$

This equation mimics a passive scalar advected by the flow, *e.g.* density. Then, the cross-correlation

$$\Gamma(t) = (\rho, u) \tag{A.6}$$

which can be seen as total momentum of the flow, is conserved in time. The proof follows similar lines as those already presented and may be found in [26]. Since this conservation holds for all solutions $\rho(t)$, this provides infinitely many inviscid invariants for model (A.1), analogous to circulation in Kelvin's Theorem to be described in Section 5.1. Up to our knowledge, this has not been shown earlier.

Appendix B

LogLatt: A computational library for the calculus and flows on logarithmic lattices

In this appendix, we introduce LogLatt, an efficient Matlab® library for the numerical calculus and operations between functions on logarithmic lattices [27]. The library was specially designed for the operations introduced in the Part I of this thesis. It is freely available for noncommercial use in Matlab Central File Exchange [28]. The computational applicabilities are available for one-, two- and three-dimensional lattices, and include usual differential operators from vector calculus, norms and the functional products. The operations are encoded as Matlab function handles. This provides simple and intuitive scripts. When applied to partial differential equations, the models are coded exactly as they are mathematically written. This library will make the computational calculus on logarithmic lattices accessible in an efficient framework for the study of nonlinear equations. All numerical experiments in the subsequent chapters make use of LogLatt.

This appendix is composed by two sections. In Section B.1, we describe the implementation of the library and its computational cost. In Section B.2, we apply it to the one-dimensional Burgers equation, in order to validate the library and attest its efficiency.

B.1 Computational library

Since only a finite number of points can be represented on computer's memory, all routines are developed upon the truncated lattice

$$\mathbb{\Lambda} = \{\pm 1, \pm\lambda, \pm\lambda^2, \ldots, \pm\lambda^{N-1}\} \tag{B.1}$$

with N points in each direction. Then, lattice $\mathbb{\Lambda}^d$ mimics the d-dimensional Fourier space of a system with largest integral scale $L \sim 2\pi$ corresponding to $|\mathbf{k}| \sim 1$ and finest scale ℓ defined by N as $\ell \sim 2\pi/\lambda^{N-1}$. Finer resolutions may be accessed by increasing N.

As we have classified in Theorem 2.1, LogLatt considers three representative lattice spacings λ:

(L.1) (dyadic) $\lambda = 2$;

(L.2) (golden mean) $\lambda = \varphi$, where $\varphi = (1+\sqrt{5})/2 \approx 1.618$ is the golden mean;

(L.3) (plastic number) $\lambda = \sigma$, where $\sigma = (\sqrt[3]{9+\sqrt{69}} + \sqrt[3]{9-\sqrt{69}})/\sqrt[3]{18} \approx 1.325$ is the plastic number.

These and other lattices with triads may be obtained also from

(L.4) (integers $0 \le a < b$) λ satisfies $1 = \lambda^b - \lambda^a$, where $0 \le a < b$ are some integers.

LogLatt is composed by distinct routines for each of the spatial dimensions. We first present the simpler one-dimensional case in Section B.1.1 to next extend it to two and three dimensions in Section B.1.2. Here the focus is to describe the applicabilities of the library and how to implement each operation. Lastly, we discuss in Section B.1.3 the computational efficiency of the products, the most expensive operation of the library.

B.1.1 One-dimensional lattices

In one-dimensional space, the logarithmic lattice is simply the set (B.1). Because of reality condition (3.1), we don't need to carry negative lattice points on the memory. Therefore, functions $f(k) \in \mathbb{C}$ on the lattice $k \in \mathbb{\Lambda}$ are represented by complex valued arrays `f` of size $N \times 1$.

All applicabilities in the one-dimensional case are encoded in the m-file `LogLatt1D.m`. This routine should be called by specifying the lattice, say the number of points N and the lattice spacing λ. This can be done in three different forms of input:

(I.1) `(N)` If only the number N of nodes is input, the lattice spacing is the golden mean *(L.2)*, by default;

(I.2) `(N,str)` The usual lattice spacings *(L.1)*, *(L.2)* and *(L.3)* may be input as strings `str = 'dyadic'`, `'golden'` and `'plastic'`, respectively;

(I.3) `(N,a,b)` Lattice *(L.4)* may be introduced through the integers $0 \leq a < b$.

Henceforward, we adopt input *(I.2)* whenever the function needs the lattice to be specified. The operations and the lattice itself are obtained through the command `[product,l2norm, l2inner,sup,dx,lapl,K] = LogLatt1D(N,str)`. We describe now each of the outputs.

The array `K` has size $N \times 1$ and contains the lattice points $(1, \lambda, \lambda^2, \ldots, \lambda^{N-1})$. The remaining outputs are function handles for the operations on lattice functions: given two functions f and g, encoded as $N \times 1$ arrays `f` and `g`, `l2inner(f,g)` returns their inner product (3.3); `l2norm(f)` and `sup(f)` give the ℓ^2 norm (3.4) and the maximum absolute value $\max_{k \in \mathbb{\Lambda}} |f(k)|$ of f; `dx(f)` computes the function $\partial_x f$, which is the spatial derivative of f given by the Fourier factor (3.2); `lapl(f)` is the laplacian of f, which in one-dimensional space is simply the second-order spatial derivative $\partial_x^2 f$; finally, `product(f,g)` gives the product function $f * g$, *i.e.*, the convolution on the lattice (4.8). A practical example of implementation will be given in Section B.2, where the operations from `LogLatt1D.m` are applied in the study of the one-dimensional Burgers equation.

B.1.2 Two- and three-dimensional lattices

We describe in details the two-dimensional case only, which, except for minor changes enumerated at the end of this section, has the same form of implementation and applicabilities for three-dimensional lattices.

Two dimensions

Functions on two-dimensional logarithmic lattices are computationally represented by matrices. Because of reality condition (3.1), it is sufficient to keep only the first two quadrants of Fourier space. In this case, scalar functions f are encoded as complex matrices `f` of size $N \times N \times 2$, where `f(m,n,q)` returns the value $f(\mathbf{k}_{m,n,q})$ with

$$\mathbf{k}_{m,n,q} = \begin{cases} (\ \ \lambda^{m-1}, \ \ \lambda^{n-1}) & \text{if } q = 1 \quad \textit{(1st quadrant)}, \\ (-\lambda^{m-1}, \ \ \lambda^{n-1}) & \text{if } q = 2 \quad \textit{(2nd quadrant)}. \end{cases} \tag{B.2}$$

Vector fields receive an additional input at the end, which designates the component, and thus become of size $N \times N \times 2 \times 2$.

The applicabilities for two-dimensional lattices are split into four routines: `LogLatt2D.m`, for the geometry of the lattice; `LogLatt2D_diff.m`, for the two-dimensional differential operators; `LogLatt2D_norms.m`, for the norms; and `LogLatt2D_product.m`, for the functional product. Except for the norms routine, which receives no inputs, all of them are called by specifying the lattice in one of the three ways *(I.1)–(I.3)* above. We describe their outputs in details now.

The lattice itself is obtained by the command `[Kx,Ky,Knorm] = LogLatt2D(N,str)`: `Kx` and `Ky` are the x and y coordinates of each point from the lattice; `Knorm` is their Euclidean norm. They are $N \times N \times 2$ matrices and their entries follow the same enumeration (B.2) as described above for scalar functions.

For the two-dimensional lattice, several differential operators from vector calculus are available as function handles through the command `[dx,dy,lapl,lapl_,grad,div,rot, rot_] = LogLatt2D_diff(N,str)`: given a scalar function f encoded as the matrix `f`, `dx(f)` and `dy(f)` are the partial derivatives $\partial_x f$ and $\partial_y f$; `lapl(f)` and `lapl_(f)` are the laplacian operator $\Delta f(\mathbf{k}) = -|\mathbf{k}|^2 f(\mathbf{k})$ and its inverse $\Delta^{-1} f(\mathbf{k}) = -|\mathbf{k}|^{-2} f(\mathbf{k})$, which is well-defined on the lattice (B.1); `grad(f)` computes the gradient $\operatorname{grad} f = (\partial_x f, \partial_y f)$; given a vector field $\mathbf{u} = (u_x, u_y)$ represented by the matrix `u`, `div(u)` calculates its divergence $\operatorname{div} \mathbf{u} = \partial_x u_x + \partial_y u_y$ and `rot(u)` its scalar rotational $\operatorname{rot} \mathbf{u} = \partial_x u_y - \partial_y u_x$, *i.e.*, the nontrivial z-component of the full rotational vector; `rot_` is the inverse of rotational in the space of solenoidal vector fields; more precisely, it receives a scalar function f and computes an incompressible vector field $\mathbf{u}$ satisfying $\operatorname{rot} \mathbf{u} = f$, explicitly given by $\mathbf{u} = -\Delta^{-1}(\partial_y f, -\partial_x f)$.

The norms are initialized by `[l2norm,l2inner,sup] = LogLatt2D_norms`, with no inputs. They are implemented as it was described in the one-dimensional case, and they operate equally on scalar functions and vector fields.

Finally, product (4.8) is obtained from `product = LogLatt2D_product(N,str)` and operates on scalar functions only.

In Chapter 10 we apply the two-dimensional library (with some modifications) to the study of boundary layers.

Three dimensions

Here we limit ourselves to highlight the differences between the three- and two-dimensional routines. Because of reality condition (3.1), we only represent the four

octants with $z > 0$ in the three-dimensional space. Extending the two-dimensional enumeration (B.2), scalar functions f are encoded as complex matrices `f` of size $N \times N \times N \times 4$, where `f(m,n,p,q)` returns the value $f(\mathbf{k}_{m,n,p,q})$ with

$$\mathbf{k}_{m,n,p,q} = \begin{cases} (\ \lambda^{m-1}, & \lambda^{n-1}, & \lambda^{p-1}) & \text{if } q = 1 \quad \textit{(1st octant)}, \\ (-\lambda^{m-1}, & \lambda^{n-1}, & \lambda^{p-1}) & \text{if } q = 2 \quad \textit{(2nd octant)}, \\ (-\lambda^{m-1}, & -\lambda^{n-1}, & \lambda^{p-1}) & \text{if } q = 3 \quad \textit{(3rd octant)}, \\ (\ \lambda^{m-1}, & -\lambda^{n-1}, & \lambda^{p-1}) & \text{if } q = 4 \quad \textit{(4th octant)}. \end{cases} \tag{B.3}$$

Vector fields receive an additional entry in the end indicating the component, and thus become of size $N \times N \times N \times 4 \times 3$. Routines for geometry and differential operators output the additional z-component of the lattice `Kz` and the partial derivative in the z-direction `dz`. The rotational `rot` gives the full vector field rot $\mathbf{u} = (\partial_y u_z - \partial_z u_y, \partial_z u_x - \partial_x u_z, \partial_x u_y - \partial_y u_x)$ and its inverse in the space of solenoidal fields `rot_` receives a vector field $\mathbf{u}$ and computes the incompressible vector field $\mathbf{v}$ satisfying rot $\mathbf{v} = \mathbf{u}$, explicitly given by $\mathbf{v} = -\Delta^{-1}\text{rot}\ \mathbf{u}$.

In Chapters 5 and 6 we apply the three-dimensional library to the incompressible Euler and Navier-Stokes equations, respectively.

B.1.3 Computational cost

Computationally, the most expensive operation on the logarithmic lattice is the unconventional convolution (4.8), which couples local triads in Fourier space. When applied to nonlinear differential equations, the many executions of such products may take a substantial parcel of the computational cost. Aiming to reduce the execution time, LogLatt adopts the following coding strategy. When initialized, the product routine locates and stores all interacting triads into an array mask, which is efficiently used each time the product is invoked. This strategy reduces the time spent on the computation of each convolution, at the cost of, first and only once, classifying and storing in memory all triads in the lattice. In two and three dimensions, this is done by an external C routine, called by Matlab through a mex-file, which, for larger amounts of storage, proved to be more efficient than solely the Matlab computation. The one-dimesional case, instead, benefits from Matlab's multithreading.

Fig. B.1 summarizes the computational cost of library LogLatt and how this cost grows with the number of points N, in one-, two- and three-dimensional lattices; here, the spacing λ is the golden mean *(L.2)*. Efficiency is estimated up to $N = 60$, which in

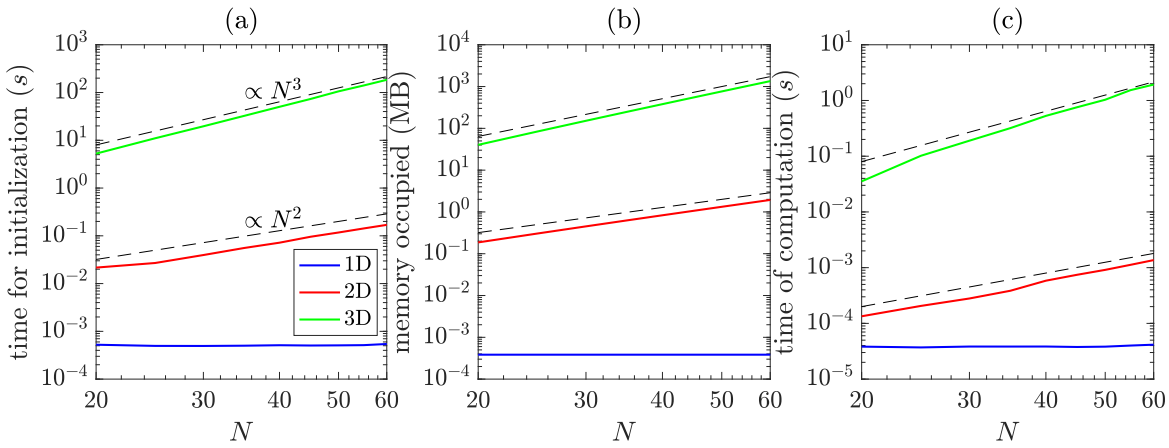

Fig. B.1 Computational cost of CPU time, in seconds, and memory usage, in MegaBytes, of the product routines with respect to the number of node points N, for one-, two- and three-dimensional lattices with golden mean spacing *(L.2)*: (a) time for initialization of product routines; (b) memory occupied by the product function handle; (c) time of computation for one product (4.8). Dashed lines indicating growths $\propto N^d$ for $d = 2, 3$ are plotted for comparison. All figures are in log-scale.

Fourier space covers a spatial range $k_{\max} = \varphi^{60} \approx 10^{12}$. The CPU time of execution is measured in seconds and all runs were performed in MATLAB R2016b on a MAC® with Intel® Core i5 CPU 1.8 GHz 8 GB RAM.

Figs. B.1(a,b) show the computational cost, in CPU time and memory occupied, for the initialization of the products. The three-dimensional lattice with best resolution ($N = 60$) takes around a couple of minutes to initialize and occupies 1 GB in memory. In turn, one- and two-dimensional products are initialized within less than a second and take no more than 2 MB in memory. We recall that the products need to be initialized only once before computations and have the alternative of being saved as mat-files and quickly loaded whenever needed. The expense of this initialization is rewarded in the reduced CPU time for a single convolution, as shown in Fig. B.1(c), where, even in the higher three-dimensional resolution, the operation takes not even two seconds to be fully executed. Differently from a full convolution, the local convolution (4.8) in the d-dimensional lattice has complexity $O(N^d)$. This is readily confirmed by the measured time of computation in Fig. B.1(c), except for the one-dimensional case, which is coded using a different strategy as said above and benefits from MATLAB's multithreading.

B.2 Application to the Burgers equation

The forced Burgers equation on the one-dimensional logarithmic lattice (B.1) is given by

$$\partial_t u + u * \partial_x u = \nu \partial_x^2 u + f, \tag{B.4}$$

where $u(k,t)$ represents the velocity modes on the lattice $k \in \mathbb{\Lambda}$ at time $t \in \mathbb{R}$, $\nu \geq 0$ is the viscosity and $f(k,t)$ is an external force. All functions are supposed to satisfy the reality condition (3.1). For the properties of the Burgers equation (B.4), see the Appendix A, or consult [26] for further details.

When considering purely imaginary solutions, the Burgers equation (B.4) on the dyadic lattice *(L.1)* can be reduced to the Desnyansky-Novikov shell model of turbulence [54], also called the dyadic shell model—see Appendix A or consult [30] for the detailed deduction. Introducing a constant-in-time force

$$f = i\delta_1, \tag{B.5}$$

where $\delta_1(1) = 1$ and $\delta_1(k) = 0$ for $k \neq 1$, this model is well-known for blowing up when $\nu = 0$ and to recover assymptotically the fixed-point solution $u(k) = ik^{-1/3}$ in the inviscid regularization $\nu \to 0$, a behavior which was related to the development of shock solutions in the original Burgers equation [110].

The m-file `Burgers1D.m` in Listing B.1 solves the Burgers equation (B.4), with the constant forcing (B.5) and zero initial condition, on the one-dimensional dyadic logarithmic lattice *(L.1)*. We fix $N = 20$ points in the lattice, which covers a spatial range $k_{\max} = 2^{20} \approx 10^6$. The functionalities of the library are initialized through `LogLatt1D.m` in the preamble, which is called as in *(I.2)*. The viscosity `nu` and the force `f` are defined in the usual way. Using the `product` and `dx` function handles, the time variation in the Burgers equation is written, as a function of the time `t` and the velocity

```
% Burgers1D.m   Solver for Burgers' equation on the one-dimensional logarithmic
    lattice
N = 20; % number of lattice nodes
[product,l2norm,l2inner,sup,dx,lapl,K] = LogLatt1D(N,'dyadic'); % preamble

nu = 1e-2; % viscosity
f = zeros(N,1); f(1) = 1j; % constant in time force
dudt = @(t,u) -product(u,dx(u)) + nu*lapl(u) + f; % Burgers' equation
uinit = zeros(N,1); % initial condition
T = 5; % time of integration
[t,u] = ode15s(dudt,[0 T],uinit); % solver
```

Listing B.1 m-file Burgers1D.m

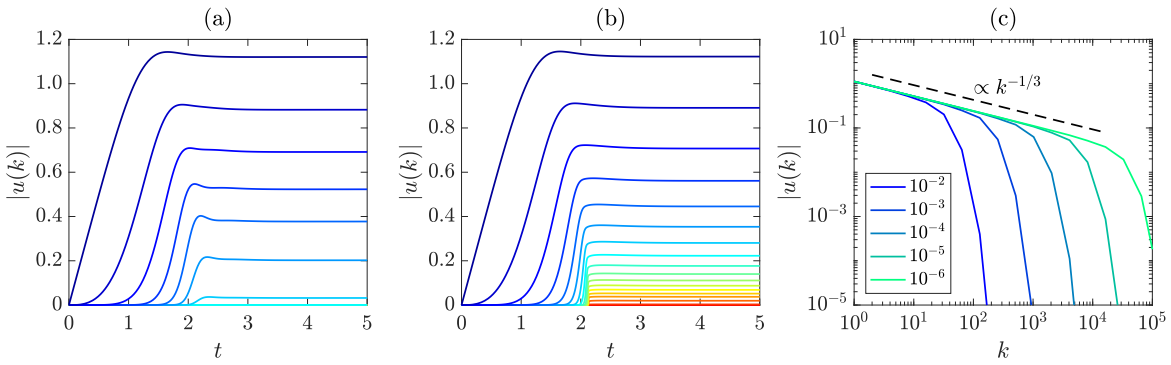

Fig. B.2 Solutions of the Burgers equation on the one-dimensional dyadic logarithmic lattice *(L.1)*, with the constant forcing (B.5) and zero intial condition: (a) and (b) show the time evolution of lattice variables $|u(k)|$, at several points k, for viscosities $\nu = 10^{-2}$ and 10^{-6}, respectively; colors change from blue to red by increasing $|k|$; (c) solution spectrum $|u(k)|$, in log-scales, at the final instant $t = 5$ for different viscosities $\nu = 10^{-2},\ 10^{-3},\ 10^{-4},\ 10^{-5},\ 10^{-6}$.

`u`, in the very intuitive way `dudt = @(t,u) −product(u,dx(u))+nu∗lapl(u)+f`. For simplicity, we use the MATLAB native ODE solver `ode15s`, a variable-step, variable-order solver for stiff equations based on the numerical differentiation formulas of orders one to five—consult [141] for details. `Burgers1D.m` returns the solution `u` at time instants `t` after around 0.06 second of CPU time.

Figs. B.2(a,b) show the time evolution of velocities $|u(k)|$ at several lattice points k for viscosities $\nu = 10^{-2}$ and 10^{-6}, respectively. These graphs are generated by the command `plot(t,abs(u))`. We observe an abrupt growth of the velocities around the inviscid blowup time $t_b \approx 2.13$, which gets more pronounced for smaller viscosities. The viscous solution can be extended beyond the blowup time and develops an assymptotic power-law scaling $|u(k)| \sim k^{-1/3}$ as the dissipation range is shifted towards larger k in the inviscid limit $\nu \to 0$. This dynamics is better visualized by plotting, in log-scales, the solution spectrum at the final instant of time through the command `loglog(K,abs(u(end,:)))` and is readily verified in Fig. B.2(c).

Part II

Flows without boundaries on logarithmic lattices

Chapter 5

Ideal incompressible flow

In this and next chapters, we make sense of incompressible hydrodynamics on logarithmic lattices by applying the operations introduced previously. Strategies dealing with compressibility are considered in Appendix C.

We will consider a d-dimensional logarithmic lattice $\mathbb{\Lambda}^d$, for $d = 2$ or 3, where

$$\mathbb{\Lambda} = \{0, \pm 1, \pm\lambda, \pm\lambda^2, \dots\}, \tag{5.1}$$

for some λ from Theorem 2.1. This lattice mimics Fourier space of a system with largest integral scale $L \sim 2\pi$ corresponding to $|\mathbf{k}| \sim 1$. Our derivations below are equally valid for the case $\mathbb{\Lambda} = \{\pm 1, \pm\lambda, \pm\lambda^2, \dots\}$, where zero is excluded from (5.1).

This section is subdivided as follows. Section 5.1 introduces the incompressible Euler equations on the logarithmic lattice and enumerates their main properties. Section 5.2 establishes rigorous results concerning the local-in-time existence and uniqueness of strong solutions and the criterion for singularity formation in this model. Section 5.3 presents a numerical study of blowup in the three-dimensional equations.

5.1 Basic equations, symmetries and conservation laws

We represent the velocity field $\mathbf{u}(\mathbf{k}, t) = (u_1, \dots, u_d) \in \mathbb{C}^d$ as a function of the wave vector $\mathbf{k} \in \mathbb{\Lambda}^d$ and time $t \in \mathbb{R}$. Similarly we define the scalar pressure $p(\mathbf{k}, t)$. The inner product for vector fields will be understood as $(\mathbf{u}, \mathbf{v}) = (u_1, v_1) + \dots + (u_d, v_d)$ with the inner product (3.3) for each scalar component. All functions are supposed to satisfy the reality condition (3.1).

For the governing equations, we use the exact form of the incompressible Euler equations

$$\partial_t \mathbf{u} + \mathbf{u} * \nabla \mathbf{u} = -\nabla p, \quad \nabla \cdot \mathbf{u} = 0, \tag{5.2}$$

which are defined upon the logarithmic lattice $\mathbb{\Lambda}^d$, with the conventional notation $(\mathbf{u} * \nabla \mathbf{v})_i = \sum_{j=1}^d u_j * \partial_j v_i$ for the product $*$ from Theorem 4.1. Introducing the vorticity $\boldsymbol{\omega} = \nabla \times \mathbf{u}$ and taking the curl of equations (5.2), we may write the Euler equations in vorticity formulation

$$\partial_t \boldsymbol{\omega} + \mathbf{u} * \nabla \boldsymbol{\omega} = \boldsymbol{\omega} * \nabla \mathbf{u}. \tag{5.3}$$

In the case of vanishing average velocity $\mathbf{u}(\mathbf{0}) = \mathbf{0}$ at $\mathbf{k} = \mathbf{0}$, the velocity field is recovered from the vorticity through the Biot-Savart law

$$\mathbf{u}(\mathbf{k}) = \frac{i\mathbf{k} \times \boldsymbol{\omega}(\mathbf{k})}{|\mathbf{k}|^2} \quad \text{for } \mathbf{k} \neq \mathbf{0}; \quad \mathbf{u}(\mathbf{0}) = \mathbf{0}. \tag{5.4}$$

Moreover, if we take the divergence of equation (5.2) and use the incompressibility condition, then the pressure may be obtained from the velocities by solving the Poisson equation

$$-\Delta p = \nabla \cdot (\mathbf{u} * \nabla \mathbf{u}). \tag{5.5}$$

The proposed model retains many properties of the continuous Euler equations, which rely only upon the structure of the equations and elementary operations on the logarithmic lattice, as described in the previous sections. These include the basic symmetry groups.

Theorem 5.1 (Symmetry groups of the Euler equations on the logarithmic lattice)**.** *Let* $\mathbf{u}(\mathbf{k}, t)$*,* $p(\mathbf{k}, t)$ *be a solution of the Euler equations* (5.2)*. Then the following transformations also yield solutions:*

(E.1) (Time translations) $\mathbf{u}^\tau(\mathbf{k}, t) = \mathbf{u}(\mathbf{k}, t + \tau)$*, for any* $\tau \in \mathbb{R}$*;*

(E.2) (Space translations) $\mathbf{u}^{\boldsymbol{\xi}}(\mathbf{k}, t) = e^{-i\mathbf{k}\cdot\boldsymbol{\xi}}\mathbf{u}(\mathbf{k}, t)$*, for any* $\boldsymbol{\xi} \in \mathbb{R}^d$*;*

(E.3) (Isotropy and parity) $\mathbf{u}^R(\mathbf{k}, t) = R^{-1}\mathbf{u}(R\mathbf{k}, t)$*, where* $R \in \mathsf{O}_\mathsf{h}$ *is any element of the group of cube symmetries (cf. Definition 3.1);*

(E.4) (Scale invariance) $\mathbf{u}^{n,h}(\mathbf{k}, t) = \lambda^h \mathbf{u}\left(\lambda^n \mathbf{k}, \lambda^{h-n} t\right)$*, for any* $h \in \mathbb{R}$ *and* $n \in \mathbb{Z}$*, where* λ *is the lattice spacing;*

(E.5) (Time reversibility) $\mathbf{u}^r(\mathbf{k}, t) = -\mathbf{u}(\mathbf{k}, -t)$*;*

(E.6) (Galilean invariance) $\mathbf{u}^{\mathbf{v}}(\mathbf{k},t) = e^{-i\mathbf{k}\cdot\mathbf{v}t}\mathbf{u}(\mathbf{k},t) - \widehat{\mathbf{v}}(\mathbf{k})$, *for any* $\mathbf{v} \in \mathbb{R}^d$, *where* $\widehat{\mathbf{v}}(\mathbf{k})$ *is the constant velocity field on the lattice defined as* $\widehat{\mathbf{v}}(\mathbf{0}) = \mathbf{v}$ *and zero for* $\mathbf{k} \neq \mathbf{0}$.

We did not write the transformations for the pressure p because it can be eliminated from the Euler equations.

Recall that the factors $e^{-i\mathbf{k}\cdot\boldsymbol{\xi}}$ and $e^{-i\mathbf{k}\cdot\mathbf{v}t}$ in the symmetries *(E.2)* and *(E.6)* are Fourier representations of physical-space translations by the vectors $\boldsymbol{\xi}$ and $\mathbf{v}t$. Thus, the listed symmetries of the Euler equations on the logarithmic lattice are the same as those for the continuous model, except that isotropy *(E.3)* and scale invariance *(E.4)* are given in discrete form.

Model (5.2) also preserves the same invariants as the continuous Euler equations. Let us show this first for the energy and for the enstrophy or helicity, in the two or three-dimensional cases respectively. Here we proceed formally. The proofs in this section hold for strong solutions, whose existence and uniqueness for short times are established in the next Section 5.2.

Theorem 5.2 (Conservation of energy, enstrophy, helicity)**.** *Let* $\mathbf{u}(t)$ *be a solution of the three-dimensional Euler equations* (5.2)*. Then the energy*

$$E(t) = \frac{1}{2}(\mathbf{u}, \mathbf{u}) \tag{5.6}$$

and the helicity

$$H(t) = (\mathbf{u}, \boldsymbol{\omega}) \tag{5.7}$$

are conserved in time. In the the two-dimensional case, the energy (5.6) *and the enstrophy*

$$\Omega(t) = \frac{1}{2}(\boldsymbol{\omega}, \boldsymbol{\omega}) \tag{5.8}$$

are conserved in time.

Proof. Taking the energy as an example, let us show how the proof can be written using the basic operations defined on the logarithmic lattice, following the standard approach of fluid dynamics. Using the Euler equations (5.2), we obtain

$$\frac{dE}{dt} = \frac{d}{dt}\left[\frac{1}{2}(\mathbf{u}, \mathbf{u})\right] = (\mathbf{u}, \partial_t \mathbf{u}) = -(\mathbf{u}, \nabla p) - (\mathbf{u}, \mathbf{u} * \nabla \mathbf{u}). \tag{5.9}$$

The pressure term vanishes owing to the incompressibility condition as

$$(\mathbf{u}, \nabla p) = \sum_{i=1}^{d} (u_i, \partial_i p) = -\sum_{i=1}^{d} (\partial_i u_i, p) = -(\nabla \cdot \mathbf{u}, p) = 0, \tag{5.10}$$

where the second relation is obtained from the integration by parts (E.7). In the inertial term, using commutativity of the product *(P.3)*, the associativity in average *(P.4)* and the Leibniz rule *(P.5)*, one obtains

$$(\mathbf{u}, \mathbf{u} * \nabla \mathbf{u}) = \sum_{i,j=1}^{d} (u_i, u_j * \partial_j u_i) = \sum_{i,j=1}^{d} (u_i * \partial_j u_i, u_j) = \frac{1}{2} \sum_{i,j=1}^{d} (\partial_j (u_i * u_i), u_j). \quad (5.11)$$

After integration by parts, this term vanishes due to the incompressibility condition.

Conservation of enstrophy and helicity in their respective space dimensions can be proved following a similar line of derivations. □

One can also derive the analogue of Kelvin's Circulation Theorem for the Euler system (5.2) on a logarithmic lattice. For this purpose, let us recall the relation of circulation with the cross-correlation $\Gamma = (\mathbf{u}, \mathbf{h})$ for "frozen-into-fluid" divergence-free vector fields $\mathbf{h}(\mathbf{k}, t)$ satisfying the equations [113]

$$\partial_t \mathbf{h} + \mathbf{u} \cdot \nabla \mathbf{h} - \mathbf{h} \cdot \nabla \mathbf{u} = \mathbf{0}, \quad \nabla \cdot \mathbf{h} = 0. \quad (5.12)$$

The circulation around a closed material contour $\mathbf{C}(s, t)$ in three-dimensional physical space (s is the arc length parameter) is given by the cross-correlation Γ with the field [157]

$$\mathbf{h}(\mathbf{x}, t) = \oint \frac{\partial \mathbf{C}(s, t)}{\partial s} \, \delta^3(\mathbf{x} - \mathbf{C}(s, t)) \, ds, \quad (5.13)$$

where δ^3 is the 3D Dirac delta function. The field (5.13) satisfies equations (5.12) in the sense of distributions. Thus, Kelvin's Theorem follows, as a particular case, from the conservation of cross-correlation Γ. The following theorem proves the conservation of cross-correlation in the lattice model.

Theorem 5.3 (Kelvin's Theorem on logarithmic lattices)**.** *Let* $\mathbf{u}(t)$ *be a solution of the three-dimensional Euler equations* (5.2) *on a logarithmic lattice. Then, for any "frozen-into-fluid" divergence-free field* $\mathbf{h}(t)$ *satisfying equations*

$$\partial_t \mathbf{h} + \mathbf{u} * \nabla \mathbf{h} - \mathbf{h} * \nabla \mathbf{u} = \mathbf{0}, \quad \nabla \cdot \mathbf{h} = 0, \quad (5.14)$$

the cross-correlation $\Gamma(t) = (\mathbf{u}, \mathbf{h})$ *is conserved in time.*

Since equations (5.14) are satisfied by the vorticity field $\boldsymbol{\omega}$, the proof for conservation of the cross-correlation follows the same steps as for conservation of helicity (5.7). Theorem 5.3 provides an infinite number of circulation invariants: the cross-correlation Γ is conserved for any solution of system (5.14).

For two-dimensional flows, Kelvin's Theorem can be reformulated as the conservation of flux of vorticity across surfaces moving with the fluid. This flux can be expressed as the inner product $\Gamma(t) = (a, \omega)$ of the scalar vorticity $\omega = \partial_1 u_2 - \partial_2 u_1$ with a Lagrangian marker $a(\mathbf{k}, t)$ [113], which is advected by the flow and satisfies the equation $\partial_t a + \mathbf{u} \cdot \nabla a = 0$. Indeed, taking the Lagrangian marker as the indicator function of a bounded surface S_t carried by the flow [42, Sec. 1.2], the flux of vorticity across S_t yields the circulation along the contour ∂S_t, *i.e.*, $\Gamma(t) = \int_{S_t} \omega dS = \int_{\partial S_t} \mathbf{u} \cdot d\mathbf{l}$. On the logarithmic lattice, the vorticity flux is introduced similarly, as the inner product $\Gamma(t) = (a, \omega)$ of the scalar vorticity with a Lagrangian marker satisfying the equation

$$\partial_t a + \mathbf{u} * \nabla a = 0. \tag{5.15}$$

It is straightforward to show that, given the solution $\mathbf{u}(\mathbf{k}, t)$ of the two-dimensional Euler system (5.2), the conservation of Γ holds for any solution of (5.15).

5.2 Regularity of solutions

In this section, we establish the local theory for the Euler system on the logarithmic lattice. Here the results are similar to those for the original model: we show local existence and uniqueness of strong solutions and the Beale-Kato-Majda (BKM) blowup criterion [6]. Two-dimensional solutions turn out to be globally regular. The proofs are similar to those in [46, 37, 90, 39] for shell models and exploit locality of nonlinear interactions on the logarithmic lattice, which turns the convective term into the action of a bounded operator. In this framework, all classical bounds on the nonlinear term are preserved, and energy methods are naturally carried over.

For simplicity, we consider the case of the lattice without zero components, *i.e.*, $0 \notin \mathbb{\Lambda}$, in the following analysis. For the lattice variables, we introduce the ℓ^2 norm in the standard way as $\|\mathbf{u}\|_{\ell^2} = (\sum_{\mathbf{k}\in\mathbb{\Lambda}^d} |\mathbf{u}(\mathbf{k})|^2)^{1/2}$ and the ℓ^∞ norm as $\|\mathbf{u}\|_{\ell^\infty} = \sup_{\mathbf{k}\in\mathbb{\Lambda}^d} |\mathbf{u}(\mathbf{k})|$. Given a nonnegative integer m, we introduce the operator D^m as

$$D^m \mathbf{u}(\mathbf{k}) = |\mathbf{k}|^m \mathbf{u}(\mathbf{k}), \tag{5.16}$$

and define the homogeneous Sobolev spaces h^m on the lattice consisting of the functions with finite norm

$$\|\mathbf{u}\|_{h^m} = \|D^m \mathbf{u}\|_{\ell^2} = \left(\sum_{\mathbf{k}\in\mathbb{\Lambda}^d} |\mathbf{k}|^{2m} |\mathbf{u}(\mathbf{k})|^2 \right)^{1/2} < \infty. \tag{5.17}$$

Clearly, the space h^m is a Hilbert space endowed with the inner product $(\mathbf{u},\mathbf{v})_{h^m} = (D^m\mathbf{u}, D^m\mathbf{v})$, whose functions have all partial derivatives up to order m in ℓ^2. Finally, we consider the space of divergence-free vector fields

$$V^m = \{\mathbf{u} \in h^m | \nabla\cdot\mathbf{u} = 0\}, \tag{5.18}$$

which provides the natural setting for strong solutions of the Euler equations. The space V^m is endowed with the h^m norm.

Theorem 5.4. *Let $\mathbf{u}^0 \in V^m$ for some $m \geq 1$. Then, there exists a time $T > 0$, such that the incompressible Euler equations on the logarithmic lattice* (5.2) *have a unique strong solution $\mathbf{u}(t)$ in the class*

$$\mathbf{u} \in C^1([0,T); V^m), \tag{5.19}$$

with initial condition $\mathbf{u}\big|_{t=0} = \mathbf{u}^0$. This solution either exists globally in time, or there is a finite maximal time of existence t_b such that

$$\limsup_{t\nearrow t_b} \|\mathbf{u}(t)\|_{h^m} = \infty. \tag{5.20}$$

Proof. We write the Euler system (5.2) in the functional form

$$\partial_t\mathbf{u} + B(\mathbf{u},\mathbf{u}) = -\nabla p, \tag{5.21}$$

where we have introduced the operator

$$B(\mathbf{u},\mathbf{v}) = \mathbf{u} * \nabla\mathbf{v}. \tag{5.22}$$

Operator B is a bounded bilinear operator in h^m—see the proof in Appendix D.

Next, in order to eliminate pressure, we project Eq. (5.21) onto the space of divergence-free vector fields. We introduce the Leray projector $\mathbb{P}$—*cf.* [135, Sec. 2.1]—on the logarithmic lattice, explicitly given by

$$\mathbb{P}_{ij}(\mathbf{k}) = \delta_{ij} - \frac{k_i k_j}{|\mathbf{k}|^2}, \quad \mathbf{k} \in \mathbb{\Lambda}^d. \tag{5.23}$$

Since $\mathbf{u}$ is divergence free and ∇p is a full gradient, it follows that $\mathbb{P}\mathbf{u} = \mathbf{u}$ and $\mathbb{P}\nabla p = 0$, and so we are reduced to the problem

$$\frac{d\mathbf{u}}{dt} = F(\mathbf{u}), \quad \mathbf{u}\Big|_{t=0} = \mathbf{u}^0, \tag{5.24}$$

where $F(\mathbf{u}) = -\mathbb{P}B(\mathbf{u},\mathbf{u})$ maps functions from V^m to itself. We claim that F is locally-Lipschitz continuous. Since $\mathbb{P}$ is an orthogonal projection on h^m, and therefore $\|\mathbb{P}\mathbf{v}\|_{h^m} \leq \|\mathbf{v}\|_{h^m}$, we have

$$\begin{aligned} \|F(\mathbf{u}) - F(\mathbf{v})\|_{h^m} &= \|\mathbb{P}[B(\mathbf{u},\mathbf{u}) - B(\mathbf{v},\mathbf{v})]\|_{h^m} \\ &\leq \|B(\mathbf{u},\mathbf{u}) - B(\mathbf{v},\mathbf{v})\|_{h^m} \\ &\leq \|B(\mathbf{u},\mathbf{u}-\mathbf{v})\|_{h^m} + \|B(\mathbf{u}-\mathbf{v},\mathbf{v})\|_{h^m}. \end{aligned} \tag{5.25}$$

In the last inequality, we have applied the bilinearity of B and the triangle inequality. Using the boundness of operator B, there exists a constant $C > 0$ such that

$$\|B(\mathbf{u},\mathbf{u}-\mathbf{v})\|_{h^m} \leq C\|\mathbf{u}\|_{h^m}\|\mathbf{u}-\mathbf{v}\|_{h^m}. \tag{5.26}$$

A similar inequality is obtained for the other term $\|B(\mathbf{u}-\mathbf{v},\mathbf{v})\|_{h^m}$, which proves the Lipschitz continuity of F when $\|\mathbf{u}\|_{h^m}$ and $\|\mathbf{v}\|_{h^m}$ are bounded by some constant.

It follows that Eq. (5.24) is an ordinary differential equation with F locally-Lipschitz continuous on the Banach space V^m. In this framework, we apply the Picard Theorem on Banach spaces—see *e.g.* [31, 139]—to guarantee existence of a unique local solution in the class (5.19) and initial condition $\mathbf{u}^0$. The pressure is recovered by solving the Poisson equation (5.5). The blowup statement in (5.20) also follows from classical theory of ordinary differential equations [139]. □

Theorem 5.5 (BKM blowup criterion)**.** *Let $\mathbf{u}(t) \in C^1([0,t_b);V^m)$ be a strong solution for the incompressible Euler equations* (5.2) *on the logarithmic lattice, where t_b is the maximal time of existence. Then either $t_b = \infty$ or*

$$\int_0^{t_b} \|\boldsymbol{\omega}(t)\|_{\ell^\infty} dt = \infty. \tag{5.27}$$

In the later case, we have necessarily

$$\limsup_{t \nearrow t_b} \|\boldsymbol{\omega}(t)\|_{\ell^\infty} = \infty. \tag{5.28}$$

Proof. Let us assume that

$$\int_0^{t_b} \|\boldsymbol{\omega}(t)\|_{\ell^\infty} dt = M < \infty. \tag{5.29}$$

for a finite $t_b < \infty$. We are going to prove that this implies

$$\|\mathbf{u}(t)\|_{h^m} \leq N, \quad \forall t < t_b, \tag{5.30}$$

for some constant $N < \infty$, thus contradicting condition (5.20) of Theorem 5.4. To show this, we perform an energy estimate for Eq. (5.2). We set $\mathbf{v} = D^m\mathbf{u}$ and $q = D^m p$ and apply D^m to Eq. (5.2) to obtain

$$\partial_t \mathbf{v} = -D^m(\mathbf{u} * \nabla\mathbf{u}) - \nabla q. \tag{5.31}$$

Taking the ℓ^2-inner product of Eq. (5.31) with $\mathbf{v}$ yields

$$\frac{1}{2}\frac{d}{dt}\|\mathbf{v}\|_{\ell^2}^2 = -(D^m(\mathbf{u} * \nabla\mathbf{u}), \mathbf{v}) - (\nabla q, \mathbf{v}). \tag{5.32}$$

After integrating by parts, the last term vanishes due to incompressibility as

$$(\nabla q, \mathbf{v}) = \sum_{i=1}^{d}(\partial_i q, v_i) = -\sum_{i=1}^{d}(q, \partial_i v_i) = -\sum_{i=1}^{d}(q, D^m\partial_i u_i) = -(q, D^m\nabla\cdot\mathbf{u}) = 0. \tag{5.33}$$

Next, we use the following calculus inequality on logarithmic lattices

$$\|\mathbf{f} * \mathbf{g}\|_{h^m} \leq C(\|\mathbf{f}\|_{h^m}\|\mathbf{g}\|_{\ell^\infty} + \|D\mathbf{f}\|_{\ell^\infty}\|\mathbf{g}\|_{h^{m-1}}), \quad \text{for } \mathbf{f} \in h^m, \mathbf{g} \in h^{m-1} \tag{5.34}$$

for some positive constant C; this inequality has a continuous analogue for Sobolev spaces H^s—see *e.g.* [113, Sec. 3.2.1]—and the lattice version (5.34) is proved in the Appendix D. Then, the nonlinear term in (5.32) can be estimated using $\mathbf{f} = \mathbf{u}$ and $\mathbf{g} = \nabla u_i$ as

$$\begin{aligned}
(D^m(\mathbf{u} * \nabla\mathbf{u}), \mathbf{v}) &\leq \|\mathbf{u} * \nabla\mathbf{u}\|_{h^m}\|\mathbf{v}\|_{\ell^2} \\
&\leq C\|\mathbf{v}\|_{\ell^2}\sum_{i=1}^{d}(\|\mathbf{u}\|_{h^m}\|\nabla u_i\|_{\ell^\infty} + \|D\mathbf{u}\|_{\ell^\infty}\|\nabla u_i\|_{h^{m-1}}) \\
&\leq 2dC\|\mathbf{v}\|_{\ell^2}\|\mathbf{u}\|_{h^m}\|D\mathbf{u}\|_{\ell^\infty} = C'\|\mathbf{v}\|_{\ell^2}^2\|D\mathbf{u}\|_{\ell^\infty},
\end{aligned} \tag{5.35}$$

where at the end we used $\|\mathbf{u}\|_{h^m} = \|D^m\mathbf{u}\|_{\ell^2} = \|\mathbf{v}\|_{\ell^2}$ and set $C' = 2dC$. Substituting relations (5.33) and (5.35) into (5.32) yields

$$\frac{d}{dt}\|\mathbf{v}\|_{\ell^2}^2 \leq 2C'\|\mathbf{v}\|_{\ell^2}^2\|D\mathbf{u}\|_{\ell^\infty}, \tag{5.36}$$

and applying Gronwall's Inequality—consult *e.g.* [61, p. 708]—, we are lead to

$$\|\mathbf{v}(t)\|_{\ell^2} \leq \|\mathbf{v}(0)\|_{\ell^2} \exp\left(C' \int_0^t \|D\mathbf{u}(s)\|_{\ell^\infty} ds\right). \tag{5.37}$$

Finally, using the estimate

$$\|D\mathbf{u}\|_{\ell^\infty} \leq \|\boldsymbol{\omega}\|_{\ell^\infty}, \tag{5.38}$$

which follows from the Biot-Savart law (5.4), and recalling again that $\|\mathbf{v}\|_{\ell^2} = \|\mathbf{u}\|_{h^m}$, we obtain

$$\|\mathbf{u}(t)\|_{h^m} \leq \|\mathbf{u}(0)\|_{h^m} \exp\left(C' \int_0^{t_b} \|\boldsymbol{\omega}(s)\|_{\ell^\infty} ds\right) \leq N, \quad \forall t \in [0, t_b) \tag{5.39}$$

for $N = \|\mathbf{u}(0)\|_{h^m} \exp(C'M) < \infty$. This is the inequality (5.30), which led us to contradiction. □

Corollary 5.6. *Strong solutions* $\mathbf{u}(t)$ *of the two-dimensional incompressible Euler equations* (5.2) *exist globally in time.*

Proof. From Theorem 5.2, strong solutions of the two-dimensional Euler equations conserve the ℓ^2 norm $\|\boldsymbol{\omega}\|_{\ell^2}$ of the vorticity. Hence, the inequality $\|\boldsymbol{\omega}\|_{\ell^\infty} \leq \|\boldsymbol{\omega}\|_{\ell^2}$ on the lattice prevents condition (5.28) to take place. □

5.3 Blowup in incompressible 3D Euler equations

Whether three-dimensional incompressible Euler flow develops a singularity in finite time (also called *blowup*) remains a challenging open mathematical problem. According to the BKM criterion, the singularity implies a spontaneous generation of infinitely large vorticity. Such singularity is anticipated by Kolmogorov's theory of turbulence [69], which predicts that vorticity increments $\delta\omega = |\boldsymbol{\omega}(\mathbf{r}') - \boldsymbol{\omega}(\mathbf{r})|$ diverge at small scales $\ell = |\mathbf{r}' - \mathbf{r}|$ as $\delta\omega \sim \ell^{-2/3}$ when energy is transferred from integral to viscous scales. In this context, blowup could reveal an efficient mechanism for the energy cascade and, for this reason, it is often considered a cornerstone for the theory of turbulence.

In addition to purely mathematical approaches, see *e.g.* [33, 146] and very recent achievements [60, 35], the blowup problem was intensively investigated through Direct

Numerical Simulations (DNS) [72, 76, 82]. However, numerical results appear to be rather inconclusive, with the controversy [91, 83] only growing with the increase of resolution. Naturally, several simplified models have been investigated for understanding possible blowup scenarios, *e.g.* [45, 151, 56, 108]. Despite being rather successful in the study of turbulence [11] and serving as a useful testing ground for mathematical analysis, *e.g.* [90, 37], these models fall short of reproducing basic features of Euler's blowup phenomenon: they lack important properties of Euler's flow, such as incompressibility and conservation of circulation, and often show dynamical behavior atypical for Euler solutions, such as self-similarity [32, 34]. Note that we do not discuss here boundary effects [104], which set a different open problem.

Unlike many previous simplified models, the Euler equations on logarithmic lattices retain most structural properties of the original equations, as we showed in Section 5.1. In the work [29, 26], we presented a numerical evidence of chaotic blowup in the three-dimensional Euler system on a golden-mean logarithmic lattice. Now we extend these previously reported results by testing the robustness of our conclusions on different lattices. For the comparison, we consider the golden mean $\lambda = \varphi$ and the plastic number $\lambda = \sigma$, which provide two lattices $\mathbb{\Lambda}^3$ with increasing resolution—see Fig. 2.2; here, $\mathbb{\Lambda} = \{\pm 1, \pm\lambda, \pm\lambda^2, \dots\}$ is taken, with no zero component. We remark that the spacing factor $\lambda = 2$ does not provide a reliable model for the blowup study, because the incompressibility condition together with a small number of triad interactions cause degeneracies in coupling of different modes.

Numerical model

Aiming for the study of blowup, initial conditions are chosen to have nonzero components limited to large scales, with wavenumbers $1 \le |k_i| \le \varphi^2 = (3+\sqrt{5})/2$. This corresponds to a box of three excited modes in each direction for the golden mean and four modes for the plastic number lattice spacing. The velocities at these modes are explicitly given in the form

$$u_j(\mathbf{k}) = \frac{k_1 k_2 k_3}{k_j} e^{i\theta_j(\mathbf{k}) - |\mathbf{k}|}, \quad \text{for} \quad j = 1, 2. \tag{5.40}$$

Here, the phases θ_j are given by

$$\theta_j(\mathbf{k}) = \operatorname{sgn}(k_1)\alpha_j + \operatorname{sgn}(k_2)\beta_j + \operatorname{sgn}(k_3)\delta_j + \operatorname{sgn}(k_1 k_2 k_3)\gamma_j, \quad \text{for} \quad j = 1, 2, \tag{5.41}$$

with the constants

$$(\alpha_1, \beta_1, \delta_1, \gamma_1) = \tfrac{1}{4}(1, -7, 13, -3) \quad \text{and} \quad (\alpha_2, \beta_2, \delta_2, \gamma_2) = \tfrac{1}{4}(-1, -3, 11, 7). \tag{5.42}$$

The third component u_3 is uniquely defined by the incompressibility condition. The choice of phases avoids undesirable initial symmetries or preferred directions in the flow. Clearly, because the nodes of different lattices do not match, it is impossible to test the same initial condition on different lattices.

Like in usual DNS, we consider the Euler equations in vorticity formulation (5.3), where the velocity field is recovered through the Biot-Savart law (5.4). The equations are integrated numerically with double-precision using the fourth-order Runge-Kutta-Fehlberg adaptive scheme [67]. The time step was dynamically defined in order to keep the relative error for $\omega_{\max}(t) = \max_{\mathbf{k}} |\boldsymbol{\omega}(\mathbf{k}, t)|$ below 10^{-6}. Since only a finite number N of modes in each direction can be simulated, the infinite-dimensional nature of the problem was tracked by implementing the following spatial adaptive scheme. At each time step, we compute the enstrophy $\Omega(t) = \frac{1}{2}(\boldsymbol{\omega}, \boldsymbol{\omega})$ due to the modes with wave vectors $|\mathbf{k}| \geq K_{\max}/\lambda$, where $K_{\max}$ is the largest wave number in each direction. This quantity estimates the enstrophy error (*i.e.*, ℓ^2 norm of vorticity) due to the mode truncation and it was kept below 10^{-15} during the whole simulation. Every time this threshold was reached we increased the number of modes in each direction by five, *i.e.*, multiplying $K_{\max}$ by λ^5. We stopped the simulation for the plastic number with $N = 95$, thus covering a spatial range of $K_{\max} = \sigma^{95} \approx 10^{11}$. Due to the higher spacing value, the golden mean allows to cover a larger spatial range with less modes. In this case, the simulation was stopped with $N = 70$, which corresponds to $K_{\max} = \varphi^{70} \approx 10^{14}$. For the simulations of both lattice spacings, the energy was conserved during the whole time of integration with a relative error below 10^{-6}.

Results

Fig. 5.1 compares the numerical integrations of the Euler equations for golden and plastic lattice spacings. Though solutions are, of course, different at earlier times, they demonstrate very close (numerically indistinguishable) asymptotic blowup dynamics, which we analyze in details now.

Figures 5.1(a) and 5.1(b) show the temporal evolution of the maximum vorticity $\omega_{\max}(t) = \max_{\mathbf{k} \in \mathbb{\Lambda}^3} |\boldsymbol{\omega}(\mathbf{k}, t)|$. BKM blowup criterion—see Theorem 5.5—states that the blowup of the solution at finite time t_b requires that the integral $\int_0^t \omega_{\max}(t)dt$ diverges as $t \to t_b$. In particular, this implies that the growth of maximum vorticity must be at least as fast as $\omega_{\max}(t) \gtrsim (t_b - t)^{-1}$. This is verified for both simulations by plotting the inverse value $1/\omega_{\max}(t)$ in Fig. 5.1(a), providing the blowup times $t_b = 4.255 \pm 0.001$ and $t_b = 10.052 \pm 0.001$ for the plastic number and golden mean, respectively. Fig. 5.1(b) shows the same results in logarithmic scale verifying the asymptotic $\omega_{\max}(t) \sim (t_b - t)^{-1}$.

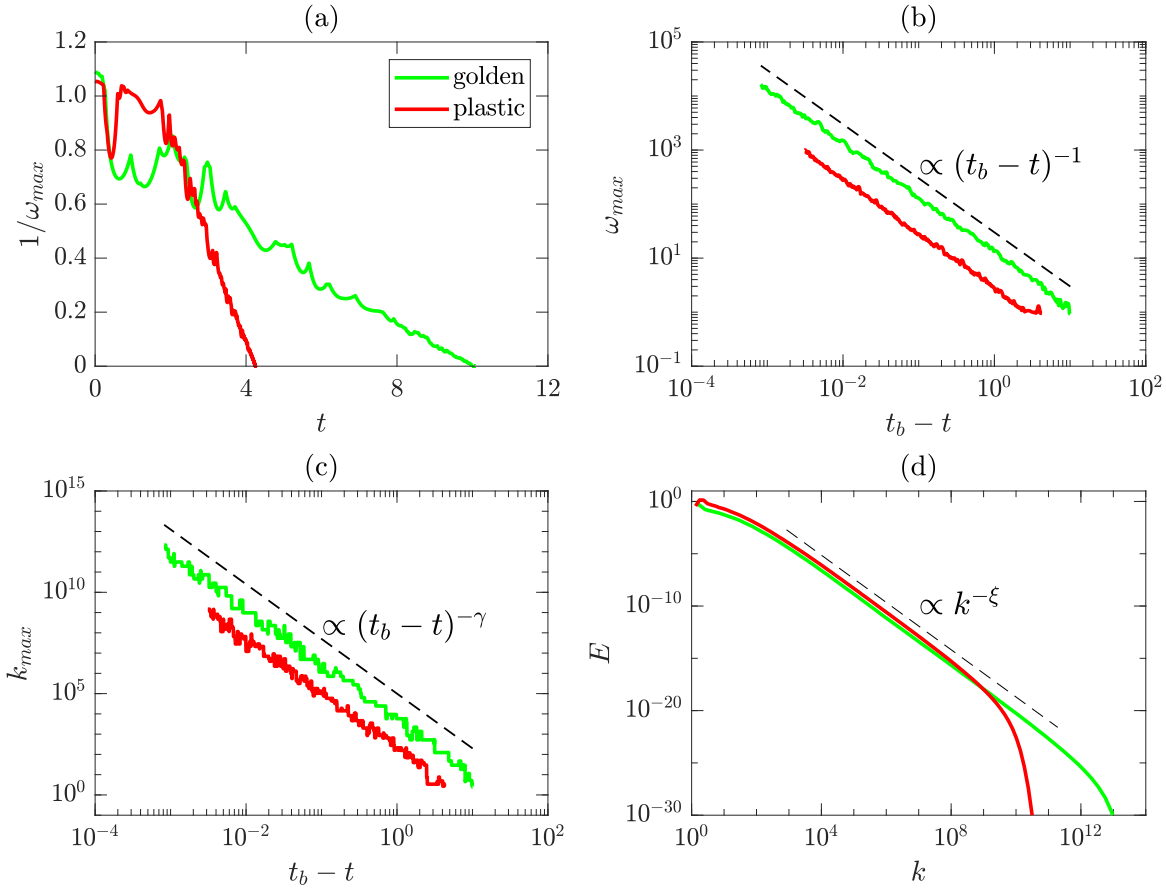

Fig. 5.1 Comparison of the Euler blowup dynamics for different lattice spacings—the golden mean φ in green and plastic number σ in red. Owing to the lower computational cost, the simulation for the golden mean spans a larger spatial range. (a) Dynamic evolution of the inverse maximum vorticity $1/\omega_{\max}$, reaching the blowup times $t_b = 4.255$ and 10.052 for golden and plastic lattice spacings, respectively. (b) The maximum vorticity $\omega_{\max}$ in logarithmic scale fitting in average the power law $\sim (t_b - t)^{-1}$. (c) Wave number $k_{\max}$ where the maximum vorticity occurs in logarithmic scale, following the asymptotic $\sim (t_b - t)^{-\gamma}$ with $\gamma = 2.70$. (d) The energy spectrum (5.43) at the final time of integration for each simulation, developing the power-law $E(k) \propto k^{-\xi}$, where $\xi = 2.26$.

Note that a growth of four orders of magnitude is observed for the golden mean. The wave number $k_{\max}$ at which the maximum vorticity occurs also grows asymptotically as $k_{\max} \sim (t_b - t)^{-\gamma}$ with the same exponent $\gamma = 2.70 \pm 0.01$ for the two simulations, as shown in Fig. 5.1(c). The power-law dependence persists in average up to extremely small physical scales $\ell \sim 1/k_{\max} \sim 10^{-12}$. Finally, Fig. 5.1(d) shows the energy spectrum

$$E(k) = \frac{1}{2\Delta k} \sum_{k \le |\mathbf{k}'| < \lambda k} |\mathbf{u}(\mathbf{k}')|^2, \quad \text{with } \Delta k = \lambda k - k, \tag{5.43}$$

which develops the power law $E(k) \propto k^{-\xi}$ in the energy spectrum as $t \to t_b$. The exponent can be obtained with the dimensional argument $E \propto \omega_{\max}^2 / k_{\max}^3$, which yields $\xi = 3 - 2/\gamma \approx 2.26$, steeper than Kolmogorov's 5/3 for developed turbulence.

Chaotic blowup

The observed scaling agrees with the Leray-type [100] self-similar blowup solution $\boldsymbol{\omega}_L(\mathbf{k}, t)$ defined as

$$\boldsymbol{\omega}_L(\mathbf{k}, t) = (t_b - t)^{-1} \mathbf{W}[(t_b - t)^{\gamma} \mathbf{k}]. \tag{5.44}$$

Such a solution, however, cannot describe the blowup in Fig. 5.1, where the maximum vorticity and the corresponding scale $\ell \sim 1/k_{\max}$ have the power-law behavior only in average, with persistent irregular oscillations.

In order to understand the nonstationary blowup dynamics, we perform the change of coordinates

$$\begin{aligned} \widetilde{\boldsymbol{\omega}} &= (t_b - t)\boldsymbol{\omega}, & \eta &= \log |\mathbf{k}|, \\ \mathbf{o} &= \mathbf{k}/|\mathbf{k}|, & \tau &= -\log(t_b - t). \end{aligned} \tag{5.45}$$

This change of coordinates applies similarly in Fourier space $\mathbb{R}^3$ and in our 3D lattice $\mathbb{A}^3$. With the renormalized variables (5.45), it is convenient to define new differentiation operators as the Fourier factors $\widetilde{\partial}_j = i o_j$, where $\mathbf{o} = (o_1, o_2, o_3) = \mathbf{k}/|\mathbf{k}|$ and i is the imaginary unit. Thus, derivatives in the original and in the renormalized variables are related as $\partial_j = e^{\eta} \widetilde{\partial}_j$. Also, the renormalized velocity can be defined as $\widetilde{\mathbf{u}} = (t_b - t)|\mathbf{k}|\mathbf{u}$, which is related to the renormalized vorticity as

$$\widetilde{\mathbf{u}} = i\mathbf{o} \times \widetilde{\boldsymbol{\omega}}. \tag{5.46}$$

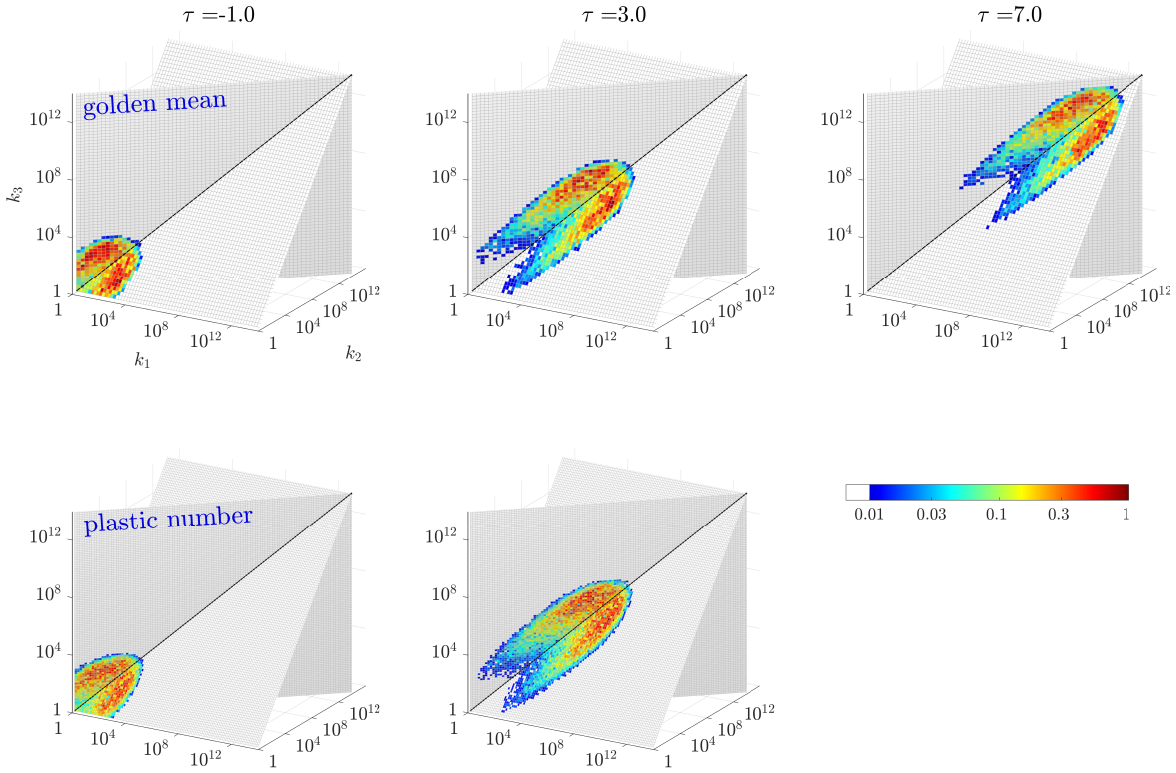

Fig. 5.2 Absolute value of renormalized vorticities $|\widetilde{\boldsymbol{\omega}}|$ plotted on sections of 3D Fourier space, in logarithmic scales, at three different instants τ. For comparison, the vorticities are normalized with respect to their maximum norm $\widetilde{\omega}_{\max}$. Values below 0.01 are plotted in white. The first row shows the evolution on the golden and the second row on the plastic lattice. Owing to the lower computational cost, the simulation for the golden mean was integrated for longer renormalized times τ.

Using relations (5.45) and (5.46), the vorticity equation (5.3), after dropping the common factor $e^{2\tau}$, takes the form

$$\partial_\tau \widetilde{\boldsymbol{\omega}} = G[\widetilde{\boldsymbol{\omega}}], \tag{5.47}$$

where the ith component of the nonlinear operator $G[\widetilde{\boldsymbol{\omega}}]$ is

$$(G[\widetilde{\boldsymbol{\omega}}])_i = -\widetilde{\omega}_i - \widetilde{u}_j * \widetilde{\partial}_j \widetilde{\omega}_i + \widetilde{\omega}_j * \widetilde{\partial}_j \widetilde{u}_i, \quad \widetilde{\partial}_j = i o_j. \tag{5.48}$$

The choice of variables (5.45) is motivated by the scaling invariance: the operator $G[\widetilde{\boldsymbol{\omega}}]$ is homogeneous (invariant to translations) with respect to τ and η, which correspond to temporal and spatial scaling, respectively. In our model, the scaling invariance is represented by the shifts of η with integer multiples of $\log \lambda$. These properties allow studying the blowup as an attractor of system (5.47)—see, *e.g.* [58, 108]. For example, the self-similar blowup solution (5.44) corresponds to the traveling wave $\widetilde{\boldsymbol{\omega}} = \mathbf{W}(e^{\eta-\gamma\tau}\mathbf{o})$, which has a stationary profile in the comoving reference frame $\eta' = \eta - \gamma\tau$. In the limit $\eta \sim \gamma\tau \to \infty$, the original variables (5.45) yield the blowup dynamics: $|\boldsymbol{\omega}| \to \infty$ and $\ell \sim 1/|\mathbf{k}| \to 0$ as $t \to t_b$. Such a blowup is robust to small perturbations if the traveling wave is an attractor in system (5.47).

Irregular evolution observed in Fig. 5.1 suggests that the attractor of system (5.47) cannot be a traveling wave. We will now argue that the attractor in the renormalized system represents a chaotic wave moving with the average speed γ.

Fig. 5.2 shows the time evolution, in renormalized variables, of the solutions on the two different lattices. For the comparison, we plot the vorticities $\widetilde{\boldsymbol{\omega}}$ normalized with respect to their correspondent maximum values $\widetilde{\omega}_{\max}$. The renormalized time for the plastic number is shifted $\tau \mapsto \tau + \tau_0$ by $\tau_0 = -1.2$ for the attractors to be aligned in space.

The solutions in Fig. 5.2 show convergence to waves moving through the main diagonal of Fourier space with the same constant average speed $\eta \sim \gamma\tau$. The waves look surprisingly similar despite the quite distinct resolutions furnished by the two lattices. However, they do not preserve exactly the spatial vorticity distribution. In order to confirm that the wave is chaotic, we computed the largest Lyapunov exponent $\lambda_{\max} = 9.18 \pm 0.07$ in Fig. 5.3: we added a tiny perturbation to the original solution at $\tau = 1.7$, when the attractor is already fully established, and observed the exponential deviation of the solutions $\max_{\mathbf{k}} |\delta\widetilde{\boldsymbol{\omega}}(\tau)| \propto e^{\lambda_{\max}\tau}$ in renormalized time τ. In the original

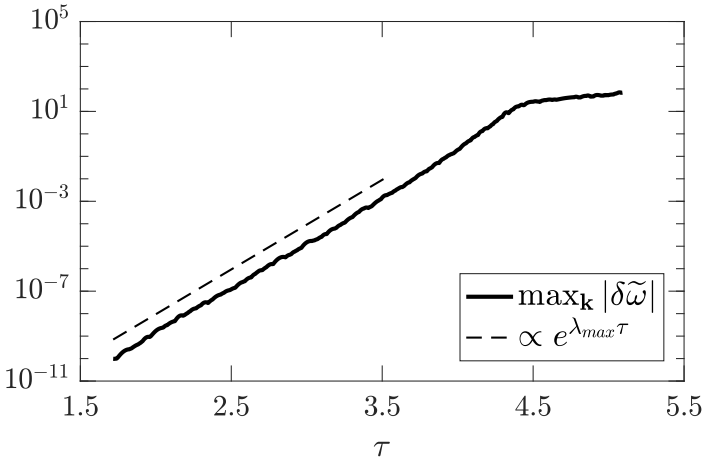

Fig. 5.3 Evolution of a small perturbation of vorticity, $\max_{\mathbf{k}} |\delta\widetilde{\boldsymbol{\omega}}|$, in renormalized variables. Solutions deviate exponentially with the Lyapunov exponent $\lambda_{\max} \approx 9.18$.

variables, this yields the rapid power-law growth

$$\max_{\mathbf{k}} |\delta\boldsymbol{\omega}(t)| \propto (t_b - t)^{-\zeta}, \quad \zeta = \lambda_{\max} + 1 \approx 10.18. \tag{5.49}$$

The chaotic behavior justifies the high sensitivity to perturbations, which is encountered in full DNS [76] and has theoretical foundation in developed turbulence [136]. Instability of blowup solutions is also observed in other simplified models [151, 109, 51] and was proved recently for the full incompressible 3D Euler equations [153].

The striking property of the chaotic attractor is that it restores the isotropy in the statistical sense, even though the solution at each particular moment is essentially anisotropic, in similarity to the recovery of isotropy in the Navier-Stokes turbulence [69, 14]. This property is confirmed in Fig. 5.4 presenting the averages of renormalized vorticity components $|\tilde{\omega}_i|$, considered in the comoving reference frame $\eta' = \eta - \gamma\tau$. The isotropy, as well as other statistical properties, are expected to be established very rapidly in realistic conditions, e.g., in the presence of microscopic fluctuations, because of the very large Lyapunov exponent; see Eq. (5.49). This resembles closely a similar effect in developed turbulence [136].

As one can infer from Figs. 5.2 and 5.4, the chaotic attractor has the span of about six decades of spatial scales. This property imposes fundamental limitations on the numerical resources necessary for the observation of blowup, assuming that the dynamics in the continuous 3D Euler equations can be qualitatively similar to our model. At the respective scales, the solution of the logarithmic model displays properties that can be associated with typical coherent structures of full DNS, *e.g.* the

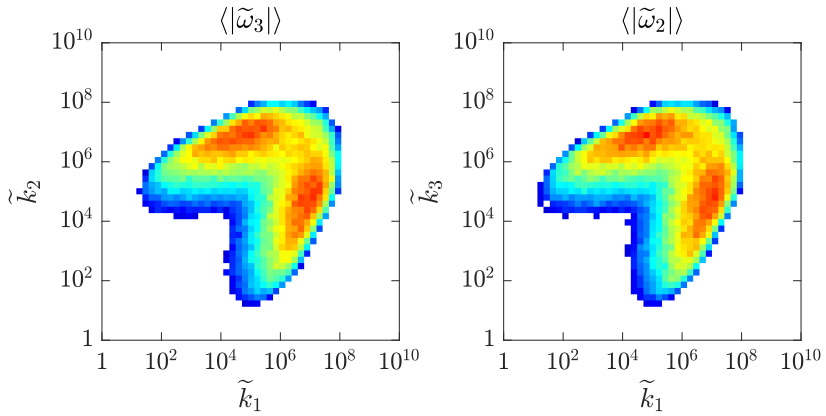

Fig. 5.4 Statistical isotropy: Left panel shows the τ average of $|\widetilde{\omega}_3|$ in a comoving reference frame $\eta' = \eta - \gamma\tau$. Right panel shows analogous result for the average of $|\widetilde{\omega}_2|$ on plane $(\widetilde{k}_1, \widetilde{k}_3)$. Planes of the two figures are related by the 90° rotation about the $\widetilde{k}_3$ axis. Similar results are obtained for other elements of the rotation symmetry group $\mathsf{O_h}$. We plot results for the golden mean lattice spacing.

effect of two-dimensional depletion [133, 17, 70, 3]. For more details on the comparison between logarithmic lattices and DNS, see [29].

Chapter 6

Viscous incompressible flow and turbulence

In this section, we introduce a viscous dissipative term and a forcing $\mathbf{f}$ into the Euler equations (5.2), leading to the incompressible 3D Navier-Stokes equations on a logarithmic lattice

$$\partial_t \mathbf{u} + \mathbf{u} * \nabla \mathbf{u} = -\nabla p + \nu \Delta \mathbf{u} + \mathbf{f}, \quad \nabla \cdot \mathbf{u} = 0, \tag{6.1}$$

where $\nu \geq 0$ is the kinematic viscosity. We will focus on testing some fundamental properties of hydrodynamic turbulence, when the viscous term is responsible for dissipating energy at small scales of the flow while the force injects it at large scales. Following the same lines of derivations as for the continuous model, we deduce the balance for the energy (5.6) as

$$\frac{dE}{dt} = -2\nu\Omega(t) + F(t), \tag{6.2}$$

where $\Omega(t)$ is the enstrophy (5.8) and $F(t) = (\mathbf{u}, \mathbf{f})$ is the work done by external forces. The term $\varepsilon = 2\nu\Omega$ is the total dissipation rate of the flow.

6.1 Anomalous dissipation

A major feature of turbulent flows is the non-vanishing energy dissipation rate $\epsilon > 0$ in the limit of large Reynolds numbers, which can also be formulated mathematically as the limit of vanishing viscosity $\nu \to 0$. This apparently paradoxical phenomenon is known

as *dissipation anomaly* [125, 64] and has found confirmation in many experiments [127] and numerical simulations [87, 68].

Dissipation anomaly is conveniently quantified by considering the evolution of energy through different scales. With the usual procedure—see [69, §2.4]—we derive from Eq. (6.1) the scale-by-scale energy budget equation

$$\partial_t E_k = \Pi_k - 2\nu\Omega_k + F_k. \tag{6.3}$$

Here, using the notation

$$(f,g)_k = \sum_{|\mathbf{k}'|\le k} f(\mathbf{k}')\overline{g(\mathbf{k}')}, \tag{6.4}$$

we have introduced the *cumulative energy* between wave number 0 and k

$$E_k = \frac{1}{2}(\mathbf{u},\mathbf{u})_k, \tag{6.5}$$

the *cumulative enstrophy*

$$\Omega_k = \frac{1}{2}(\boldsymbol{\omega},\boldsymbol{\omega})_k, \tag{6.6}$$

the *cumulative energy injection*

$$F_k = (\mathbf{u},\mathbf{f})_k, \tag{6.7}$$

and the *energy flux*

$$\Pi_k = -(\mathbf{u}, \mathbf{u}*\nabla\mathbf{u} + \nabla p)_k. \tag{6.8}$$

Statistical steady state in a turbulent flow is achieved when $\partial_t\langle E_k\rangle = 0$. In this regime, the mean energy flux $\langle\Pi_k\rangle$ balances with the mean energy dissipation $\langle -2\nu\Omega_k\rangle$ and the work of external forces $\langle F_k\rangle$. Since for small viscosities it is typical to have energy injection confined to large scales and energy dissipation confined to small scales, a dissipation anomaly is related to the development of a constant energy flux in the intermediate range called the *inertial interval*. In our definition, a positive energy flux corresponds to a (direct) cascade of energy from large to small scales.

In order to compute the energy flux, we consider the Navier-Stokes equations (6.1) on the three-dimensional logarithmic lattice of spacing $\lambda = \varphi$, the golden mean. The energy is injected at large scales $\varphi \le |k_{1,2,3}| \le \varphi^3$ through a constant-in-time force with randomly generated components. To obtain an extended inertial interval, the viscous forces $\nu\Delta\mathbf{u}$ were replaced by a hyper-viscous term $-\nu(-\Delta)^h\mathbf{u}$ with $h = 2$. For models with local triad interactions, it is expected that the dynamical statistics are ultraviolet robust, *i.e.*, does not depend on the detailed dissipation mechanism at small scales [8, 107]. The model was integrated with double-precision using the first-order

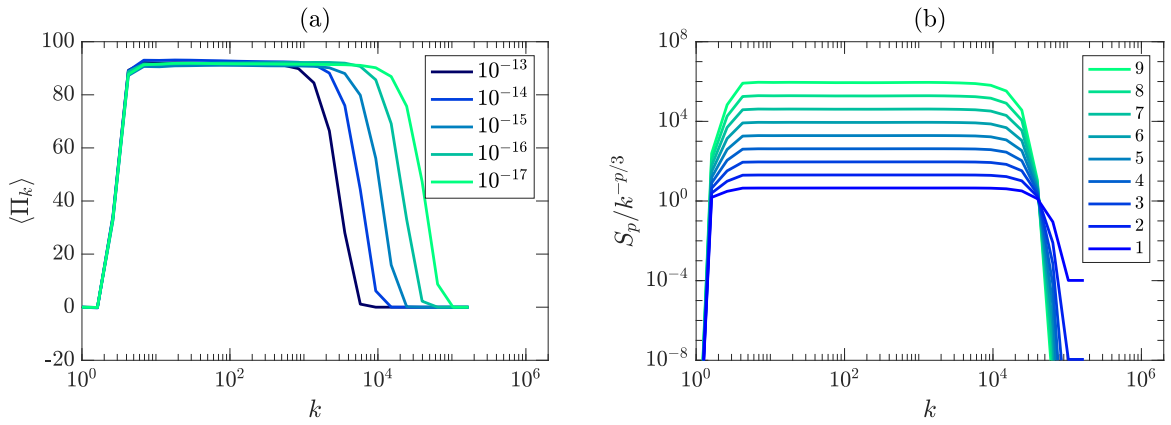

Fig. 6.1 Statistically steady-state solutions of the forced Navier-Stokes equations on the logarithmic lattice. (a) Mean energy flux $\langle \Pi_k \rangle$ along wave numbers k, in logarithmic scale. Distinct curves result from different values of the hyper-viscous parameter $\nu = 10^{-13}$, 10^{-14}, 10^{-15}, 10^{-16} and 10^{-17}. In our convention, a positive energy flux corresponds to a direct cascade of energy. (b) Compensated structure functions $S_p/k^{-p/3}$, defined from the energy flux as functions of the wavenumber k in logarithmic coordinates. Hyper-viscous parameter is $\nu = 10^{-16}$. Distinct curves stand for different powers $p = 1, \ldots, 9$.

exponential time-splitting method [49]: at each time step, we first use the fourth-order Runge-Kutta method to integrate the Euler equations, and next we multiply the resulting solution by the exponential factor $e^{(-\nu|\mathbf{k}|^{2h}\Delta t)}$, where Δt is the time step.

Fig. 6.1(a) shows the mean energy flux $\langle \Pi_k \rangle$ along scales k for different viscosities. The energy flux reaches the same constant positive value for all viscosities, and the inertial range extends to smaller scales as the viscosity decreases, which indicates a dissipation anomaly in the limit $\nu \to 0$.

It turns out that the mean energy spectrum given by (5.43) develops a power-law $\langle E \rangle \propto k^{-\zeta}$ with the exponent $\zeta \approx 1.30$ different from Kolmogorov's 5/3. In fact, a more detailed analysis reveals that this energy spectrum is dominated by the variables with one of the wave vector components much larger than the others, *i.e.*, it is an artifact caused by anisotropy of the model. On the other hand, the analysis of structure functions defined in terms of the energy flux, $S_p(k) = \langle |\Pi_k/k|^{p/3} \rangle$, demonstrates the exact Kolmogorov scaling $S_p \propto k^{-p/3}$, as shown in Fig. 6.1(b).

We continue the analysis of small-scale statistics in the next subsection.

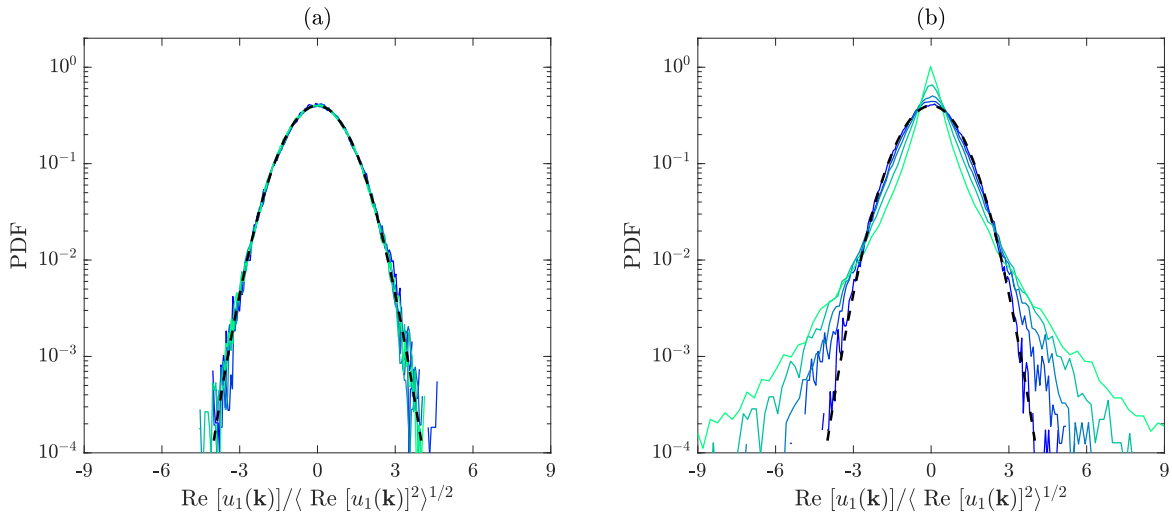

Fig. 6.2 Normalized PDF's in logarithmic scale of the real part of x velocity, $\mathrm{Re}[u_1(\mathbf{k})]$, at different wave vectors $\mathbf{k}_n = \lambda^n \mathbf{k}_0$, $\mathbf{k_0} = (1,1,1)$, rescaled along the main diagonal of Fourier space. Scales decrease from darker to lighter colors. Gaussian distribution of zero mean and unit variance is shown for comparison in black dashed line. (a) Statistics of inertial-range wave vectors $\mathbf{k}_n$, with $n = 10,\ldots,15$; (b) statistics of viscous-range wave vectors $\mathbf{k}_n$, with $n = 18,\ldots,22$.

6.2 Statistics of Fourier modes

The probability distribution functions (PDF's) were numerically estimated through a histogram binning procedure using the statistics accumulated within a sample time T. For this, we use the simulation of viscosity $\nu = 10^{-13}$. In terms of turnover time $T_0 = 1/|\mathbf{k}_0|U_0$, where $\mathbf{k}_0 = (1,1,1)$ is the wave vector of integral scale and $U_0 = \langle|\mathbf{u}(\mathbf{k}_0)|^2\rangle^{1/2}$, the sample time T was larger than $90T_0$. The PDF's of $\mathrm{Re}[u_1(\mathbf{k}_n)]$, in units of their root-mean-square $\langle \mathrm{Re}[u_1(\mathbf{k}_n)]^2\rangle^{1/2}$ values are shown in Fig. 6.2, for several wave vectors $\mathbf{k}_n = \lambda^n \mathbf{k}_0$ rescaled along the main diagonal of Fourier space.

Fig. 6.2(a) shows the statistics at inertial-range wave vectors $\mathbf{k}_n$, for $n = 10,\ldots,15$. The PDF's for all scales are very close to a Gaussian distribution. Similar Gaussian distributions for inertial-range Fourier components were observed for developed turbulence through full DNS [19] and laboratory experiments [131, 120, 40]. For a flow of characteristic large scale L and finite correlation length ℓ in physical space, the univariate statistics of Fourier modes in the inertial range are normally distributed in the asymptotic limit $\ell/L \to 0$, as a particular case of the Central Limit Theorem for weighted integrals [103]. For these reasons, it is commonly argued that Fourier modes are not well suited for the study of extreme events that proportionate inertial-range turbulent intermittency.

Large fluctuations in Fourier modes can only appear when viscous processes become important and initiate a complex interplay between nonlinearity and dissipation. In this regime, the velocity field exhibits strong intermittency, associated with spatial variation of large-scale motion rather than with intense small-scale structures [36]. Unlike what occurs in the inertial range, dissipative intermittency leaves fingerprints on viscous-range Fourier components, whose statistics develop widening of tails at smaller scales [19]. Such behavior is also reproduced by the logarithmic model. Fig. 6.2(b) shows the statistics at viscous-range wave vectors $\mathbf{k}_n$, for $n = 18, \ldots, 22$, where we observe an increasing deviation from Gaussian distribution as we move towards finer scales of the flow.

As presented above, there is a strong similarity between statistics of lattice variables from the logarithmic model and Fourier components of the full Navier-Stokes equations; for instance, compare Figs. 6.2(a,b) of the present paper with Figs. 1(f,b) from the DNS results in [19]. However, it is quite intriguing that the Gaussian behavior in our model is in sharp contrast with statistics of other simplified models, which usually present some degree of inertial-range intermittency. We turn now to a brief discussion about their statistical behavior.

Shell models of turbulence exhibit chaotic intermittent dynamics in the inertial interval with statistical properties close to the Navier-Stokes developed turbulence [73, 123, 105]. On the other hand, the reduced wave vector set approximation (REWA) model displays only weak intermittency [59, 79]. A possible explanation for this feature was given in [19], where it is argued that REWA model can be written in a spherical model framework [119] consisting of N interacting subsystems each one describing the evolution of a velocity component in a certain direction. In this framework, modes should have Gaussian statistics [62] and anomalous fluctuations would be destroyed in the limit $N \to \infty$ [132]. A tendency towards less intermittent regime when increasing the couplings is also observed in the tree models of turbulence [9]. In view of these results, is reasonable to relate the non-intermittent Fourier modes in our model to its rich triad couplings, although no rigorous conclusions can be made. How much Fourier decimation decreases intermittency in physical space is also not clear. This was observed for the Burgers equation with random decimation [25] and for the Navier-Stokes equations, decimating from full to REWA model [79], but not for Sabra model [110], which retains turbulent intermittent dynamics in physical space.

We repeat that the absence of anomalous fluctuations in individual Fourier modes does not mean lack of intermittency in the flow, since this is exactly the scenario for developed turbulence, and because the intermittency is seen in the same way within the

dissipative range. To determine whether our model mimics physical-space intermittency or not, it would be necessary to probe it properly. The challenging question is precisely how to capture intermittency fingerprints on Fourier variables [19], the only available quantities for our model. We leave the more detailed analysis of these interesting but non-trivial questions to future work.

Appendix C

Isentropic compressible flow

The logarithmic models presented in this paper do not extend naturally to isentropic (or general) compressible flow due to the appearance of cubic terms in the governing equations and inviscid invariants. Nevertheless, we present below one possible way to overcome this issue. The idea consists of introducing additional variables properly constrained, so the original cubic terms become quadratic with respect to the extended set of variables. In this formulation, the symmetries and conserved quantities are exactly those from the continuous model. Unfortunately, preliminary numerical simulations do not show good correspondence to dynamical features of realistic compressible flows, such as formation of shock waves. For this reason we restrict ourselves to the model description and its conserved quantities, leaving the numerical implementation for future analysis.

Model

We introduce the scalar density $\rho(\mathbf{k}, t)$, the velocity field $\mathbf{u}(\mathbf{k}, t)$ and the momentum field $\mathbf{q}(\mathbf{k}, t)$, defined on the lattice $\mathbf{k} \in \mathbb{\Lambda}^d$. The model for ideal compressible flow consists of the continuity equation and the balance of momentum together with an algebraic constraint relating all variables, respectively given by the system (*cf.* [98, Sec. 15])

$$\partial_t \rho + \nabla \cdot \mathbf{q} = 0, \quad \partial_t \mathbf{q} = -\nabla \cdot \Pi, \quad \mathbf{q} = \rho * \mathbf{u}, \tag{C.1}$$

where the *momentum flux density* tensor Π has its classical form

$$\Pi_{ij} = p\delta_{ij} + u_i * q_j. \tag{C.2}$$

In an isentropic flow, the pressure p is a function of the density. For our logarithmic model, we consider the quadratic relation

$$p = A\rho * \rho, \tag{C.3}$$

which mimics a polytropic gas $p = A\rho^\gamma$, with $\gamma = 2$.

To evolve model (C.1), one needs to solve the last algebraic constraint for the velocities $\mathbf{u}$, *i.e.*, express it in terms of the momentum and density. This is possible when the mean density $\rho(\mathbf{0}) > 0$ at $\mathbf{k} = \mathbf{0}$ is sufficiently larger than the sum of all other components $\sum_{\mathbf{k}\neq\mathbf{0}} |\rho(\mathbf{k})|$. Under this condition, the density field may be interpreted as small-amplitude oscillations around a positive mean value. Solvability of velocities under this condition can be rigorously proved in proper functional spaces using Operator Theory.

Conserved quantities

The *total momentum* of the flow is naturally defined as

$$M(t) = \mathbf{q}(\mathbf{0}, t), \tag{C.4}$$

at $\mathbf{k} = \mathbf{0}$. The *total energy* E decomposes into two contributions

$$E = K + U, \tag{C.5}$$

where

$$K = \frac{1}{2}(\mathbf{q}, \mathbf{u}) \tag{C.6}$$

is the *kinetic energy* and

$$U = (\rho, e) \tag{C.7}$$

is the *internal energy*. The *internal energy per unit mass* e is defined as

$$e = A\rho. \tag{C.8}$$

Formula (C.8) is obtained from the pressure through the well-known (isentropic) thermodynamical relation $de = pd\rho/\rho^2$.

System (C.1) conserves total momentum (C.4) and total energy (C.5) in time. Kinetic and internal energies are transferred from one another through pressure as

$$\frac{dK}{dt} = -\frac{dU}{dt} = -(\nabla p, \mathbf{u}). \tag{C.9}$$

Viscous effects

Following classical derivations of fluid mechanics, viscosity is introduced in the momentum flux density tensor as

$$\Pi_{ij} = p\delta_{ij} + u_i * q_j - \sigma_{ij}, \tag{C.10}$$

with the *viscous tensor* σ given by

$$\sigma_{ij} = \eta\left(\partial_i u_j + \partial_j u_i - \frac{2}{3}\nabla \cdot \mathbf{u}\delta_{ij}\right) + \zeta\nabla \cdot \mathbf{u}\delta_{ij}. \tag{C.11}$$

The constants $\eta, \zeta \geq 0$ are the *viscosity coefficients*. Non-equilibrium solutions dissipate energy through the work of viscosity forces in the form

$$\frac{dE}{dt} = (\nabla \cdot \sigma, \mathbf{u}). \tag{C.12}$$

In this way, system (C.1) yields equations for the viscous flow.

Appendix D

Functional inequalities on logarithmic lattices

Here we prove some functional inequalities and operator properties used in Section 5.2.

Lemma D.1. *Let* $\mathbf{u} \in h^m$ *and* $\mathbf{v} \in h^{m-1}$, *for* $m \geq 1$. *Then,* $\mathbf{u} * \mathbf{v} = \sum_{i=1}^{d} u_i * v_i \in h^m$ *with*

$$\|\mathbf{u} * \mathbf{v}\|_{h^m} \leq C(\|\mathbf{u}\|_{h^m}\|\mathbf{v}\|_{\ell^\infty} + \|D\mathbf{u}\|_{\ell^\infty}\|\mathbf{v}\|_{h^{m-1}}), \tag{D.1}$$

where C *is a constant which does not depend on* $\mathbf{u}$ *and* $\mathbf{v}$.

Proof. Let us prove the inequality in the one-dimensional case. Using elementary algebraic relations, we obtain

$$\begin{aligned}
\|u * v\|_{h^m}^2 &= \|D^m(u * v)\|_{\ell^2}^2 = \sum_{k \in \mathbb{\Lambda}} |k|^{2m} |(u * v)(k)|^2 \\
&\leq N \sum_{k \in \mathbb{\Lambda}} \sum_{j=1}^{N} |k|^{2m} |u(p_j k) v(q_j k)|^2 \\
&= N \sum_{k \in \mathbb{\Lambda}} \sum_{j=1}^{N} |p_j k + q_j k|^{2m} |u(p_j k) v(q_j k)|^2 \\
&\leq 2^{2m-1} N \sum_{k \in \mathbb{\Lambda}} \sum_{j=1}^{N} (|p_j k|^{2m} + |q_j k|^{2m}) |u(p_j k) v(q_j k)|^2 \\
&= 2^{2m-1} N \sum_{k \in \mathbb{\Lambda}} \sum_{j=1}^{N} |p_j k|^{2m} |u(p_j k) v(q_j k)|^2 + 2^{2m-1} N \sum_{k \in \mathbb{\Lambda}} \sum_{j=1}^{N} |q_j k|^{2m} |u(p_j k) v(q_j k)|^2.
\end{aligned}$$

In the first term, we estimate

$$\sum_{k\in\mathbb{\Lambda}}\sum_{j=1}^{N}|p_jk|^{2m}|u(p_jk)v(q_jk)|^2 \le \|v\|_{\ell^\infty}^2\sum_{j=1}^{N}\sum_{k\in\mathbb{\Lambda}}|p_jk|^{2m}|u(p_jk)|^2 \le N\|u\|_{h^m}^2\|v\|_{\ell^\infty}^2,$$

while the sums of the second term are bounded by

$$\begin{aligned}\sum_{k\in\mathbb{\Lambda}}\sum_{j=1}^{N}|q_jk|^{2m}|u(p_jk)v(q_jk)|^2 &= \sum_{k\in\mathbb{\Lambda}}\sum_{j=1}^{N}|q_jk|^{2m-2}|q_jk|^2|u(p_jk)v(q_jk)|^2\\ &\le M\sum_{k\in\mathbb{\Lambda}}\sum_{j=1}^{N}|q_jk|^{2m-2}|p_jk|^2|u(p_jk)v(q_jk)|^2\\ &\le M\|Du\|_{\ell^\infty}^2\sum_{j=1}^{N}\sum_{k\in\mathbb{\Lambda}}|q_jk|^{2m-2}|v(q_jk)|^2\\ &\le MN\|Du\|_{\ell^\infty}^2\|v\|_{h^{m-1}}^2,\end{aligned}$$

where $M = \max_{j=1,\dots,N}|q_j|^2/|p_j|^2$. In view of the estimates for the two terms, we reach to the result $\|u*v\|_{h^m} \le C\left(\|u\|_{h^m}\|v\|_{\ell^\infty} + \|Du\|_{\ell^\infty}\|v\|_{h^{m-1}}\right)$ with the choice of $C = 2^{m-1/2}N\max(M,1)^{1/2}$. The proof extends naturally to higher dimensions, by considering multiple components. □

Lemma D.2. *Define the bilinear operator*

$$B(\mathbf{u},\mathbf{v}) = \mathbf{u}*\nabla\mathbf{v}, \tag{D.2}$$

where $(\mathbf{u}*\nabla\mathbf{v})_i = \mathbf{u}*\nabla u_i = \sum_{j=1}^{d}u_j*\partial_j v_i$. *Then,* $B : h^m\times h^m \to h^m$ *is a bounded bilinear operator, i.e., there exists a constant* $C>0$ *such that*

$$\|B(\mathbf{u},\mathbf{v})\|_{h^m} \le C\|\mathbf{u}\|_{h^m}\|\mathbf{v}\|_{h^m}, \tag{D.3}$$

for every $\mathbf{u},\mathbf{v}\in h^m$.

Proof. Using inequality (D.1) for $\mathbf{u}$ and ∇v_i, we obtain

$$\|B(\mathbf{u},\mathbf{v})\|_{h^m} \le \sum_{i=1}^{d}\|\mathbf{u}*\nabla v_i\|_{h^m} \le C\sum_{i=1}^{d}\left(\|\mathbf{u}\|_{h^m}\|\nabla v_i\|_{\ell^\infty} + \|D\mathbf{u}\|_{\ell^\infty}\|\nabla v_i\|_{h^{m-1}}\right).$$

We now use the inequalities

$$\|\nabla v_i\|_{\ell^\infty} \le \|D\mathbf{v}\|_{\ell^\infty} \le \|\mathbf{v}\|_{h^1}, \quad \|D\mathbf{u}\|_{\ell^\infty} \le \|\mathbf{u}\|_{h^1}, \quad \|\nabla v_i\|_{h^{m-1}} \le \|\mathbf{v}\|_{h^m}$$

and the general relation

$$\|\mathbf{u}\|_{h^1} \leq \|\mathbf{u}\|_{h^m},$$

which are simple estimates from the definition of the norms on the lattice (5.1). This yields

$$\|B(\mathbf{u},\mathbf{v})\|_{h^m} \leq 2dC\|\mathbf{u}\|_{h^m}\|\mathbf{v}\|_{h^m},$$

which shows that $B(\mathbf{u},\mathbf{v}) \in h^m$ and the boundness of operator B. □

Part III

Flows with boundaries on logarithmic lattices

Chapter 7

Immersed boundary method

Our strategy is to model the solid boundary as a discontinuity surface immersed in the fluid. This will allow us to consider the flow defined everywhere and thus readily work with Fourier variables. Such surface shall be the source of a concentrated force, which is interpreted as the action exerted from the boundary to the fluid. Our approach is based on the discontinuous formulation of the Navier-Stokes equations [142, 137, 143, 74] and inspired by the well-known immersed boundary method [129, 130].

7.1 Discontinuous Navier-Stokes equations

Discontinuous formulations of the Fluid Dynamics equations were first derived in [142] for compressible ideal flows and was subsequently applied to gas dynamics [143], compressible magnetohydrodynamics [137], and in the modelling of no-slip flow boundary for incompressible viscous flow [74]. In this section, we derive the Navier-Stokes equations for viscous incompressible flow in the presence of a discontinuity surface with source distributions. After recalling the Transport Theorem for discontinuity surfaces, we establish the continuity equation followed by the balance of momentum.

Transport Theorem for discontinuity surfaces

Let us consider a moving volume Ω_t of fluid advected by a flow of velocity $\mathbf{u}(\mathbf{x}, t)$. The classical Transport Theorem (consult *e.g.* [42]) balances the variation of smooth quantities on such volume. Given a smooth scalar function $f(\mathbf{x}, t)$, the Theorem states that

$$\frac{d}{dt}\int_{\Omega_t} f(\mathbf{x}, t)d\mathbf{x} = \int_{\Omega_t} \left(\partial_t f + \nabla \cdot (f\mathbf{u})\right) d\mathbf{x}, \tag{7.1}$$

where the term $\int_{\Omega_t} \nabla \cdot (f\mathbf{u}) d\mathbf{x}$ stands for the total flux of f through the moving boundary $\partial\Omega_t$.

Now let us allow f to have a jump discontinuity on a surface $\mathcal{S}_t$ immersed on the flow and moving with velocity $\mathbf{U}(\mathbf{x}, t)$ for $\mathbf{x} \in \mathcal{S}_t$. Assume $\mathcal{S}_t$ splits the volume Ω_t into two subregions Ω_t^- and Ω_t^+. In this case, the balance equation (7.1) becomes

$$\frac{d}{dt}\int_{\Omega_t} f(\mathbf{x},t)d\mathbf{x} = \int_{\Omega_t^-} \left(\partial_t f + \nabla\cdot(f\mathbf{u})\right) d\mathbf{x} + \int_{\Omega_t^+} \left(\partial_t f + \nabla\cdot(f\mathbf{u})\right) d\mathbf{x} + \int_{\mathcal{S}_t\cap\Omega_t} [f(\mathbf{U}-\mathbf{u})\cdot\mathbf{n}]dS, \quad (7.2)$$

where $\mathbf{n}$ is the unit normal vector on $\mathcal{S}_t$ pointing from Ω_t^+ to Ω_t^- and $[f] = f^+ - f^-$ is the jump of f across $\mathcal{S}_t$, with f^+ and f^- the values of f at $\mathcal{S}_t$ from Ω_t^+ and Ω_t^- sides respectively. Formula (7.2) is obtained by applying the original balance equation (7.1) on the two subdomains split by $\mathcal{S}_t$—see Appendix E for details.

Conservation of mass

Representing by $\rho(\mathbf{x}, t)$ the scalar density field, the conservation of mass in a flow in the presence of a discontinuity surface with mass source ξ is given by

$$\frac{d}{dt}\int_{\Omega_t} \rho(\mathbf{x},t)d\mathbf{x} = \int_{\mathcal{S}_t\cap\Omega_t} \xi dS, \quad (7.3)$$

for every volume Ω_t advected by the flow. Applying the discontinuous transport balance (7.2), expression (7.3) is expanded as

$$\int_{\Omega_t^-} \left(\partial_t\rho + \nabla\cdot(\rho\mathbf{u})\right) d\mathbf{x} + \int_{\Omega_t^+} \left(\partial_t\rho + \nabla\cdot(\rho\mathbf{u})\right) d\mathbf{x} + \int_{\mathcal{S}_t\cap\Omega_t} [\rho(\mathbf{U}-\mathbf{u})\cdot\mathbf{n}]dS = \int_{\mathcal{S}_t\cap\Omega_t} \xi dS. \quad (7.4)$$

Since the flow satisfies the continuity equation away from $\mathcal{S}_t$, the first two integrals in (7.4) vanish, and we conclude that the mass source on $\mathcal{S}_t$ equals the jump of mass flow across it as

$$\xi = [\rho(\mathbf{U}-\mathbf{u})\cdot\mathbf{n}]. \quad (7.5)$$

In order to obtain a differential form of equation (7.3), we introduce the Dirac delta $\delta_{\mathcal{S}_t}$ locating $\mathcal{S}_t$ given by

$$\delta_{\mathcal{S}_t}(\mathbf{x}) = \int_{\mathcal{S}_t} \prod_{i=1}^{d} \delta(x_i - y_i) dS(\mathbf{y}), \quad (7.6)$$

where δ is the usual Dirac delta, and d is the spatial dimension. This distribution satisfies

$$\int_{\Omega_t} f\delta_{\mathcal{S}_t} d\mathbf{x} = \int_{\mathcal{S}_t \cap \Omega_t} f dS. \tag{7.7}$$

Therefore, the mass balance (7.3) is written as a singular differential equation

$$\partial_t \rho + \nabla \cdot (\rho \mathbf{u}) = [\rho(\mathbf{U} - \mathbf{u}) \cdot \mathbf{n}]\delta_{\mathcal{S}_t}. \tag{7.8}$$

Now, if we consider the flow to be incompressible with constant density, the conservation of mass reduces to a singular divergence-free condition

$$\nabla \cdot \mathbf{u} = [(\mathbf{U} - \mathbf{u}) \cdot \mathbf{n}]\delta_{\mathcal{S}_t}. \tag{7.9}$$

Balance of momentum

By Newton's second law, the variation of momentum equals external forces. When considering surface stresses only, such forces can be expressed through the action of the stress tensor $\boldsymbol{\sigma}$. Assuming that $\mathcal{S}_t$ has a momentum source distribution $\boldsymbol{\pi}$, we are lead to the following integral balance equation

$$\frac{d}{dt}\int_{\Omega_t} \rho \mathbf{u} d\mathbf{x} = \int_{\partial\Omega_t} \boldsymbol{\sigma} \cdot \mathbf{n} dS + \int_{\mathcal{S}_t \cap \Omega_t} \boldsymbol{\pi} dS, \tag{7.10}$$

for every volume Ω_t advected by the flow.

Application of the discontinuous transport equation (7.2) on the left term of (7.10) yields

$$\begin{aligned}\frac{d}{dt}\int_{\Omega_t} \rho \mathbf{u} d\mathbf{x} = &\int_{\Omega_t^-} (\partial_t(\rho\mathbf{u}) + \nabla \cdot (\rho \mathbf{u} \otimes \mathbf{u}))d\mathbf{x} \\ &+ \int_{\Omega_t^+} (\partial_t(\rho\mathbf{u}) + \nabla \cdot (\rho \mathbf{u} \otimes \mathbf{u}))d\mathbf{x} + \int_{\mathcal{S}_t \cap \Omega_t} [\rho\mathbf{u}(\mathbf{U} - \mathbf{u}) \cdot \mathbf{n}]dS,\end{aligned} \tag{7.11}$$

where we have used the tensor product notation $(\mathbf{u} \otimes \mathbf{v})_{ij} = u_i v_j$.

The stress term in Eq. (7.10) is computed from the Divergence Theorem for discontinuity surfaces—see Appendix E—as

$$\int_{\partial\Omega_t} \boldsymbol{\sigma} \cdot \mathbf{n} dS = \int_{\Omega_t^-} \nabla \cdot \boldsymbol{\sigma} d\mathbf{x} + \int_{\Omega_t^+} \nabla \cdot \boldsymbol{\sigma} d\mathbf{x} - \int_{\mathcal{S}_t \cap \Omega_t} [\boldsymbol{\sigma} \cdot \mathbf{n}] dS. \tag{7.12}$$

Substitution of (7.11) and (7.12) in the balance of momentum (7.10) leads to

$$\int_{\Omega_t^-}(\partial_t(\rho\mathbf{u})+\nabla\cdot(\rho\mathbf{u}\otimes\mathbf{u})-\nabla\cdot\boldsymbol{\sigma})d\mathbf{x}+\int_{\Omega_t^+}(\partial_t(\rho\mathbf{u})+\nabla\cdot(\rho\mathbf{u}\otimes\mathbf{u})-\nabla\cdot\boldsymbol{\sigma})d\mathbf{x}$$
$$+\int_{\mathcal{S}_t\cap\Omega_t}[\boldsymbol{\sigma}\cdot\mathbf{n}+\rho\mathbf{u}(\mathbf{U}-\mathbf{u})\cdot\mathbf{n}]dS=\int_{\mathcal{S}_t\cap\Omega_t}\boldsymbol{\pi}dS. \quad (7.13)$$

Away from $\mathcal{S}_t$, the flow satisfies the classical Navier-Stokes equations, so the first two integrals in (7.13) vanish, and we obtain a relation between the momentum source on $\mathcal{S}_t$ and the jumps

$$\boldsymbol{\pi}=[\boldsymbol{\sigma}\cdot\mathbf{n}+\rho\mathbf{u}(\mathbf{U}-\mathbf{u})\cdot\mathbf{n}]. \quad (7.14)$$

After employing the Dirac delta (7.6), Eq, (7.10) is written in the singular differential form

$$\partial_t(\rho\mathbf{u})+\nabla\cdot(\rho\mathbf{u}\otimes\mathbf{u})-\nabla\cdot\boldsymbol{\sigma}=[\boldsymbol{\sigma}\cdot\mathbf{n}+\rho\mathbf{u}(\mathbf{U}-\mathbf{u})\cdot\mathbf{n}]\delta(\mathcal{S}_t). \quad (7.15)$$

We assume the flow to be incompressible with homogeneous density, which we set to unity $\rho=1$. For a Newtonian fluid, the stress tensor is given by

$$\sigma_{ij}=-p\delta_{ij}+\nu(\partial_i u_j+\partial_j u_i), \quad (7.16)$$

where $\nu\geq 0$ is the kinematic viscosity, p is the hydrodynamic pressure, and δ_{ij} is the Kronecker delta. Under these assumptions, the momentum balance law (7.15) is simplified to

$$\partial_t\mathbf{u}+\mathbf{u}\cdot\nabla\mathbf{u}=-\nabla p+\nu\Delta\mathbf{u}+[\boldsymbol{\sigma}\cdot\mathbf{n}+\mathbf{u}(\mathbf{U}-\mathbf{u})\cdot\mathbf{n}]\delta_{\mathcal{S}_t}, \quad (7.17)$$

which, together with the singular divergence free condition (7.9), constitutes the *discontinuous Navier-Stokes equations* for incompressible flow.

Our aim in the next sections is to express conditions at solid boundaries as discontinuity surfaces. In this case, the flow satisfies the no-penetration condition

$$(\mathbf{U}-\mathbf{u})\cdot\mathbf{n}=0 \quad \text{on } \mathcal{S}_t. \quad (7.18)$$

and the final system of equations becomes

$$\partial_t\mathbf{u}+\mathbf{u}\cdot\nabla\mathbf{u}=-\nabla p+\nu\Delta\mathbf{u}+[\boldsymbol{\sigma}\cdot\mathbf{n}]\delta_{\mathcal{S}_t}, \quad \nabla\cdot\mathbf{u}=0. \quad (7.19)$$

7.2 Modeling solid boundaries as discontinuity surfaces

We consider a three-dimensional velocity field $\mathbf{u}(x, y, z) = (u, v, w)$ in the upper-half volume $y > 0$ with a steady solid boundary on the plane $y = 0$. Viscous incompressible flow in this domain is governed by the classical Navier-Stokes equations together with no-slip boundary condition

$$\begin{cases} \partial_t \mathbf{u} + \mathbf{u} \cdot \nabla \mathbf{u} = -\nabla p + \nu \Delta \mathbf{u} & \text{in } y > 0, \\ \nabla \cdot \mathbf{u} = 0 & \text{in } y > 0, \\ \mathbf{u} = \mathbf{0} & \text{on } y = 0. \end{cases} \tag{7.20}$$

System (7.20) also approximates the governing set of equations for smooth boundaries of more general geometries, when considering the flow in a small vicinity of a boundary point taken as the origin in local Cartesian coordinates.

Our goal is to deduce a system equivalent to (7.20), but with the field variables u, v, w and p defined everywhere. A simple way to achieve this is by extending the flow to the lower-half volume through the symmetries

$$\begin{aligned} u(x, y, z, t) &= \quad u(x, -y, z, t), \\ v(x, y, z, t) &= -v(x, -y, z, t), \\ w(x, y, z, t) &= \quad w(x, -y, z, t), \\ p(x, y, z, t) &= \quad p(x, -y, z, t), \end{aligned} \tag{7.21}$$

for all x, y, z and t. Observe that, because of the parity of v, any symmetric field (7.21) immediately satisfies the no-penetration condition on the boundary

$$v = 0 \text{ at } y = 0. \tag{7.22}$$

However, in performing such extension, we might have introduced singularities in the system. More precisely, the resulting reflected field variables may present jump discontinuities in their derivatives accross the solid boundary. Therefore, we should consider the axis $y = 0$ as a steady discontinuity surface, and the balance laws must take the jump singularities into account. The governing equations we have to consider are the discontinuous formulation of the Navier-Stokes equations (7.19), deduced in Section 7.1. In our framework, we can compute the singular term $[\boldsymbol{\sigma} \cdot \mathbf{n}]\delta_{\mathcal{S}_t}$ explicitly.

Let us establish the contribution of the jump singularities on the governing equations. First, we set the upper-half volume $y > 0$ as being the positive domain split by the discontinuity surface $y = 0$, while the lower-half volume $y < 0$ is its negative counterpart. Following the convention established in Section 7.1, the unit normal vector at $y = 0$ pointing from the positive towards the negative domains is $\mathbf{n} = (0, -1, 0)^T$. Next, the stress tensor (7.16) on $y = 0$ is given by

$$\boldsymbol{\sigma} = \begin{pmatrix} -p & \nu\partial_y u & 0 \\ \nu\partial_y u & -p + 2\nu\partial_y v & \nu\partial_y w \\ 0 & \nu\partial_y w & -p \end{pmatrix} \quad \text{on } y = 0, \tag{7.23}$$

where we have used the no-slip boundary condition $\mathbf{u} = \mathbf{0}$ on the x-z plane to neglect all terms involving spatial derivatives in x and z directions, that is $\partial_x u = \partial_x v = \partial_x w = \partial_z u = \partial_z v = \partial_z w = 0$ on $y = 0$. Hence,

$$\boldsymbol{\sigma} \cdot \mathbf{n} = \begin{pmatrix} -\nu\partial_y u \\ p - 2\nu\partial_y v \\ -\nu\partial_y w \end{pmatrix} \quad \text{on } y = 0. \tag{7.24}$$

Finally, because of the symmetries (7.21) on p and v, we have $[p] = [\partial_y v] = 0$, so we obtain

$$[\boldsymbol{\sigma} \cdot \mathbf{n}] = \begin{pmatrix} -\nu[\partial_y u] \\ 0 \\ -\nu[\partial_y w] \end{pmatrix}. \tag{7.25}$$

The system of governing equations for the reflected flow becomes

$$\begin{cases} \partial_t \mathbf{u} + \mathbf{u} \cdot \nabla \mathbf{u} = -\nabla p + \nu \Delta \mathbf{u} - \nu \mathbf{J}(x, z, t)\delta(y) & \text{in } \mathbb{R}^3, \\ \nabla \cdot \mathbf{u} = 0 & \text{in } \mathbb{R}^3, \\ \mathbf{u} = \mathbf{0} & \text{on } y = 0, \\ + \text{ symmetries (7.21)}. \end{cases} \tag{7.26}$$

It follows from Eq. (7.25) that the jump $\mathbf{J}$ is given by

$$\mathbf{J} = \begin{pmatrix} [\partial_y u] \\ 0 \\ [\partial_y w] \end{pmatrix}. \tag{7.27}$$

The concentrated force $-\nu\mathbf{J}(x,z,t)\delta(y)$ is the shear action exerted by the solid plate on the fluid and is responsible for relaxing the flow velocity $\mathbf{u}$ (more precisely, components u and w) to zero on the disontinuity surface $y=0$.

Just as pressure is obtained from incompressibility, the new jump variable $\mathbf{J}$ is determined from the no-slip condition, as we are going to see in the next subsection. In fact, one can prove uniqueness of strong solutions from the same initial data for system (7.26). By a strong solution of (7.26), we understand a continuous flow which is smooth away from the boundary and has finite energy. One can prove such uniqueness by undertaking energy methods from classical Navier-Stokes analysis—like the estimates in [113, pp. 87–90]—and noting that terms associated with the additional concentrated force are going to vanish due to the restriction $u=w=0$ on $y=0$. This argument also attest the necessity of imposing the no-slip condition on the discontinuity surface for the uniqueness of solutions. Indeed, the no-slip condition cannot be lifted up from the set of equations (7.26), otherwise the resulting system would be ill-posed—see Appendix F for an example of nonunique solutions from the same initial data when no-slip condition is not explicitly prescribed.

Following the steps of this section, we have shown that any solution of the original governing equations (7.20), once reflected on the lower-half plane through symmetries (7.21), is going to be a solution of the discontinuous formulation (7.26). On the other hand, the aforementioned uniqueness property of equations (7.26) implies the converse, *i.e.* solutions of the discontinuos system (7.26), taking $\mathbf{u}$, p and $\mathbf{J}$ as variables, when restricted to the upper-half plane, are solutions of the original governing equations (7.20). We conclude that the two systems are equivalent.

In the inviscid case $\nu=0$, we simplify (7.26) to the *incompressible Euler equations*

$$\begin{cases} \partial_t\mathbf{u}+\mathbf{u}\cdot\nabla\mathbf{u}=-\nabla p & \text{in } \mathbb{R}^3, \\ \nabla\cdot\mathbf{u}=0 & \text{in } \mathbb{R}^3, \\ +\text{ symmetries (7.21)}. \end{cases} \tag{7.28}$$

In this system, no penetration

$$v=0 \quad \text{in } y=0 \tag{7.29}$$

is satisfied as a consequence of the flow symmetry, while the flow may slip through the boundary, *i.e.* $u\neq 0$ and $w\neq 0$ on $y=0$.

7.3 Computation of the jump discontinuity

As we demonstrated in the later section, the jump formulation (7.26) for our boundary problem is well-posed considering the unknown variables $\mathbf{u}$, p and $\mathbf{J}$. It follows that the jump $\mathbf{J}$ is fully determined from the system. In literature, the jumps have been numerically computed by means of control theory [74] or other computational methods [129, 130], but they are explicitly evaluated only for simple flows [142, 143]. Here we deduce a new closed formula in a limit sense, which is applicable to any flow. The strategy is to approximate system (7.26) by considering approximations of the Dirac delta function, and then taking the proper limit. Such strategy shall be used again in the computation of jumps on logarithmic lattices in the next sections.

Approximation of Dirac delta

Let us introduce an approximation of Dirac delta, or, as it is commonly called in the Theory of Distributions, an approximation of identity. Take a positive small parameter $\varepsilon > 0$ and consider the exponential function

$$\delta^{\varepsilon}(y) = \frac{1}{\varepsilon\sqrt{\pi}} e^{-y^2/\varepsilon^2}. \tag{7.30}$$

Such function has unit mass

$$\int \delta^{\varepsilon} dy = 1 \quad \forall \varepsilon > 0, \tag{7.31}$$

and it converges to Dirac delta

$$\delta^{\varepsilon} \to \delta \quad \text{as } \varepsilon \to 0 \tag{7.32}$$

in the sense of distributions, *i.e.*

$$(\delta^{\varepsilon}, f) \to f(0) \quad \text{as } \varepsilon \to 0, \quad \text{for all continuous } f, \tag{7.33}$$

where $(f, g) = \int fg dy$ is the L^2-inner product.

Approximated system

With an approximation δ^ε of Dirac delta in hand, we introduce the approximated system

$$\begin{cases} \partial_t \mathbf{u}^\varepsilon + \mathbf{u}^\varepsilon \cdot \nabla \mathbf{u}^\varepsilon = -\nabla p^\varepsilon + \nu \Delta \mathbf{u}^\varepsilon - \nu \mathbf{J}^\varepsilon(x,z,t)\delta^\varepsilon(y) & \text{in } \mathbb{R}^3, \\ \nabla \cdot \mathbf{u}^\varepsilon = 0 & \text{in } \mathbb{R}^3, \\ (\mathbf{u}^\varepsilon, \delta^\varepsilon)_y = \mathbf{0} & \text{for all } x \text{ and } z, \\ + \text{ symmetries (7.21)}. \end{cases} \tag{7.34}$$

Here, $(f,g)_y = \int f g dy$ is the L^2-inner product in variable y only.

Some remarks should be addressed. In this approximated system, the discontinuity surface is not anymore sharply located. As a consequence, the boundary force $-\nu \mathbf{J}^\varepsilon(x,z,t)\delta^\varepsilon(y)$ is not concentrated on the plane $y = 0$, but it is diffuse along a bandwidth determined by δ^ε, whose width becomes thinner and thinner as $\varepsilon \to 0$. Accordingly, we do not demand the no-slip boundary condition to be satisfied on $y = 0$, but in the diffuse form given in Eqs. (7.34). Observe that the exact no-slip boundary condition is readily recovered in the vanishing approximation limit, since

$$(\mathbf{u}^\varepsilon, \delta^\varepsilon)_y \to (\mathbf{u}, \delta)_y = \mathbf{u}|_{y=0} \quad \text{as } \varepsilon \to 0. \tag{7.35}$$

Moreover, this condition guarantees that the approximated boundary force exerts no work in the flow, since

$$\nu(\mathbf{u}^\varepsilon, \mathbf{J}^\varepsilon \delta^\epsilon) = \nu \iint (\mathbf{u}^\varepsilon, \delta^\varepsilon)_y \cdot \mathbf{J}^\varepsilon(x,z,t) dx dz = 0. \tag{7.36}$$

Computation of the jump discontinuities

For this approximated system, we can compute explicitly the jumps $\mathbf{J}^\varepsilon$. Since the approximated Dirac delta is a smooth function, we can take the y-inner product of the momentum equation in (7.34) with δ^ε. We use the condition $(\mathbf{u}^\varepsilon, \delta^\varepsilon)_y = \mathbf{0}$ to neglect the trivial term $(\partial_t \mathbf{u}^\varepsilon, \delta^\varepsilon)_y = \mathbf{0}$. The result follows

$$(\mathbf{u}^\varepsilon \cdot \nabla \mathbf{u}^\varepsilon + \nabla p^\varepsilon - \nu \Delta \mathbf{u}^\varepsilon, \delta^\varepsilon)_y = (-\nu \mathbf{J}^\varepsilon \delta^\varepsilon, \delta^\varepsilon)_y. \tag{7.37}$$

Noting that the regularized jumps $\mathbf{J}^\varepsilon$ do not depend on variable y, the y-inner product on the right-hand side of (7.37) is expanded as

$$(-\nu\mathbf{J}^\varepsilon\delta^\varepsilon, \delta^\varepsilon)_y = -\nu\mathbf{J}^\varepsilon(x,z,t)(\delta^\varepsilon, \delta^\varepsilon)_y. \tag{7.38}$$

Observe that, since δ^ε is a smooth function, the product $(\delta^\varepsilon, \delta^\varepsilon)_y$ is well-defined. For the approximated delta (7.30), it values

$$(\delta^\varepsilon, \delta^\varepsilon)_y = \frac{1}{\varepsilon\sqrt{2\pi}}. \tag{7.39}$$

Substituting the force term (7.38) in Eq. (7.37), we can isolate the regularized jumps $\mathbf{J}^\varepsilon$ as

$$\mathbf{J}^\varepsilon(x,z,t) = \frac{1}{\nu(\delta^\varepsilon, \delta^\varepsilon)_y}(-\mathbf{u}^\varepsilon \cdot \nabla\mathbf{u}^\varepsilon - \nabla p^\varepsilon + \nu\Delta\mathbf{u}^\varepsilon, \delta^\varepsilon)_y. \tag{7.40}$$

Observe, for instance, that the flow symmetries (7.21) in v imply that the y-component J_y^ε of the regularized jumps is identically zero.

The original jumps $\mathbf{J}$ in Eq. (7.26) are recovered as the limit of regularized jumps $\mathbf{J}^\varepsilon$ in the form

$$\mathbf{J}(x,z,t) = \lim_{\varepsilon\searrow 0}\mathbf{J}^\varepsilon = \lim_{\varepsilon\searrow 0}\frac{1}{\nu(\delta^\varepsilon, \delta^\varepsilon)_y}(-\mathbf{u}^\varepsilon \cdot \nabla\mathbf{u}^\varepsilon - \nabla p^\varepsilon + \nu\Delta\mathbf{u}^\varepsilon, \delta^\varepsilon)_y. \tag{7.41}$$

Chapter 8

Boundaries on logarithmic lattices

In this chapter, we show how to add solid boundaries to the logarithmic models of the Euler and Navier-Stokes equations. The strategy here is to apply our usual logarithmic lattice techniques to the jump formulation of incompressible flow, deduced in the previous Chapter 7. Because the equations are written for the whole space, such model is readily translated into Fourier variables, and so to logarithmic lattices. The no-slip boundary condition is encoded through the inner product of the velocity field against the Dirac delta, which is well-defined in our framework. The shear force at the boundary is explicitly computed as a limit of an approximation parameter, just as in the discontinuous model of Section 7.3. Regularization on the lattice is simply truncation.

For the subsequent development, we shall consider a three-dimensional logarithmic lattice $\mathbb{\Lambda}^3$, where

$$\mathbb{\Lambda} = \{\pm 1, \pm\lambda, \pm\lambda^2, \dots\}, \tag{8.1}$$

for some λ from Theorem 2.1. As usual, this lattice mimics Fourier space with largest integral scale $L \sim 2\pi$ corresponding to $|\mathbf{k}| \sim 1$. Some specific statements below, however, will be suitable only for the lattice with zero component $\mathbb{\Lambda} = \{0, \pm 1, \pm\lambda, \pm\lambda^2, \dots\}$. In those cases, the necessity of this additional point will be addressed in the text.

8.1 Governing equations

As we did for the flows without boundaries in Chapters 5 and 6, we represent the velocity field $\mathbf{u}(\mathbf{k}, t) = (u, v, w) \in \mathbb{C}^3$ as a function of the wave vector $\mathbf{k} = (k_x, k_y, k_z) \in \mathbb{\Lambda}^3$ on the logarithmic lattice and the time variable $t \in \mathbb{R}$. Similarly, we have the scalar

pressure $p(\mathbf{k}, t) \in \mathbb{C}$. These and all field variables are supposed to satisfy the reality condition (3.1).

In physical space, the flow is reflected with respect to the plane $y = 0$ as in (7.21). Accordingly, we demand the lattice fields to satisfy the corresponding symmetries

$$\begin{aligned} u(k_x, k_y, k_z, t) &= \quad u(k_x, -k_y, k_z, t), \\ v(k_x, k_y, k_z, t) &= -v(k_x, -k_y, k_z, t), \\ w(k_x, k_y, k_z, t) &= \quad w(k_x, -k_y, k_z, t), \\ p(k_x, k_y, k_z, t) &= \quad p(k_x, -k_y, k_z, t), \end{aligned} \tag{8.2}$$

for all k_x, k_y, k_z and t.

We have also to consider the action of the shear force at the boundary $\mathbf{F} = (F_x, F_y, F_z)$ on the flow, which is related to the jump discontinuities $\mathbf{J} = (J_x, J_y, J_z)$ in the form

$$\mathbf{F}(\mathbf{k}, t) = -\nu \mathbf{J}(k_x, k_z, t)\delta(k_y). \tag{8.3}$$

Since the jump discontinuities in physical space occur at the plane $y = 0$, the corresponding lattice variable is a function independent of k_y, and thus depend on k_x, k_z and t only. In analogy with the Fourier transform of Dirac delta distribution, we take the lattice Dirac delta function $\delta(k_y)$ as unity

$$\delta(k_y) = 1 \quad \text{for all } k_y \in \mathbb{\Lambda}. \tag{8.4}$$

Such natural definition preserves some important properties of Dirac delta, like scaling invariance

$$\delta(\lambda k_y) = \delta(k_y) \tag{8.5}$$

and parity

$$\delta(-k_y) = \delta(k_y). \tag{8.6}$$

Moreover, Dirac delta (8.4) on the lattice keeps similarity with a classical property of the original distribution: if $f(k_y)$ is a lattice function representing a function $F(y)$ in physical space, then its k_y-inner product against delta mimics the localization of F on $y = 0$, since

$$(f, \delta)_{k_y} = \sum_{k_y \in \mathbb{\Lambda}} f(k_y)\overline{\delta(k_y)} = \sum_{k_y \in \mathbb{\Lambda}} f(k_y) \simeq \int \hat{F}(k_y) dk_y = F(y)\Big|_{y=0}. \tag{8.7}$$

Here the left-hand side of $\simeq$ corresponds to a logarithmic lattice representation $k_y \in \mathbb{\Lambda}$, and the right-hand side corresponds to a usual representation in continuous space $y \in \mathbb{R}$. This interpretation allows us to impose the no-slip boundary condition in the form

$$(\mathbf{u}, \delta)_{k_y} \equiv \mathbf{0}, \tag{8.8}$$

since we interpret

$$(\mathbf{u}, \delta)_{k_y} \simeq \mathbf{u}\Big|_{y=0}. \tag{8.9}$$

Observe that the left expression in Eq. (8.8) is a function of k_x, k_z and t.

With all the above definitions, we can now establish the *incompressible Navier-Stokes equations for a flat solid boundary on a logarithmic lattice*. We simply write the discontinuous formulation of the Navier-Stokes equations (7.26), but considering the operations on logarithmic lattices

$$\begin{cases} \partial_t \mathbf{u} + \mathbf{u} * \nabla \mathbf{u} = -\nabla p + \nu \Delta \mathbf{u} - \nu \mathbf{J}(k_x, k_z, t)\delta(k_y) & \text{in } \mathbb{\Lambda}^3, \\ \nabla \cdot \mathbf{u} = 0 & \text{in } \mathbb{\Lambda}^3, \\ (\mathbf{u}, \delta)_{k_y} = \mathbf{0} & \text{for all } k_x, k_z, t, \\ + \text{ symmetries (8.2)}. \end{cases} \tag{8.10}$$

The corresponding *incompressible Euler equations for a flat solid boundary on a logarithmic lattice* reads

$$\begin{cases} \partial_t \mathbf{u} + \mathbf{u} * \nabla \mathbf{u} = -\nabla p & \text{in } \mathbb{\Lambda}^3, \\ \nabla \cdot \mathbf{u} = 0 & \text{in } \mathbb{\Lambda}^3, \\ + \text{ symmetries (8.2)}. \end{cases} \tag{8.11}$$

In this case, the no-penetration boundary condition $(v, \delta)_{k_y} = 0$ is a consequence of the symmetry $v(-k_y) = -v(-k_y)$ on v from (8.2).

Taking the divergence of the momentum equation in (8.10) and invoking incompressibility, we obtain a Poisson equation for the pressure

$$\Delta p = -\nabla \cdot (\mathbf{u} * \nabla \mathbf{u}) - \nu \nabla \cdot (\mathbf{J}(k_x, k_z, t)\delta(k_y)). \tag{8.12}$$

This allows us to eliminate the pressure from system (8.10). Observe, however, that the pressure is written as a function of not only the velocities, but of the jumps as

well. The additional term $-\nu\nabla\cdot(\mathbf{J}(k_x,k_z,t)\delta(k_y))$ in pressure's equation stands for the contribution of the boundary.

8.2 Computation of the jump lattice variable

We shall proceed as in Section 7.3. Regularization in Fourier space is easily achieved by cutting-off high frequencies. When considering a discrete set of wave vectors, this is truncation. Let us limit the highest frequencies of the lattice by the wave number $k_N=\lambda^N$ as

$$\mathbb{\Lambda}_N=\{\pm1,\pm\lambda,\pm\lambda^2,\dots,\pm\lambda^N\}. \tag{8.13}$$

Then, the Dirac delta on the lattice (8.4) is automatically "regularized", since truncation turns it into a summable function.

Then we consider the approximated system

$$\begin{cases}\partial_t\mathbf{u}^N+\mathbf{u}^N*\nabla\mathbf{u}^N=-\nabla p^N+\nu\Delta\mathbf{u}^N-\nu\mathbf{J}^N(k_x,k_z,t)\delta^N(k_y) & \text{in } \mathbb{\Lambda}_N^3,\\ \nabla\cdot\mathbf{u}^N=0 & \text{in } \mathbb{\Lambda}_N^3,\\ (\mathbf{u}^N,\delta^N)_{k_y}=\mathbf{0} & \text{for all } k_x,k_z,t,\\ +\text{ symmetries (8.2).}\end{cases} \tag{8.14}$$

We wrote the upper-script N to indicate all regularized variables, *i.e.* those defined on the truncated lattice (8.13).

To compute the regularized jumps $\mathbf{J}^N$, we take the k_y-inner product of the momentum equation with δ^N. As a consequence of no-slip condition, the contribution of time variation vanishes, and we are lead to

$$(\mathbf{u}^N*\nabla\mathbf{u}^N,\delta^N)_{k_y}=(-\nabla p^N+\nu\Delta\mathbf{u}^N,\delta^N)_{k_y}+(-\nu\mathbf{J}^N(k_x,k_z,t)\delta^N(k_y),\delta^N)_{k_y}. \tag{8.15}$$

Using the fact that the jumps $\mathbf{J}^N$ do not depend on k_y, one may write

$$(-\nu\mathbf{J}^N(k_x,k_z,t)\delta^N(k_y),\delta^N)_{k_y}=-\nu\mathbf{J}^N(k_x,k_z,t)(\delta^N,\delta^N)_{k_y}. \tag{8.16}$$

Because the approximated truncated δ^N is summable, the product $(\delta^N,\delta^N)_{k_y}$ appearing in Eq. (8.16) is a well-defined positive number. Substitution of expression (8.16) into Eq. (8.15) yields, after some manipulations,

$$\mathbf{J}^N(k_x,k_z,t)=\frac{1}{\nu(\delta^N,\delta^N)_{k_y}}(-\mathbf{u}^N*\nabla\mathbf{u}^N-\nabla p^N+\nu\Delta\mathbf{u}^N,\delta^N)_{k_y}. \tag{8.17}$$

Because of the flow symmetries (8.2), we have $J_y^N = 0$, as expected. We remark, however, that this is not a closed formula for the regularized jumps $\mathbf{J}^N$, but an implicit equation. Indeed, the pressure must be solved from the Poisson equation (8.12) in terms of both the velocities $\mathbf{u}^N$ and the jumps $\mathbf{J}^N$. The resulting equations can be solved explicitly for $\mathbf{J}^N$, but we omit here the laborious computations. In Chapters 9 and 10 we present results for the simpler cases of one and two dimensions, respectively.

Finally, the original jumps $\mathbf{J}$ are recovered from their regularized counterparts by taking the limit

$$\mathbf{J}(k_x, k_z, t) = \lim_{N\to\infty} \mathbf{J}^N(k_x, k_z, t). \tag{8.18}$$

Particularly, $J_y = 0$.

We remark that the computation of the jump in the logarithmic lattice model just presented is analogous to the continuous-space case from Section 7.3: we consider some regular approximation of the Dirac delta distribution, compute the approximated jump and then take the limit in the approximation parameter.

8.3 Basic symmetries and balance laws

The symmetries of the Euler equations with boundary are those enumerated in Theorem 5.1 (for the case without boundary) which preserve the imposed flow symmetries (8.2). To enumerate them, if $\mathbf{u}(\mathbf{k}, t)$ is a solution of system (8.11), then the following transformations also yield solutions:

(E'.1) (Time translations) $\mathbf{u}^\tau(\mathbf{k}, t) = \mathbf{u}(\mathbf{k}, t + \tau)$, for any $\tau \in \mathbb{R}$;

(E'.2) (Space translations in x and z) $\mathbf{u}^{\boldsymbol{\xi}}(\mathbf{k}, t) = e^{-i\mathbf{k}\cdot\boldsymbol{\xi}}\mathbf{u}(\mathbf{k}, t)$, for any $\boldsymbol{\xi} = (\xi_x, 0, \xi_z) \in \mathbb{R}^3$;

(E'.3) (Isotropy in x and z and parity) $\mathbf{u}^R(\mathbf{k}, t) = R^{-1}\mathbf{u}(R\mathbf{k}, t)$, where R is any transformation $(k_1, k_2, k_3) \mapsto (\pm k_\alpha, \pm k_2, \pm k_\beta)$ with (α, β) permutations of $(1, 3)$;

(E'.4) (Scale invariance) $\mathbf{u}^{n,h}(\mathbf{k}, t) = \lambda^h \mathbf{u}\left(\lambda^n \mathbf{k}, \lambda^{h-n} t\right)$, for any $h \in \mathbb{R}$ and $n \in \mathbb{Z}$, where λ is the lattice spacing;

(E'.5) (Time reversibility) $\mathbf{u}^r(\mathbf{k}, t) = -\mathbf{u}(\mathbf{k}, -t)$;

(E'.6) (Galilean invariance in x and z) $\mathbf{u}^{\mathbf{v}}(\mathbf{k}, t) = e^{-i\mathbf{k}\cdot\mathbf{v}t}\mathbf{u}(\mathbf{k}, t) - \widehat{\mathbf{v}}(\mathbf{k})$, for any $\mathbf{v} = (v_x, 0, v_z) \in \mathbb{R}^3$, where $\widehat{\mathbf{v}}(\mathbf{k})$ is the constant velocity field on the lattice defined as $\widehat{\mathbf{v}}(\mathbf{0}) = \mathbf{v}$ and zero for $\mathbf{k} \neq \mathbf{0}$.

Naturally, Galilean invariance *(E'.6)* is well-defined only for the lattices with zero components.

Since the equations are not modified by introducing a boundary, the conserved quantities are the same, say: the energy (5.6) and helicity (5.7) in the three-dimensional case, and the energy (5.6) and enstrophy (5.8) in the two-dimensional case. See Theorem 5.2 for details. Kelvin's Theorem 5.3 for the conservation of circulation also holds in the presence of a boundary.

In the case of positive viscosity, the Navier-Stokes equations with and without boundary share the same scaling symmetry

(NS') (Scale invariance) $\mathbf{u}^n(\mathbf{k},t) = \lambda^{-n}\mathbf{u}\left(\lambda^n\mathbf{k}, \lambda^{-2n}t\right)$, for any $n \in \mathbb{Z}$, where λ is the lattice spacing.

Thus, the introduction of a boundary through our modelling technique does not disrupt the self-similarity properties of the Navier-Stokes equations.

Additionally, the shear force $\mathbf{F}(k_x,k_y,k_z,t) = -\nu\mathbf{J}(k_x,k_z,t)\delta(k_y)$ on the boundary exerts no work in the flow, as a consequence of no-slip boundary condition

$$(\mathbf{F},\mathbf{u}) = -\nu \sum_{k_x,k_z\in\mathbb{\Lambda}} \mathbf{J}(k_x,k_z,t)\cdot(\mathbf{u},\delta)_{k_y} = 0. \tag{8.19}$$

This proportionates the usual energy balance law

$$\frac{dE}{dt} = -2\nu\Omega(t), \tag{8.20}$$

where Ω is the enstrophy (5.8). This balance equation is also satisfied by the regularized flows $\mathbf{u}^N$.

Chapter 9

Classical shear flows

In this chapter, we consider some classical shear flows. Due to their simplicity, we can study the logarithmic lattice solutions in the light of exact expected results, or even compare them with direct numerical simulations. Naturally, the comparisons are always in terms of phenomenology.

We presented the governing system of equations (7.20) for a three-dimensional flow on the upper-half volume $y > 0$ with a solid boundary on the plane $y = 0$. Let us assume such flow has no variation with respect to x and z, and that $v = w = 0$. Under those hypotheses, incompressibility is trivially satisfied, while pressure is constant. Then, the resulting flow simplifies to a one-dimensional velocity field $u = u(y, t)$ governed by

$$\begin{cases} \partial_t u = \nu \partial_y^2 u + f & \text{in } y > 0, \\ u = 0 & \text{on } y = 0, \end{cases} \tag{9.1}$$

where $f = f(y, t)$ is a possible external force. System (9.1) is supplemented by proper initial conditions

$$u\Big|_{t=0} = u^0(y). \tag{9.2}$$

This is the Dirichlet problem for the one-dimensional linear heat equation. Such system can be solved exactly using the heat kernel and reflections—see Appendix F for a closed formula. Here, we understand its solutions as simple shear flows past a solid plate.

We divide this chapter as follows. We deduce the corresponding logarithmic lattice model in Section 9.1, by applying the ideas from the previous chapters. In Section 9.2, some aspects of immersed boundaries in logarithmic lattices are studied for the flow between two parallel plates (Couette flow). Next, in Section 9.3 we compare the

logarithmic lattice results with DNS for a decaying shear flow. Finally, we verify the fast convergence of solutions with respect to truncation in Section 9.4.

9.1 Logarithmic lattice model

Following the steps in the Chapter 7, we can formulate problem (9.1) on the whole domain, considering a discontinuity point at the origin $y = 0$. The resulting jump formulation reads

$$\begin{cases} \partial_t u = \nu \partial_y^2 u + f - \nu J(t)\delta(y) & \text{in } \mathbb{R}, \\ u(y) = u(-y) & \text{in } \mathbb{R}, \\ u = 0 & \text{on } y = 0. \end{cases} \tag{9.3}$$

The jump discontinuity is derived from system (9.3) as

$$J(t) = [\partial_y u]. \tag{9.4}$$

On a logarithmic lattice

$$\mathbb{\Lambda} = \{0, \pm 1, \pm\lambda, \pm\lambda^2, \dots\}, \tag{9.5}$$

model (9.3) reads

$$\begin{cases} \partial_t u = \nu \partial_y^2 u + f - \nu J(t)\delta(k) & \text{in } \mathbb{\Lambda}, \\ u(k) = u(-k) & \text{in } \mathbb{\Lambda}, \\ (u, \delta) = 0 & \text{for all } t \in \mathbb{R}. \end{cases} \tag{9.6}$$

As we saw earlier, the jump $J(t)$ can be computed explicitly. If the lattice (9.5) is truncated up to the wave number $k_N = \lambda^{N-1}$ as

$$\mathbb{\Lambda}_N = \{0, \pm 1, \pm\lambda, \pm\lambda^2, \dots \lambda^{N-1}\}, \tag{9.7}$$

we have the approximated model

$$\begin{cases} \partial_t u^N = \nu \partial_y^2 u^N + f^N - \nu J^N(t)\delta^N(k) & \text{in } \mathbb{\Lambda}_N, \\ u^N(k) = u^N(-k) & \text{in } \mathbb{\Lambda}_N, \\ (u^N, \delta^N) = 0 & \text{for all } t \in \mathbb{R}. \end{cases} \tag{9.8}$$

Taking the inner product of the main equation in (9.8) against δ^N, and using the no-slip condition $(u^N, \delta^N) = 0$, we obtain

$$(\nu\partial_y^2 u^N + f^N, \delta^N) + (-\nu J^N(t)\delta^N, \delta^N) = 0. \tag{9.9}$$

Next, using the fact that $J^N(t)$ does not depend on k, we can evaluate the term

$$(-\nu J^N(t)\delta^N, \delta^N) = -\nu J^N(t)(\delta^N, \delta^N). \tag{9.10}$$

Observe that, since the lattice is now truncated, the expression (δ^N, δ^N) is a well-defined positive number, which can be explicitly computed as

$$(\delta^N, \delta^N) = \sum_{k \in \mathbb{\Lambda}^N} 1 = 2N + 1. \tag{9.11}$$

Finally, we substitute (9.10) into (9.9) and isolate $J^N(t)$ to obtain a closed formula for the approximated jump

$$J^N(t) = \frac{(\partial_y^2 u^N + f^N, \delta^N)}{(\delta^N, \delta^N)}. \tag{9.12}$$

The original jump is then recovered from the sequence of its approximations

$$J(t) = \lim_{N\to\infty} J^N(t) = \lim_{N\to\infty} \frac{(\partial_y^2 u^N + f^N, \delta^N)}{(\delta^N, \delta^N)}. \tag{9.13}$$

9.2 Couette flow

Let us consider a flow between two parallel plates separated by a unit distance. One of the plates is at rest, and the other moves with a constant horizontal speed V. This classical problem has well-known stationary solution—consult *e.g.* [98, §17]—given by the linear velocity profile

$$u(y) = Vy \quad \text{for } 0 \le y \le 1. \tag{9.14}$$

Then, the shear force f_1 exerted on the fluid by the moving plate at $y = 1$ is

$$f_1 = \nu V \quad \text{at } y = 1, \tag{9.15}$$

while the force f_0 from the plate $y = 0$ at rest is the symmetric counterpart

$$f_0 = -\nu V \quad \text{at } y = 0, \tag{9.16}$$

To model a similar phenomenon on a logarithmic lattice, we take our usual framework (9.6) and consider the action of the moving plate as a constant-in-time force f applied at $k = 0$ in the form

$$f(k,t) = 2\nu V \delta_0(k), \tag{9.17}$$

with

$$\delta_0(k) = \begin{cases} 1, & \text{if } k = 0, \\ 0, & \text{otherwise.} \end{cases} \tag{9.18}$$

We concentrate the force at $k = 0$ in order to model the momentum input due to the moving boundary. The choice of the force (9.17) is motivated by the known shear action (9.15) at the moving plate from the original problem. Such force is proportional to the relative velocitity between the plates and to the fluid viscosity. The factor 2 appears in (9.17) because our reflected flow doubles the forces on the discontinuity surface.

Stationary solution

Let us look for stationary solutions of system (9.6) under the action of the force (9.17). Evaluating the governing equation at $k = 0$ gives us the value of the jump

$$J = 2V. \tag{9.19}$$

The solution at $k \neq 0$ can now be obtained, using that $f(k) = 0$ at $k \neq 0$, as

$$0 = \nu \partial_y^2 u(k) - J\delta(k) = -\nu k^2 u(k) - \nu J, \tag{9.20}$$

which yields

$$u(k) = -2Vk^{-2} \quad \text{for } k \neq 0. \tag{9.21}$$

Finally, the mean flow $u(k = 0)$ can be computed from the no-slip boundary condition, as follows

$$0 = (u, \delta) = \sum_{k \in \mathbb{\Lambda}} u(k) = u(0) + \sum_{k \in \mathbb{\Lambda} \setminus \{0\}} u(k) = u(0) - 2V \sum_{k \in \mathbb{\Lambda} \setminus \{0\}} k^{-2}, \tag{9.22}$$

whence

$$u(0) = 2V \sum_{k \in \mathbb{\Lambda} \setminus \{0\}} k^{-2}. \tag{9.23}$$

The final solution

$$J = 2V \quad \text{and} \quad u(k) = \begin{cases} 2V \sum_{\tilde{k} \in \mathbb{N} \setminus \{0\}} \tilde{k}^{-2} & \text{for } k = 0, \\ -2V k^{-2} & \text{for } k \neq 0, \end{cases} \tag{9.24}$$

shares many similitudes with the real shear flow. First, the jump agrees exactly with the original velocity profile (9.14), if we consider its symmetric reflection $u(-y) = u(y)$ around the origin $y = 0$. Consequently, the shear force at the plate is $-\nu J = -2\nu V$, which is in agreement with the force (9.16). Remember that the reflections of the flow around the origin double the forces, which explains the extra factor 2. Second, we observe a solution tail proportional to k^{-2}, which is the expected Fourier spectrum for a function whose first derivative is discontinuous.

Unsteady solutions

We can also simulate unsteady solutions of system (9.6) under the action of the force (9.17). For this, we set $V = 1$, $\nu = 1$ and consider identically zero initial conditions $u^0 \equiv 0$. We take the truncated logarithmic lattice (9.7) with $\lambda = 2$ and $N = 50$. Together, they provide the finest scale $\ell_N = 1/k_N \approx 10^{-15}$. We integrate the equations using MATLAB's ode15s solver [141], with the tolerances $RelTol = 10^{-8}$ and $AbsTol = 10^{-11}$.

Fig. 9.1 shows the time evolution of our Couette-like flow. As time advances, the solution converges to the stationary state (9.24), which is a fixed point attractor of the system. At each instant, the solution presents two different regimes along scales: a constant plateau $|u| \approx const.$ state at larger scales, followed by a $|u| \propto k^{-2}$ tail at smaller scales. Such behavior is more noticeable in earlier instants, since the plateau $|u| \approx const.$ collapses as time advances. These two regimes can be understood by establishing the corresponding asymptotic solutions, as we do now. For this analysis, we consider both infinitely large and small k.

The asymptotic solutions are obtained by analysing how the terms in the governing equation scale with respect to k. First, we notice that the boundary force $-\nu J(t)\delta(k)$ acts with the same magnitude at all scales, since $\delta \equiv 1$. Therefore, it contributes both to large and to small scales. Next, we analyze the contribution of the dissipative term $\nu \partial_y^2 u(k,t) = -\nu k^2 u(k,t)$, which determines the two different regimes. At high k, the dissipative term becomes important and dominates over the time derivative $\partial_t u$. In

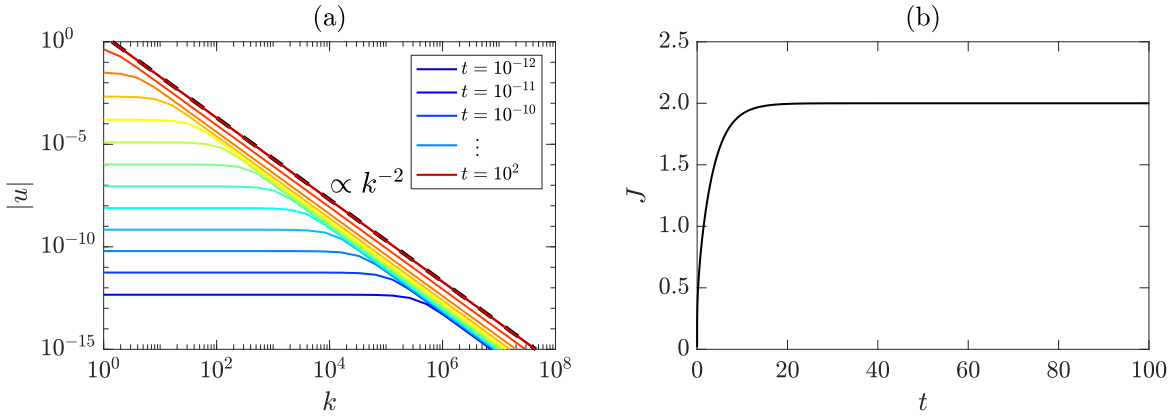

Fig. 9.1 Dynamical evolution of the shear flow on a logarithmic lattice. (a) Spectra of solution $|u(k)|$ as a function of the wave number k at several instants. Time advances from blue to red in logarithmic scale, from $t = 10^{-12}$ up to $t = 10^2$ by factors of 10. The solution converges to the stationary power-law k^{-2}, represented by the black dashed line. (b) Time evolution of the jump variable $J(t)$, converging to the constant steady value $J = 2V$ as time advances.

this regime, we have the balance

$$\nu \partial_y^2 u \sim \nu J \delta, \tag{9.25}$$

which results in the tail asymptotic solution

$$u(k,t) \sim -J(t) k^{-2} \quad \text{as } k \to \infty. \tag{9.26}$$

On the other hand, if k is small, the dissipative term becomes negligible, and it is dominated by the time derivative $\partial_t u$. The balance now is

$$\partial_t u \sim -\nu J \delta \quad \text{as } k \to 0. \tag{9.27}$$

Eq. (9.27) is independent from k, which justifies the constant plateau behavior

$$u(k,t) \approx v(t) \quad \text{for small } k, \tag{9.28}$$

in Fig. 9.1(a). To confirm such statement, let us consider the ordinary differential equation

$$\frac{dv}{dt} = -\nu J(t), \tag{9.29}$$

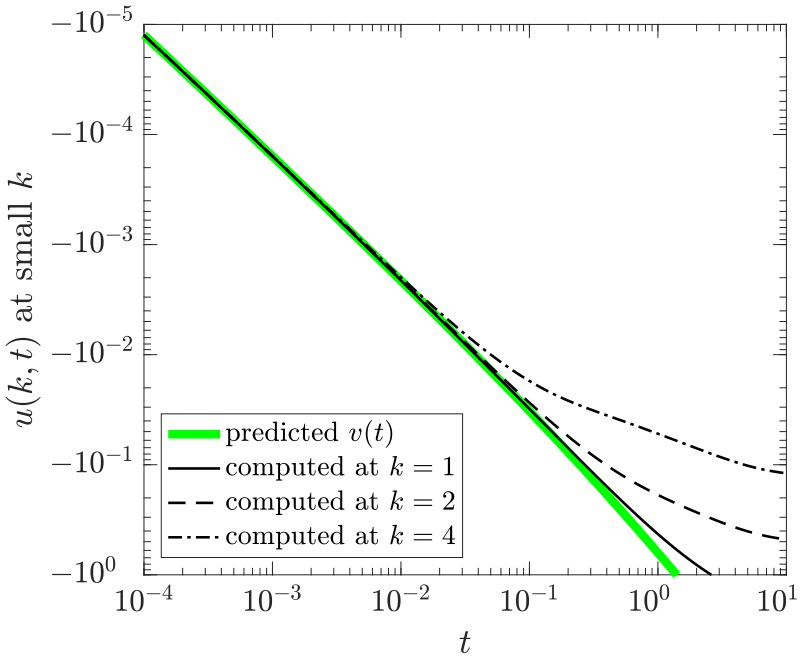

Fig. 9.2 Time evolution of $u(k,t)$ at small $k \in \mathbb{\Lambda}$ on the logarithmic lattice. Axes are in logarithmic scales. We plot in green the predicted asymptotic value $v(t)$. Black curves show actual computed solutions $u(k,t)$. Different styles of lines stand for different scales k.

where Eq. (9.29) is the exact form for asymptotic balance of (9.27) and (9.28). We integrate this equation numerically using the numerical result of $J(t)$ from our model. Fig. 9.2 compares this predicted value for the plateau with the actual solution $u(k,t)$ for small k. We verify that as k decreases, the agreement between the prediction and the solution improves.

In the above analysis of the logarithmic lattice model, we considered the two regimes by looking at the dissipative term $\partial_y^2 u(k,t) = -k^2 u(k,t)$ for infinitely large or small k. For finite k, we observe the transition between one to the other regime when $|u(k,t)|$ increases up to the order of k^2, which eventually occurs at any finite scale k after sufficiently large time. We can see the transition of regimes in Fig. 9.1(a) and the expected deviation from the asymptotic solution at finite k after some time in Fig. 9.2.

9.3 Decaying shear flow

Next we consider a decaying shear flow. The set up consists of system (9.1) with zero external force $f \equiv 0$ and nontrivial initial condition u^0.

First, we shall solve the continuous-space formulation (9.3) with a direct numerical simulation. For this, we employ simple finite difference schemes with a regularized Dirac delta parametrized by the number of grid points. Such strategy will illustrate the explicit computation of jump singularities proposed in the Section 7.3. Then, we shall consider a logarithmic lattice version of Eq. (9.3). The results for this model will be compared with the precedent direct numerical simulations.

9.3.1 Direct numerical simulations in continuous space

Consider the discontinuous formulation (9.3) in the original physical space $y \in \mathbb{R}$, with $f \equiv 0$. For the numerical model, we shall restrict ourselves to a bounded spatial domain $y \in [-L, L]$ and simulate the dynamics on a finite interval of time $t \in [0, T]$. Such framework is a good approximation of the unbounded system $y \in \mathbb{R}$ when the initial condition has fast decrease at infinity and T is sufficiently small.

We discretize the spatial domain into N points in each direction around the origin

$$y_n = n\Delta y, \quad n = -N, -N+1 \ldots, N-1, N, \tag{9.30}$$

where the grid spacing Δy relates to the number of points and the size of domain as

$$\Delta y = \frac{2L}{N}. \tag{9.31}$$

Similarly, we consider $M + 1$ points in time

$$t_m = m\Delta t, \quad m = 0, \ldots, M, \tag{9.32}$$

with the time step defined as

$$\Delta t = \frac{T}{M}. \tag{9.33}$$

The functions u and J evaluated at the point y_n at instant t_m are denoted by

$$u_n^m = u(y_n, t_m), \quad J^m = J(t_m). \tag{9.34}$$

We approximate the second-order spatial derivative by a centered finite difference

$$\partial_y^2 u\Big|_{(y_n, t_m)} \approx \frac{u_{n+1}^m - 2u_n^m + u_{n-1}^m}{\Delta y^2}, \tag{9.35}$$

and the time derivative by an forward first-order finite difference

$$\partial_t u\Big|_{(y_n,t_m)} \approx \frac{u_n^{m+1} - u_n^m}{\Delta t}. \tag{9.36}$$

Finally, we approximate the Dirac delta as

$$\delta\Big|_{(y_n,t_m)} \approx \frac{1}{\Delta y}\delta_n, \quad \text{with } \delta_n = \begin{cases} 1, & n = 0, \\ 0, & n \neq 0. \end{cases} \tag{9.37}$$

Inserting all the above approximations into Eq. (9.3) at (y_n, t_m) yields

$$\frac{u_n^{m+1} - u_n^m}{\Delta t} = \nu \frac{u_{n+1}^m - 2u_n^m + u_{n-1}^m}{\Delta y^2} - \nu J^m \frac{1}{\Delta y}\delta_n, \tag{9.38}$$

which, after some manipulations, leads us to a recurrence relation

$$u_n^{m+1} = (1 - 2\alpha)u_n^m + \alpha(u_{n+1}^m + u_{n-1}^m) - \alpha \Delta y J^m \delta_n. \tag{9.39}$$

Here we have introduced the parameter

$$\alpha = \frac{\nu \Delta t}{\Delta y^2}. \tag{9.40}$$

Stability condition [101, §9.3] for this model is

$$\Delta t \leq \frac{\Delta y^2}{2\nu}. \tag{9.41}$$

Computation of the jump discontinuity

The boundary condition for the regularized system is

$$(u, \delta) = \sum_{n=-N}^{N} u_n^m \frac{1}{\Delta y}\delta_n = \frac{1}{\Delta y} u_0^m = 0 \quad \text{for } m = 0, \ldots, M, \tag{9.42}$$

that is

$$u_0^m = 0 \quad \text{for } m = 0, \ldots, M. \tag{9.43}$$

We use this to compute the values J^m as follows. Take the numerical equation (9.39) at $n = 0$ to obtain

$$\alpha(u_1^m + u_{-1}^m) - \alpha \Delta y J^m = 0. \tag{9.44}$$

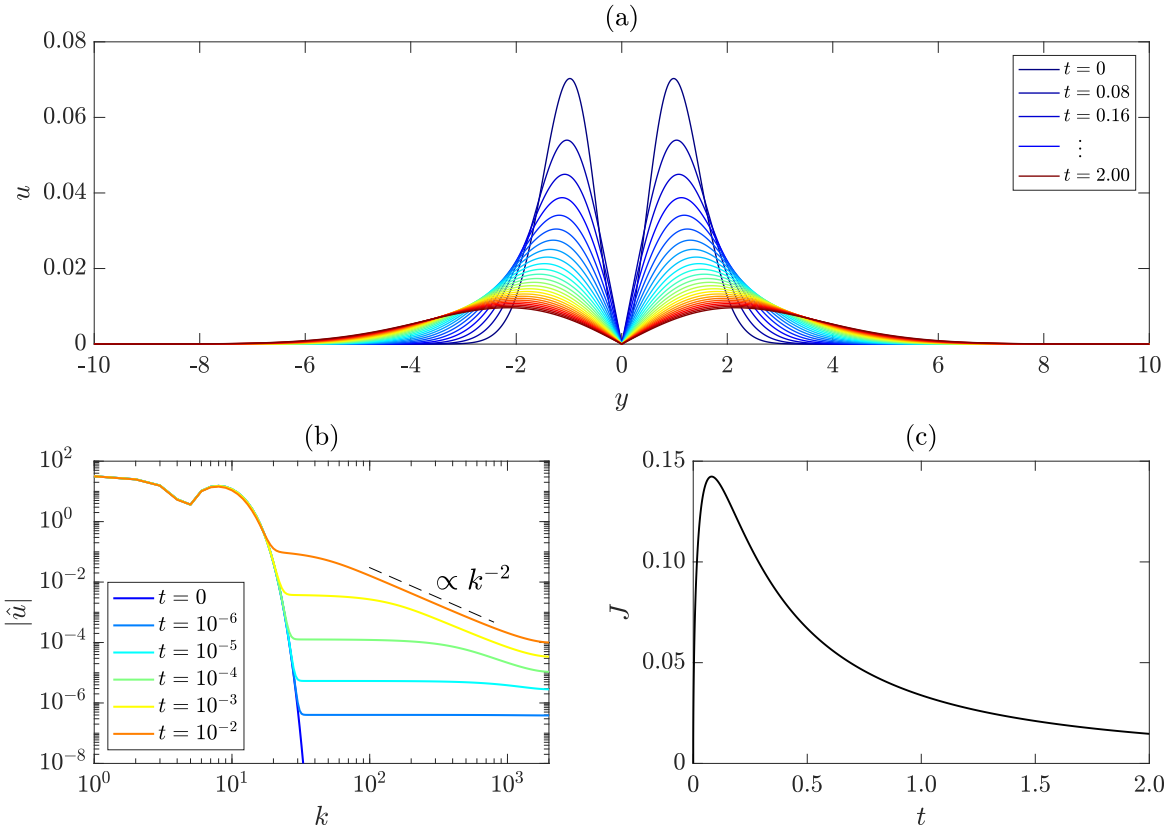

Fig. 9.3 Direct numerical simulations of the discontinuous formulation of one-dimensional shear flow. (a) Solution u along space y. Different colors indicate solutions at different instants t. Time advances from blue to red. (b) Fourier spectra of solution in logarithmic scales. Time advances from from blue to red in logarithmic scale. (c) Time evolution of the jump $J(t)$.

We isolate J^m as

$$J^m = \frac{u_1^m + u_{-1}^m}{\Delta y}, \tag{9.45}$$

i.e., J^m is the numerical approximation of the jump of $\partial_y u$ at $y = 0$. Recall that, since $u_0^m = 0$ for all m, we can write

$$J^m = \frac{u_1^m - u_0^m}{\Delta y} - \frac{u_0^m - u_{-1}^m}{\Delta y} \approx \partial_y u(0^+) - \partial_y u(0^-) = [\partial_y u]. \tag{9.46}$$

Substitution of Eq. (9.45) into Eq. (9.44) gives us the final numerical model

$$u_n^{m+1} = (1 - 2\alpha)u_n^m + \alpha(u_{n+1}^m + u_{n-1}^m)(1 - \delta_n), \tag{9.47}$$

with the jump discontinuity post-processed from the solution by formula (9.45).

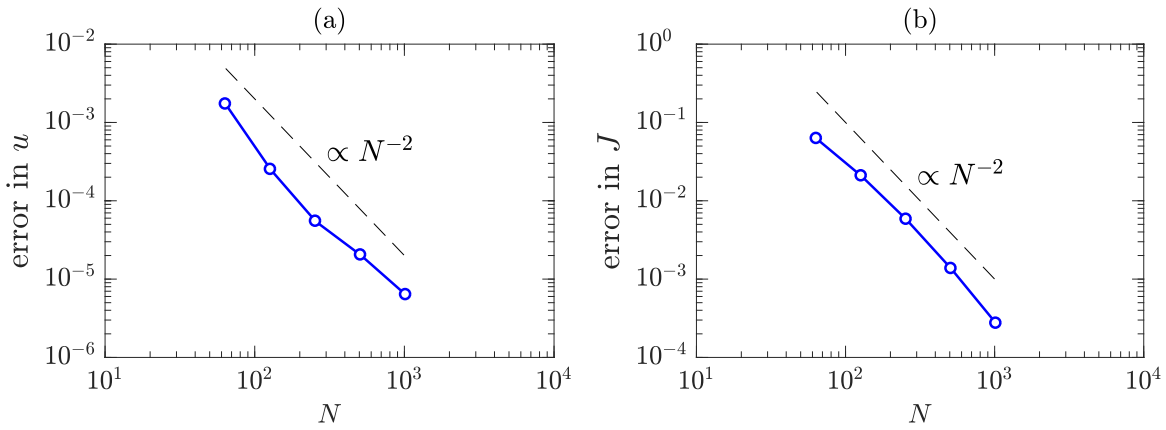

Fig. 9.4 Numerical error of direct numerical simulations for different grid points N in the continuous space model. (a) Error of solution u. (b) Error of jump J.

Numerical experiments

We set $\nu = 1$, and the initial condition to

$$u^0(y) = \left[1 - \cos\left(\frac{\pi y}{5}\right)\right] e^{-y^2/2}. \tag{9.48}$$

This function satisfies the odd symmetry $u(-y) = u(y)$ and decays exponentially fast at infinity $|y| \to \infty$. Moreover, the initial condition satisfies the no-slip condition $u^0(0) = 0$ and has zero initial shear force as $[\partial_y u^0] = 0$.

We fix $L = 10$. Our first numerical integrations concern the general picture of the solution in physical space after some amount of time. We use $T = 2$, $N = 1024$ and $M = 20000$. The results are depicted in Figs. 9.3(a) and 9.3(c). To reach better resolution in Fourier space at earlier instants, we change the numerical parameters to $T = 0.01$ and $N = 4096$, while M is kept the same. The Fourier spectrum is drawn in Fig. 9.3(b). We now discuss the results.

We show the time evolution of the velocity along physical space in Fig. 9.3(a). The initial data (9.48) is essentially two symmetric bumps close to the origin quickly decaying at infinity. They represent an initial motion restricted to large scales—as we verify from the spectrum concentrated on small k in Fig. 9.3(b). As time advances, the solution dissipates and tends towards the identically zero steady state. Initially, the velocity profile develops a large increase in the jump, it achieves a maximum and then decays, as in Fig. 9.3(c).

In Fourier space, we see some features that we already presented for the logarithmic model of a Couette-like flow. The initial state is confined to large scales, but the

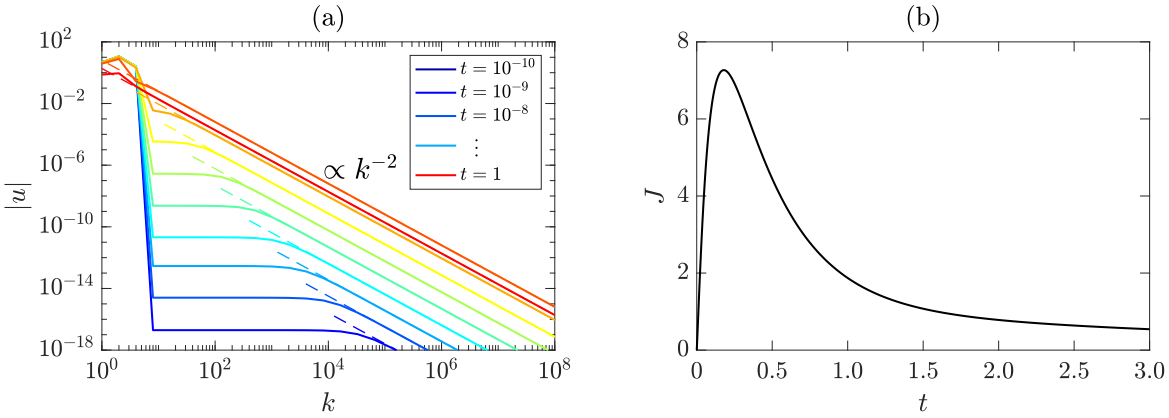

Fig. 9.5 Dynamical evolution a decaying shear flow on a logarithmic lattice. (a) Spectra of solution $|u(k)|$ as a function of the wave number k at several instants. Time advances from blue to red in logarithmic scale, from $t = 10^{-10}$ up to $t = 10^{0}$ by factors of 10. The dashed lines show the corresponding asymptotic solutions $u(k,t) \sim -J(t)k^{-2}$ for large k. (b) Time evolution of the jump variable $J(t)$.

boundary shear force affects all scales at every instant of time $t > 0$. This is noticed by the instantaneous development of a constant plateau regime along intermediate scales. Such plateau would be followed by a k^{-2} tail at large scales even for very small t, if we simulated for larger k. Under limited resolution, we can see the power-law development at later times in Fig. 9.3(b), when the tail already reaches intermediate and large scales. We observe some slight deviation from the k^{-2} at the higher scales, as an effect of truncation. Increasing resolution extends the power-law and sends this truncation effect towards higher k.

To check convergence of solutions, and thus robustness of our above conclusions, we employ different number of grid points and compute the error, in ℓ^2 norm for both u and J. The error is computed with respect to the finest grid. The number of time steps is adapted as $M \propto N^2$ to guarantee stability. As expected, the errors go to zero quadratically as (error) $\propto N^{-2}$.

9.3.2 Logarithmic lattice simulations

Now, let us consider the decaying shear flow on a logarithmic lattice. We take the governing system of equations (9.6) with unit viscosity $\nu = 1$ and zero external force $f \equiv 0$. Representing the initial condition $u(k,0)$ by the vector $u^0 = (u^0(0), u^0(\pm 1), u^0(\pm\lambda), u^0(\pm\lambda^2), \dots)$, we fix

$$u^0 = \left(8, \frac{14}{3}, -\frac{67}{6}, \frac{5}{2}, 0, 0, \dots\right). \tag{9.49}$$

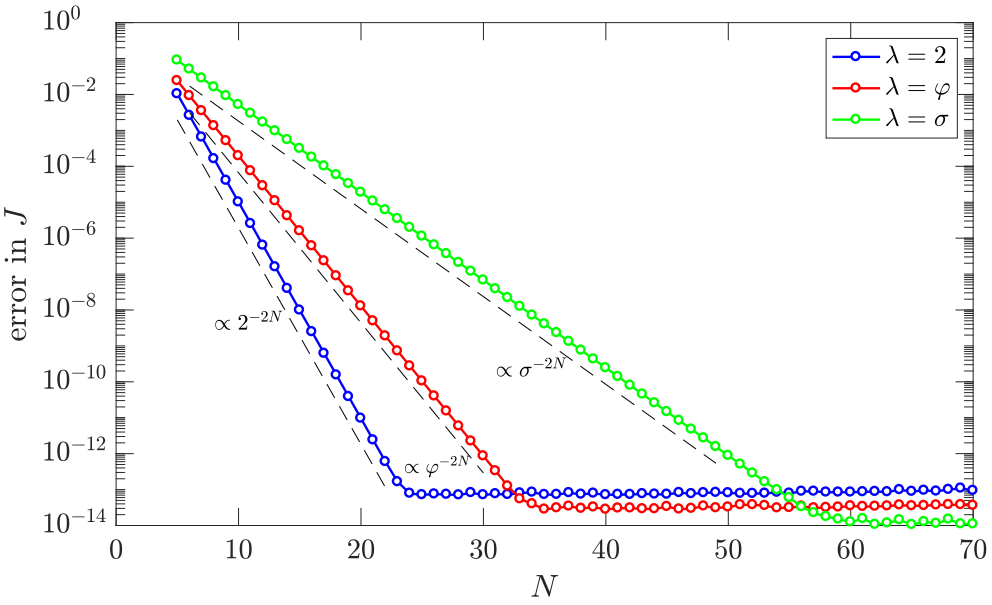

Fig. 9.6 Convergence of solutions with respect to truncation. Error in ℓ^2 norm in time for the jump J^N with respect to a reference solution with 75 as a function of the number of nodes N. Different curves stand for the three lattice spacings: $\lambda = 2$ in blue, $\lambda = \varphi$ (the golden mean) in red, and $\lambda = \sigma$ (the plastic number) in green. Dashed lines give reference to exponential convergence $\propto \lambda^{-2N}$.

Such initial flow satisfies the no-slip condition $(u^0, \delta) = 0$ and has no initial shear flow at the boundary, since $(\partial_y^2 u^0, \delta) = 0$, and thus $J|_{t=0} = 0$.

The numerical simulations are undertaken on the truncated lattice (9.7) with $\lambda = 2$ and $N = 50$. We solve the equations with MATLAB's ode15s solver [141], with tolerances $RelTol = 10^{-8}$ and $AbsTol = 10^{-11}$.

In Fig. 9.5 we see the dynamics of the solution on the logarithmic lattice. Fig. 9.5(a) shows the spectra of the velocites for different instants of time. The initial spectrum is confined to large scales, but the flow instantly develops a k^{-2} tail at high k. The gap between large and small scales is filled by a constant plateau state, which shrinks as time advances. In dashed lines, we plot the asymptotic solutions (9.26) and verify that they match the computed results at high k.

Here we verify that the solution on the logarithmic lattice is quite similar to that obtained from DNS, with the advantage that in the former we can reach way finer scales. The observations of a k^{-2} tail, a plateau in intermediate scales and the dynamical shrink of the gap between them is also present in Fig. 9.3(b) for the continuous space model, but in a more restricted resolution. Moreover, the time evolution of the jump lattice

variable shown in Fig. 9.5(b) is qualitatively indistinguishable from the corresponding jump on the continuous model from DNS in Fig. 9.3(c).

9.4 Convergence with respect to truncation

Heuristically, truncation of the logarithmic lattice $\mathbb{\Lambda}_N$ at a sufficiently large wave number $k_N = \lambda^{N-1}$ represents a cutoff of the k^{-2} tail whose sum is proportional to k_N^{-2}. In node variables, this establishes the exponential convergence rate λ^{-2N}.

To verify such convergence rate with respect to truncation, we perform simulations of the decaying shear flow from Section 9.3.2 for several number of nodes. We range N from 5 up to 70 by unit increments. To compute errors, we consider the simulation $N = 75$ as reference. We integrate equations using MATLAB's ode15s solver with tolerances $RelTol = 10^{-13}$ and $AbsTol = 10^{-16}$. We fix the time window $T = 3$ and sample the solution at points $t_j = j\Delta t$, for $j = 0, 1, \ldots, M$ with $M = 3000$, so $\Delta t = T/M = 0.001$. For each N, we compute the ℓ^2 norm in time of the difference between the jump J^N with respect to the jump of the reference solution with 75 nodes.

Fig. 9.6 shows the results of this set of runs. We readily attest the exponential rate of convergence $(error)^N \propto \lambda^{-2N}$ for the main lattice spacings $\lambda = 2$, φ (the golden mean) and σ (the plastic number). Since the convergence depends on the lattice spacing, errors reach minimum value at a different number of node points, which is approximately $N = 24$ for $\lambda = 2$, $N = 35$ for $\lambda = \varphi$ and $N = 60$ for $\lambda = \sigma$.

Chapter 10

Two-dimensional boundary layers

In this chapter, we study the convergence of Navier-Stokes solutions to Euler's at infinite Reynolds limit in the presence of solid boundaries. Just like in reported DNS [122, 121], we study this problem in two-dimensions. In the light of Kato Equivalence Theorem [89], we track total dissipation of Navier-Stokes flows with increasing Reynolds number. Here, however, we do not give a rigorous final answer to this problem on logarithmic lattices. Many questions remain open and further work is needed. The main goal of this chapter is to present promising results for this long standing problem. Particularly, we show that logarithmic models can reach extremely larger Reynolds numbers than in DNS.

10.1 Model description

We consider two-dimensional flow in the presence of a flat boundary at $y = 0$. Using the two-dimensional logarithmic lattice $\mathbf{k} = (k_x, k_y) \in \mathbb{\Lambda}^2$, the velocity field $\mathbf{u}(\mathbf{k}, t) = (u, v)$ and the scalar pressure $p(\mathbf{k}, t)$ are governed by the incompressible Navier-Stokes equations for a flat solid boundary (8.10) deduced in Chpater 8, and can be explicitly written in the form

$$\begin{cases} \partial_t u + u * \partial_x u + v * \partial_y u = -\partial_x p + \nu \Delta u - \nu J(k_x, t)\delta(k_y) & \text{in } \mathbb{\Lambda}^2 \\ \partial_t v + u * \partial_x v + v * \partial_y v = -\partial_y p + \nu \Delta v & \text{in } \mathbb{\Lambda}^2 \\ \partial_x u + \partial_y v = 0 & \text{in } \mathbb{\Lambda}^2 \\ u(-k_y) = u(k_y), \quad v(-k_y) = -v(k_y), \quad p(-k_y) = p(k_y) & \text{in } \mathbb{\Lambda}^2 \\ (u, \delta)_{k_y} = 0 & \text{for all } k_x \in \mathbb{\Lambda}. \end{cases} \tag{10.1}$$

In two dimensions, the boundary shear force acts only in the x direction. Therefore we represent the jump variable J as a scalar.

As usual, the pressure can be eliminated from the equation due to incompressibility, by solving the Poisson equation (8.12). In the case of positive viscosity, the pressure will be solved in terms of velocities and the jump J.

Computation of the jump

In the numerical integrations, we consider system (10.1) on the truncated logarithmic lattice $\mathbb{\Lambda}_N^2$, given by

$$\mathbb{\Lambda}_N = \{\pm 1, \pm\lambda, \pm\lambda^2, \cdots \pm \lambda^{N-1}\}. \tag{10.2}$$

As we did in the previous chapters, we add superscript N to the variables (say, u^N, v^N, p^N and so on) to indicate the solutions of the truncated system.

To compute the jump J^N, we take the k_y-inner product of the u^N equation against δ^N and use the no-slip condition $(u^N, \delta^N)_{k_y} = 0$ to eliminate the time derivative contribution $(\partial_t u^N, \delta)_{k_y} = 0$. After solving for the pressure p^N, the approximated jump J^N can be isolated and it has the following explicit formula

$$J^N(k_x,t) = \frac{1}{\nu(\xi\delta^N,\delta^N)_{k_y}}(\partial_x\Delta^{-1}\nabla\cdot(\mathbf{u}^N * \nabla\mathbf{u}^N) - u^N * \partial_x u^N - v^N * \partial_y u^N + \nu\partial_y^2 u^N, \delta^N)_{k_y}, \tag{10.3}$$

where Δ^{-1} and ξ are the Fourier multipliers

$$\Delta^{-1}(k_x,k_y) = \frac{1}{k_x^2+k_y^2}, \quad \xi(k_x,k_y) = \frac{k_y^2}{k_x^2+k_y^2}. \tag{10.4}$$

The jump J is recovered from the approximated jumps J^N throught the limit

$$J(k_x,t) = \lim_{N\to\infty} J^N(k_x,t). \tag{10.5}$$

Convergence of jump variable

Let us analyse expression (10.3) for the approximated jump J^N. We can write it in terms of two contributions

$$J^N = NL^N + Diss^N, \tag{10.6}$$

where NL^N represents the contribution of nonlinear terms

$$NL^N = \frac{1}{\nu(\xi\delta^N,\delta^N)_{k_y}}(\partial_x\Delta^{-1}\nabla\cdot(\mathbf{u}^N * \nabla\mathbf{u}^N) - u^N * \partial_x u^N - v^N * \partial_y u^N, \delta^N)_{k_y} \tag{10.7}$$

Run	**I**	**II**	**III**	**IV**	**V**	**VI**	**VII**	**VIII**	**IX**	**X**
Re	10^1	10^2	10^3	10^4	10^5	10^6	10^7	10^8	10^9	10^{10}
N	60	68	75	83	90	98	105	113	120	128

Table 10.1 Reynolds number Re and number of nodes N for each run.

and $Diss^N$, the contribution of the dissipative term

$$Diss^N = \frac{1}{(\xi\delta^N, \delta^N)_{k_y}} (\partial_y^2 u^N, \delta^N)_{k_y}. \tag{10.8}$$

If the velocities remain in the same regularity class (with the expected k^{-2} tail in the spectrum), the numerator of NL^N is going to converge to a finite value in the limit $N \to \infty$. The denominator, however, grows with respect to N, for a fixed viscosity. Therefore, we must have

$$\lim_{N\to\infty} NL^N = 0, \tag{10.9}$$

and only $Diss^N$ effectively contributes to the jump in the limit $N \to \infty$. The term NL^N cannot be dropped, however, otherwise the no-slip boundary condition is not satisfied.

A more subtle convergence problem arises in the study of vanishing viscosity. A small viscosity parameter appearing in the denominator of NL^N may amplify the spurious contribution of the nonlinearities to the computation of jumps. To guarantee convergence, we must first take the truncation limit $N \to \infty$, and later the vanishing viscosity limit $\nu \to 0$. Still, for proper numerical simulations, we must have the compensation of the two terms ν and $(\xi\delta^N, \delta^N)$, in such a way that their product is big enough to provide a small NL^N. In order to guarantee an adequate convergence rate to $NL^N \to 0$, we employ the generalized inner product (4.1) and generalized convolution product (4.2) with parameters $\alpha > 0$ and $\beta = 0$. One may estimate the lower bound

$$(\xi\delta^N, \delta^N) \geq \lambda^{\alpha(N-1)} \quad \text{for all } k_x \in \mathbb{\Lambda}_N. \tag{10.10}$$

Since $(\xi\delta^N, \delta^N)$ grows exponentially fast, the decrease in one order of magnitude in ν is roughly compensated by a linear increase in N. In analogy to the Boundary Layer Theory [140], we expect the jumps J to increase as the viscosity vanishes. For this reason, in practice we do not try to keep NL^N small in absolute value, but in relative error with respect to the total jump, *i.e.*, we keep NL^N/J^N small.

10.2 Numerical setup

We chose the logarithmic lattice with golden mean spacing $\lambda = \varphi$. Model (10.1) is integrated with double precision by MATLAB's ode15s solver [141]. We set the tolerances $RelTol = 10^{-10}$ and $AbsTol = 10^{-13}$. For the operations on logarithmic lattices, we employ LOGLATT [27, 28]—consult Appendix B for details of implementation.

The initial condition is fixed for all simulations and taken as random components in a box of three by three nodes, *i.e.* at scales (k_x, k_y) with $1 \leq k_x, k_y \leq \varphi^2$. The components are adjusted to match no-slip condition and zero initial jump. The initial state is zero elsewhere.

We simulate Reynolds numbers Re from 10^1 up to 10^{10}. Parameter α and the number of nodes N in each direction of the lattice are chosen so the relative error $\varepsilon^N = NL^N/J^N$ is kept small. We set $\alpha = 0.2$. The values of Re and N for each run are in Tab. 10.1. The error ε^N oscillates along scales due to nonlinearities, but they decrease in average from 10^{-2} to 10^{-4} as Re increases. To ensure that the qualitative behavior do not change because of the error on the jump computation, we performed simulations with twenty more and twenty less nodes. All simulations presented the same qualitative behavior, with also good quantitative agreement before the transition to chaos. Moreover, the error in ℓ^∞ norm for the incompressibility was kept below 8×10^{-15} for all simulations at all instants, and the error in $\ell^\infty_t \ell^1_{k_x}$ for the slip at the boundary was kept below 1.2×10^{-9}.

We now turn to the detailed presentation of the results.

10.3 Laminar to turbulent transition

Direct numerical simulations of dipole-wall collision [122, 121] indicate that possible singularities in the boundary are expected to develop from sharp gradients in the direction tangential to the wall, leading to a boundary-layer detachment. Observe, for instance, the abrupt change of vorticity signs along the boundary in Fig. 1.4(c). For this reason, we start the analysis of results by considering the simple solution spectrum

$$\mathcal{S}(k) = \sum_{k \leq |\mathbf{k}'| < \lambda k} |\mathbf{u}(\mathbf{k}')| \tag{10.11}$$

and the following spectrum in the x direction

$$\mathcal{S}_x(k_x) = \sum_{k_y \in \mathbb{\Lambda}} |\mathbf{u}(k_x, k_y)|. \tag{10.12}$$

Fig. 10.1 plots the two above spectra for Run VI, whose $Re = 10^6$. The behavior of early and late times are distinct. The initial instants in Fig. 10.1(a) depict an organized and ordered state, followed at late times by a disorganized and chaotic state in Fig. 10.1(b). For this reason, we call the first regime *laminar* and the second *turbulent*. We describe their features in details now.

The solutions are initialized at large scales only, but they instantly develop a k^{-2} tail (which actually occurs in k_y direction only, but dominates the whole spectrum) and a constant plateau k^0 at intermediate scales k. The explanation here of such scalings is similar to what we elaborated for one-dimensional shear flows—see the asymptotic solutions constructed in Section 9.2. For large k_y, we have the asymptotic balance

$$\nu \partial_y^2 u \sim \nu J \delta, \tag{10.13}$$

which gives us the k_y^{-2} tail

$$u(k_x, k_y, t) \sim -J(k_x, t) k_y^{-2} \quad \text{for large } k_y. \tag{10.14}$$

In intermediate scales and initial instants, we expect

$$\partial_t u \sim -\nu J \delta \quad \text{for small } k_y, \tag{10.15}$$

whose solution provides the plateau. All these phenomena concern the boundary effect in y direction. On the other hand, the spectrum in x direction remains confined to large scales, slowly propagating to intermediate values of k_x.

As time advances, the plateau level increases monotonically until it reaches a certain saturated value. Then, other terms of the governing equation (like the nonlinear term) start to influence the solution. In Fig. 10.1(b) we track the abrupt transition from the laminar to turbulent states. The smooth and clear slopes evolve to sinuous and strong oscillations around a possible average power-law. The k^{-2} tail is still present due to the boundary effects in y direction. The plateau, however, changes from k^0 to a $k^{-0.27}$ decay. The x-spectrum $\mathcal{S}_x(k_x)$ quickly propagates towards high k_x with the development of the power-law $S_x \propto k_x^{-0.55}$. Here, the exponents are rough approximations, and they are plot in the figure just for reference.

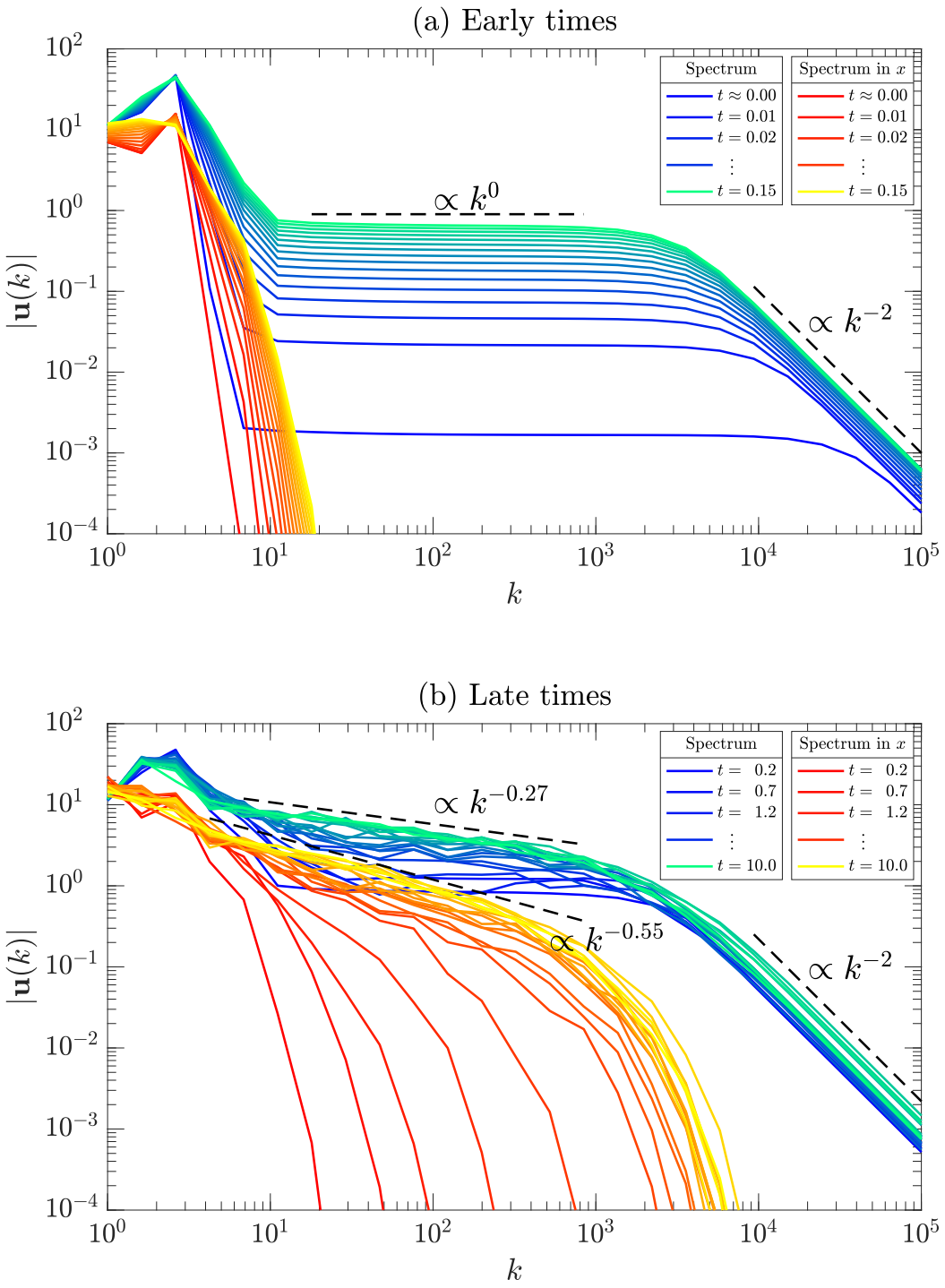

Fig. 10.1 Velocity spectra in logarithmic scales. In cold colors, we plot the total spectrum (10.11). In hot colors, we plot the spectrum (10.12) in x direction. (a) Spectra of solution for early times $t = 0, 0.01, 0.02, \ldots, 0.15$. (b) Spectra of solution for late times $t = 0.2, 0.7, 1.2, \ldots, 10.0$.

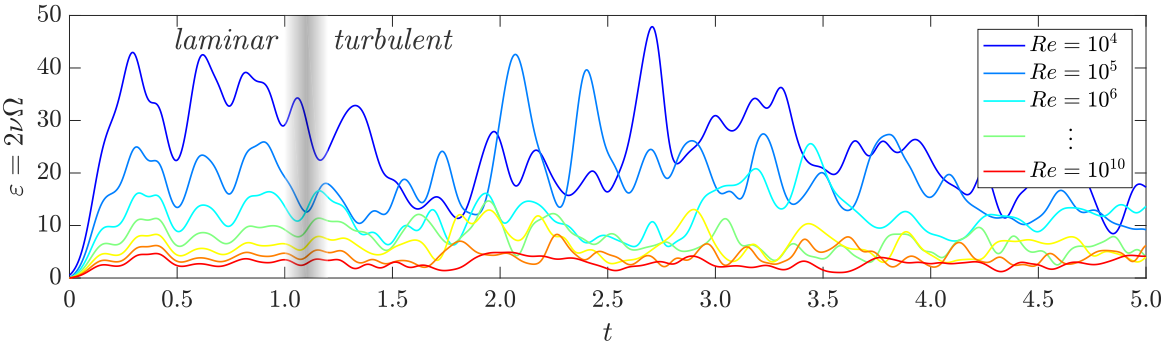

Fig. 10.2 Time evolution of the total dissipation $\varepsilon = 2\nu\Omega$ computed from the flow enstrophy $\Omega(t)$. Reynolds numbers $Re = 10^4, 10^5, 10^6, \ldots, 10^{10}$ increase from blue to red. The diffuse gray line roughly separates the laminar from the turbulent regimes.

10.4 Total dissipation at high Reynolds limit

Fig. 10.2 shows the time evolution of total dissipation for the different runs. From this picture, we can distinguish the two different regimes: at early times, when the flow is laminar, the total dissipation decreases monotonically; at later times, when it gets turbulent, humps and bumps in dissipation break monotonicity. The transition from an organized to a disorganized behavior is due to the appearence of chaotic oscillations in the field variables, already described in the previous section. The exact instant at which the transition occurs is, however, not clear.

In the laminar regime, the total dissipation seems to collapse to zero in the infinite Reynolds limit. After the flow is turbulized, a possible convergence is not so clear, since monotonicity is broken. This is the scenario in DNS [94, 43]. Some authors conjecture the lack of convergence from Navier-Stokes to Euler in view of those bursts in dissipation after the flow turbulence is triggered [122, 121]. But simulations on logarithmic lattices have the advantage of pushing the Reynolds number to incredibly large values. Despite the strong oscillations observed in the turbulent regime, the total dissipation appears to consistently decrease in average.

To verify how the solutions scale with Reynolds, we computed the maximum dissipation and the maximum force intensity $F = \nu J$ within two time windows: for the laminar regime, we consider the time window $t \in [0, 0.06]$; for the turbulent flow, $t \in [3.05, 3.50]$. The results are plotted in Fig.10.3. To explain the scaling of dissipation, we split the total dissipation into small and large scales contributions in the following

way. Let us consider the dissipation spectrum

$$\mathcal{E}(k) = \frac{\nu}{\Delta k} \sum_{k \leq |\mathbf{k}'| < \lambda k} |k'_x k'_y|^\alpha |\boldsymbol{\omega}(\mathbf{k}')|^2, \quad \text{with } \Delta k = \lambda k - k. \tag{10.16}$$

With this definition, the total dissipation rate ε is obtained by the sum

$$\varepsilon = \sum_{1 \leq k \leq k_N} \mathcal{E}(k) \Delta k. \tag{10.17}$$

The large $\mathcal{E}_l$ and small $\mathcal{E}_s$ scale contributions are expressed as

$$\mathcal{E}_l = \sum_{1 \leq k < k_{\text{cutoff}}} \mathcal{E}(k) \Delta k \quad \text{and} \quad \mathcal{E}_s = \sum_{k_{\text{cutoff}} \leq k < k_{N-1}} \mathcal{E}(k) \Delta k, \tag{10.18}$$

where we set $k_{\text{cutoff}} = \lambda^5$. Together, they sum up the total dissipation of the flow, *i.e.* $\varepsilon = \mathcal{E}_l + \mathcal{E}_s$.

When the flow is still laminar, Fig. 10.3(a) shows a clear convergence of dissipation towards zero. In the light of Kato's Theorem, the Navier-Stokes solutions are converging to the Euler's conservative solution. We can also study what is happening at different scales of motion.

For smaller Reynolds numbers, the total dissipation is dominated by large scales, which decay to zero as $\propto Re^{-1}$. Such scaling is expected by the following reason. The total dissipation is given by the product $\varepsilon = 2\nu\Omega$ between the viscosity ν and the enstrophy Ω. At large scales turn-over time is large, so there is not much variation in the enstrophy. If Ω is approximately constant in this regime, the dissipation is going to decay as $\varepsilon \propto \nu = Re^{-1}$. As Re increases, we have a transition, and the small scales start to dominate the flow. In this case, the dissipation is still converging to zero, but with the slower rate $\propto Re^{-0.123}$.

After the flow is turbulized, some aspects of the latter scenario change. We can see in Fig. 10.3(b) the development of constant plateau dissipation in intermediate values $10^3 \lessapprox Re \lessapprox 10^5$ of Reynolds number. The appearance of such plateau at this range of Reynolds numbers is consistent with DNS [122] and it might suggest the lack of convergence to the Euler conservative solution. State-of-art simulations, however, cannot achieve Reynolds numbers higher than 10^5, as it is easily reached by our logarithmic lattice model. By increasing Re, the plateau is followed by a consistent decrease in dissipation. This description agrees with the visual aspect of Fig. 10.2, in which the total dissipation is decreasing in average. This suggests that dissipation must vanish in the infinite Reynolds number.

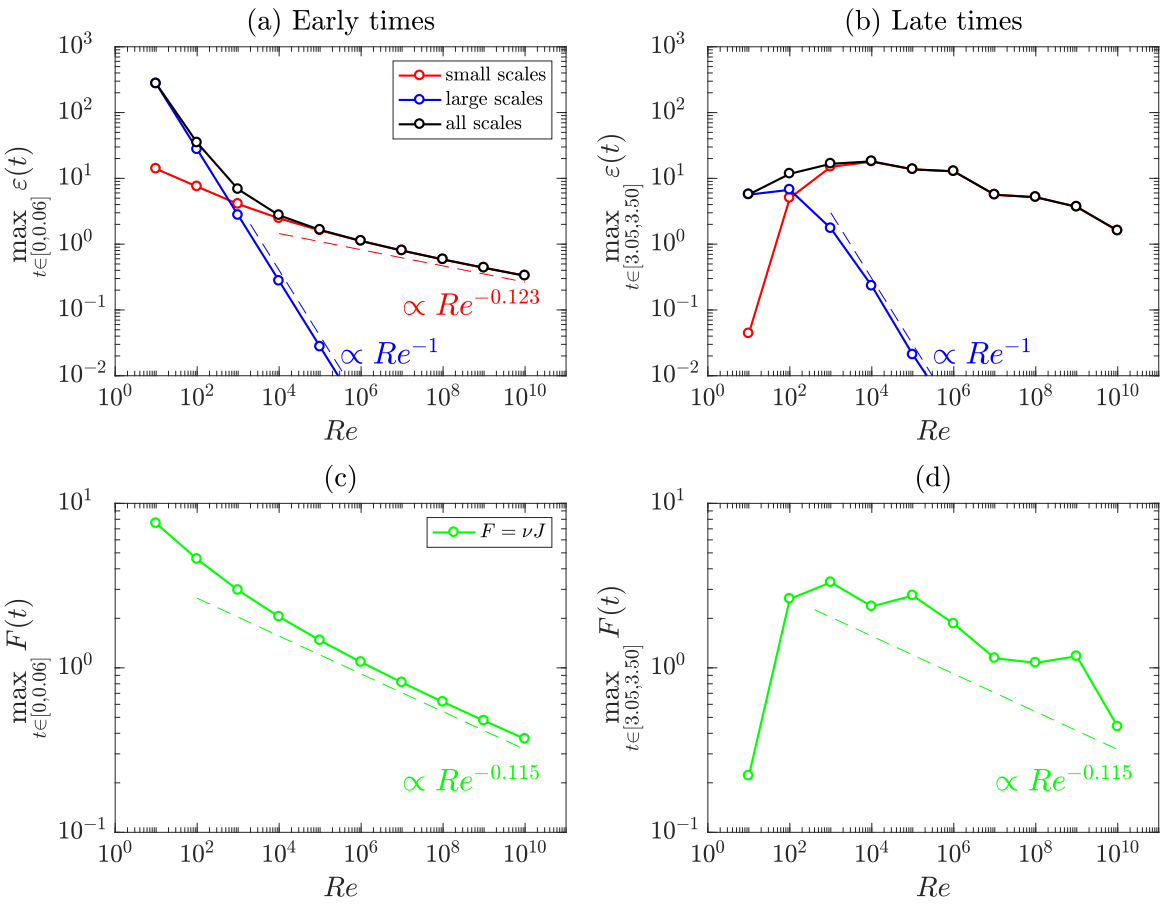

Fig. 10.3 Scaling of some global variables with respect to Reynolds numbers. The first row shows maximum dissipation ε, and the second row maximum force intensity $F = \nu J$. In the left, we consider early instants of time $t \in [0, 0.06]$, while in the right we study later times $t \in [3.05, 3.50]$.

Figs. 10.2(c) and (d) show the corresponding scalings of the force intensity $F = \nu J$ with respect to Reynolds. They both decrease to zero, indicating no residual boundary shear force in the vanishing viscosity limit. However, the aspect of the curves differ. In the laminar regime, the force intensity converges to a clear power law $\propto Re^{-0.115}$, while in the turbulent regime such scaling is obeyed in average only.

10.5 Discussion

The above results suggest that dissipation vanishes as Reynolds goes to infinity, even after the disrupt of turbulence. In view of Kato's Theorem, this means that the Navier-Stokes solutions converge to Euler's in the vanishing viscosity limit. Some comments need to be addressed about this result.

The flow is initially regular and confined to low k_x. A transition occurs, and a strong front quickly fills smaller k_x scales. Such transition also correlates with the appearance of strong dissipation events. This could be interpreted as the development of sharp gradients along boundaries as the flow detaches, which is also followed by extreme events in dissipation—see Figs. 1.4(d) and 1.5(a) for the DNS pictures. The vanishing dissipation rate in our logarithmic lattice suggests that those events are not getting sufficiently stronger in the infinite Reynolds limit, at least not to prevent the lack of convergence. Preliminar computations show that, as Reynolds increases, the transition takes more time to appear. This would explain why, in a fixed interval of time, the dissipation looks like is converging to a constant value, but start vanishing again as Reynolds increases: the transition instants drift away from the time window for larger Reynolds numbers.

In the case of dipole-wall collision, we don't expect the instant of transition to advance as the Reynolds number increases. Indeed, turbulence is triggered by the collision of the vortex against the wall, and the dipole travel time is supposedly governed by the Reynolds-independent bulk flow [126]. We remark, however, that the results on logarithmic lattices do not disagree with those from DNS [122, 121], if we compare total dissipation in their common Reynolds number range. For instance, if we look at the Reynolds interval $10^3 \leq Re \leq 10^5$, the dissipation in the logarithmic lattice model from Fig. 10.3(b) is similar to DNS results from Fig. 1.5(b).

As we mentioned in the description of the numerical setup, we performed some of the simulations with twenty less and twenty more nodes, in order to check the influence of lattice truncation on the results. The same qualitative picture was observed, with a quantitative comparison obstructed by chaotic behavior. We state, however, that more rigorous numerical study should be undertaken.

Appendix E

Transport and Divergence Theorems for discontinuity surfaces

In this appendix, we enunciate and proof the two main theorems used in the deductions of the discontinuous Navier-Stokes equations, established in Section 7.1. They are generalizations of well-known theorems from analysis: the Reynolds Transport Theorem (consult *e.g.* [42, p. 10]) and the Divergence Theorem (see *e.g.* [61, pp. 711–712]). In the formulations below, however, we consider the presence of possibly moving discontinuity surfaces, generating extra boundary terms to the classical balance laws. Despite the presentation, the following results are not new. We refer the reader to [114, pp. 124–127] for the proof of the discontinuous Transport Theorem. Other related references are [4, p. 86] and [150, pp. 525–529].

Theorem E.1 (Transport Theorem for discontinuity surfaces)**.** *Let $f(\mathbf{x},t)$ be a given scalar function with a jump discontinuity on a moving surface $\mathcal{S}_t$ immersed in the flow and moving with velocity $\mathbf{U}$. Assume that f is smooth elsewhere. Let Ω_t be a moving volume with velocity $\mathbf{u}$, possibly discontinuous on $\mathcal{S}_t$ and smooth elsewhere. Assume $\mathcal{S}_t$ splits Ω_t into two subvolumes indicated by Ω_t^- and Ω_t^+. Then*

$$\frac{d}{dt}\int_{\Omega_t} f(\mathbf{x},t)d\mathbf{x} = \int_{\Omega_t^-}\left(\frac{\partial f}{\partial t}+\nabla\cdot(f\mathbf{u})\right)d\mathbf{x} + \int_{\Omega_t^+}\left(\frac{\partial f}{\partial t}+\nabla\cdot(f\mathbf{u})\right)d\mathbf{x} + \int_{\mathcal{S}_t\cap\Omega_t}[f(\mathbf{U}-\mathbf{u})\cdot\mathbf{n}]dS, \quad \text{(E.1)}$$

where $[f]=f^+-f^-$ is the jump of f across $\mathcal{S}_t$, f^+ and f^- are the limit values of f on $\mathcal{S}_t$ from Ω_t^+ and Ω_t^- sides respectively, and $\mathbf{n}$ is the unit normal vector on $\mathcal{S}_t$ pointing from Ω_t^+ to Ω_t^-.

Proof. Since f and $\mathbf{u}$ are smooth in Ω^+, apply the classical Transport Theorem (7.1) in this subvolume, followed by applications of the classical Divergence Theorem to get

$$\begin{aligned}\frac{d}{dt}\int_{\Omega_t^+} f(\mathbf{x},t)d\mathbf{x} &= \int_{\Omega_t^+}(\partial_t f + \nabla\cdot(f\mathbf{u}))d\mathbf{x}\\ &= \int_{\Omega_t^+}\partial_t f d\mathbf{x} + \int_{\partial\Omega_t^+\cap\overline{\Omega_t}} f\mathbf{u}\cdot\mathbf{n}dS + \int_{\mathcal{S}_t\cap\Omega_t} f^+\mathbf{U}\cdot\mathbf{n}dS\\ &= \int_{\Omega_t^+}\partial_t f d\mathbf{x} + \int_{\partial\Omega_t^+} f\mathbf{u}\cdot\mathbf{n}dS - \int_{\mathcal{S}_t\cap\Omega_t} f^+\mathbf{u}^+\cdot\mathbf{n}dS + \int_{\mathcal{S}_t\cap\Omega_t} f^+\mathbf{U}\cdot\mathbf{n}dS\\ &= \int_{\Omega_t^+}\left(\partial_t f + \nabla\cdot(f\mathbf{u})\right)d\mathbf{x} + \int_{\mathcal{S}_t\cap\Omega_t} f^+(\mathbf{U}-\mathbf{u}^+)\cdot\mathbf{n}dS.\end{aligned} \tag{E.2}$$

Next, do the same to Ω_t^-, noting that $-\mathbf{n}$ is the outward unit normal vector to $\mathcal{S}_t$ with respect to Ω_t^-. We obtain

$$\frac{d}{dt}\int_{\Omega_t^-} f(\mathbf{x},t)d\mathbf{x} = \int_{\Omega_t^-}\left(\partial_t f + \nabla\cdot(f\mathbf{u})\right)d\mathbf{x} - \int_{\mathcal{S}_t\cap\Omega_t} f^-(\mathbf{U}-\mathbf{u}^-)\cdot\mathbf{n}dS. \tag{E.3}$$

Summing up Eqs. (E.2) and (E.3) leads to the desired result. □

Remark E.2. (One-dimensional case and Leibniz Integral Rule) Leibniz Integral Rule in one-dimensional space gives

$$\frac{d}{dt}\int_{a(t)}^{b(t)} f(x,t)dx = \int_{a(t)}^{b(t)}\frac{\partial f}{\partial t}dx + f(b(t),t)\frac{db}{dt} - f(a(t),t)\frac{da}{dt}. \tag{E.4}$$

If we allow f to have a jump discontinuity on a point $x=\xi(t)$, with $a(t)<\xi(t)<b(t)$, application of (E.4) twice – first on the interval $[a(t),\xi(t)]$ and next on $[\xi(t),b(t)]$ – gives

$$\frac{d}{dt}\int_{a(t)}^{b(t)} f(x,t)dx = \int_{a(t)}^{b(t)}\frac{\partial f}{\partial t}dx + f(b(t),t)\frac{db}{dt} - f(a(t),t)\frac{da}{dt} - [f]\frac{d\xi}{dt}, \tag{E.5}$$

where $[f]=f^+-f^-$, with f^+ and f^- the values of f at the right and the left of $\xi(t)$, respectively. Eq. (E.5) is the one-dimensional case of balance (E.1) and is commonly used in the study of shock propagation in partial differential equations – see *e.g.* [86, pp. 17–18].

Theorem E.3 (Divergence Theorem for discontinuity surfaces)**.** *Let $\boldsymbol{\sigma}=\sigma_{ij}(\mathbf{x},t)$ be a given rank-two tensor field with a jump discontinuity on a moving surface $\mathcal{S}_t$ immersed in the flow and moving with velocity $\mathbf{U}$. Assume that $\boldsymbol{\sigma}$ is smooth elsewhere. Let Ω_t be a moving volume with velocity $\mathbf{u}$ and assume $\mathcal{S}_t$ splits Ω_t into two subvolumes indicated*

by Ω_t^- *and* Ω_t^+*. Then*

$$\int_{\partial\Omega_t} \boldsymbol{\sigma}\cdot\mathbf{n}dS = \int_{\Omega_t^-} \nabla\cdot\boldsymbol{\sigma}d\mathbf{x} + \int_{\Omega_t^+} \nabla\cdot\boldsymbol{\sigma}d\mathbf{x} - \int_{\mathcal{S}_t\cap\Omega_t} [\boldsymbol{\sigma}\cdot\mathbf{n}]dS, \tag{E.6}$$

where $[\boldsymbol{\sigma}] = \boldsymbol{\sigma}^+ - \boldsymbol{\sigma}^-$ *is the jump of* $\boldsymbol{\sigma}$ *across* $\mathcal{S}_t$*,* $\boldsymbol{\sigma}^+$ *and* $\boldsymbol{\sigma}^-$ *are the limit values of* $\boldsymbol{\sigma}$ *on* $\mathcal{S}_t$ *from* Ω_t^+ *and* Ω_t^- *sides respectively, and* $\mathbf{n}$ *is the unit normal vector on* $\mathcal{S}_t$ *pointing from* Ω_t^+ *to* Ω_t^-*.*

Proof. This proof follows similar steps as those for the Transport Theorem E.1. Since $\boldsymbol{\sigma}$ is smooth within each subvolume Ω_t^+ and Ω_t^-, we apply the Classical Divergence Theorem twice to obtain

$$\begin{aligned}\int_{\Omega_t} \partial_j\sigma_{ij}d\mathbf{x} &= \int_{\Omega_t^-} \partial_j\sigma_{ij}d\mathbf{x} + \int_{\Omega_t^+} \partial_j\sigma_{ij}d\mathbf{x}\\ &= \int_{\partial\Omega_t^-\cap\overline{\Omega_t}} \sigma_{ij}n_j dS - \int_{\mathcal{S}_t\cap\Omega_t} \sigma_{ij}^- n_j dS + \int_{\partial\Omega_t^+\cap\overline{\Omega_t}} \sigma_{ij}n_j dS + \int_{\mathcal{S}_t\cap\Omega_t} \sigma_{ij}^+ n_j dS\\ &= \int_{\partial\Omega_t} \sigma_{ij}n_j dS + \int_{\mathcal{S}_t\cap\Omega_t} [\sigma_{ij}n_j]dS,\end{aligned} \tag{E.7}$$

which is an index notation for the desired result. □

Appendix F

Boundary conditions and nonuniqueness of discontinuous shear flows

The purpose of this appendix is to show that, after extending the flow on the upper-half space to the whole space, we cannot suppress the boundary condition on the discontinuity surface, otherwise the problem becomes ill-posed. We are going to show that, when considering the system without the no-slip condition, we have nonunique solutions.

F.1 Model formulation

Let us consider the one-dimensional shear flow $u = u(y,t)$ in the upper-half line $y > 0$ with a solid boundary at the origin $y = 0$. The system is governed by

$$\begin{cases} \partial_t u = \nu \partial_y^2 u & \text{in } y > 0, \\ u = 0 & \text{on } y = 0. \end{cases} \tag{F.1}$$

Using our strategy of discontinuity surfaces, we extend problem (F.1) to the whole two-dimensional plane $\mathbb{R}^2$ under the symmetry

$$u(y,t) = u(-y,t), \tag{F.2}$$

and add a singular forcing term to the governing equations. The resulting system is

$$\begin{cases} \partial_t u = \nu \partial_y^2 u - \nu [\partial_y u] \delta(y) & \text{in } \mathbb{R} \\ u(y,t) = u(-y,t) & \text{for } y \in \mathbb{R},\ t > 0 \\ u = 0 & \text{at} y = 0 \end{cases} \tag{F.3}$$

where $[\partial_y u]$ is the jump in the y-derivative across $y = 0$. In system (F.3), no-slip condition $u = 0$ is imposed at the discontinuity point $y = 0$. Let us consider the system without this condition

$$\begin{cases} \partial_t u = \nu \partial_y^2 u - \nu [\partial_y u] \delta(y) & \text{in } \mathbb{R} \\ u(y,t) = u(-y,t) & \text{for } y \in \mathbb{R},\ t > 0. \end{cases} \tag{F.4}$$

We are going to show that system (F.4) has nonunique solutions. This attest that we cannot suppress the no-slip condition from system (F.3).

F.2 Nonuniqueness of solutions

Using well-known facts about the heat equation, we shall construct two distinct solutions for the singular system (F.4): the first one is the physical solution of a no-slip plate, *i.e.*, it satisfies the no-slip boundary condition for all instants of time; the second one satisfies the no-slip condition at the initial condition, but loses it as time advances.

F.2.1 Dirichlet problem for the heat equation

We condider the heat equation with Dirichlet boundary condition

$$\begin{cases} \partial_t u = \nu \partial_y^2 u & (y,t) \in (0,\infty) \times (0,\infty), \\ u(y,0) = g(y) & \text{IC}, \\ u(0,t) = 0 & \text{BC (Dirichlet)}. \end{cases} \tag{F.5}$$

Problem (F.5) can be solved using the fundamental solution of the heat equation as follows. We extend the solution to the whole line through an odd reflection $u(y) = -u(-y)$, with initial condition $g(y) = -g(-y)$. Then the solution is given by

$$u(y,t) = \int_0^\infty \left(K(y,x,t) - K(y,-x,t) \right) g(x) dx, \tag{F.6}$$

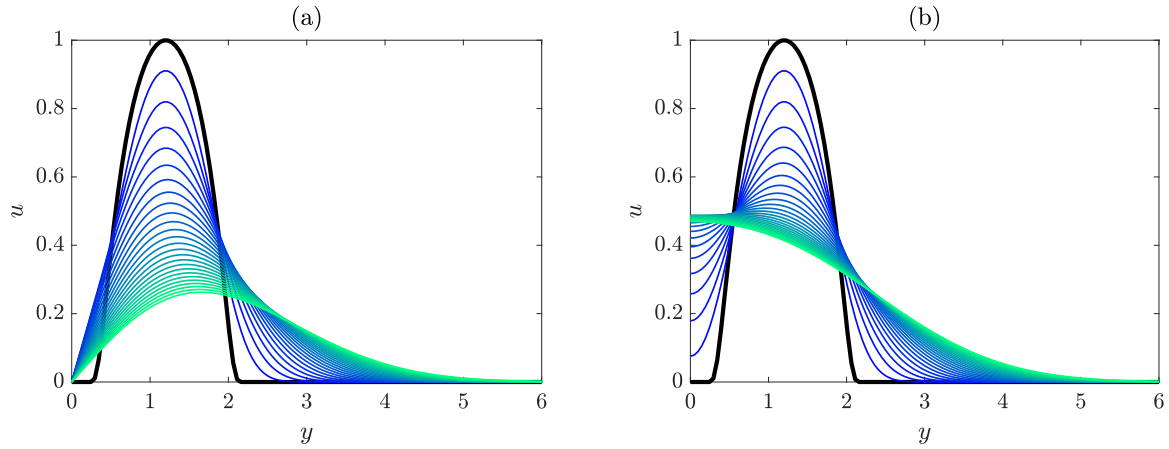

Fig. F.1 Two distinct solutions for the singular model (F.4) from the same intial condition (in black). Both solutions satisfy no-slip $u = 0$ at $y = 0$ at the initial instant. Colors change from blue to green as time advances. (a) physical solution, obtained from imposing Dirichlet boundary condition $u = 0$ at $y = 0$; (b) slip solution, satisfying the Neumann boundary condition $\partial_y u = 0$ at $y = 0$.

where

$$K(y, x, t) = \frac{e^{-|y-x|^2/4\nu t}}{(4\pi\nu t)^{1/2}} \tag{F.7}$$

is the heat kernel. Explicitly, the solution is

$$u(y, t) = \frac{1}{(4\pi\nu t)^{1/2}} \int_0^\infty \left(e^{-|y-x|^2/4\nu t} - e^{-|y+x|^2/4\nu t} \right) g(x) dx. \tag{F.8}$$

F.2.2 Neumann problem for the heat equation

We condider the heat equation with Dirichlet boundary condition

$$\begin{cases} \partial_t u = \nu \partial_y^2 u & (y, t) \in (0, \infty) \times (0, \infty), \\ u(y, 0) = g(y) & \text{IC}, \\ \partial_y u(0, t) = 0 & \text{BC (Neumann)}. \end{cases} \tag{F.9}$$

Problem (F.5) can be solved using the fundamental solution of the heat equation as follows. We extend the solution to the whole line through an even reflection $u(y) = u(-y)$, with initial condition $g(y) = g(-y)$. Then the solution is given by

$$u(y, t) = \int_0^\infty \left(K(y, x, t) + K(y, -x, t) \right) g(x) dx. \tag{F.10}$$

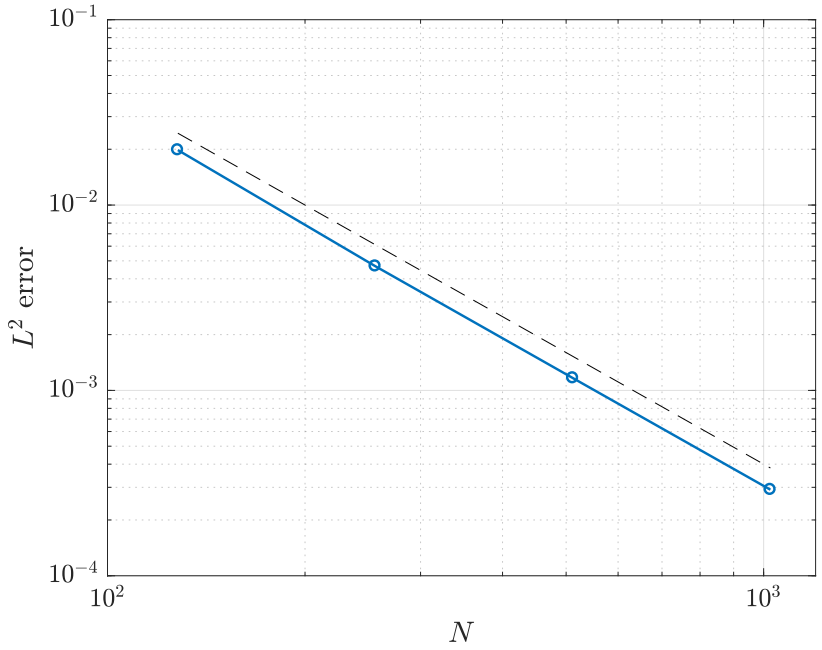

Fig. F.2 Convergence of no-slip numerical solution for the singular system. Error is plotted against different number of grid points N. Dashed line has slope $\propto N^{-2}$.

Explicitly, the solution is

$$u(y,t) = \frac{1}{(4\pi\nu t)^{1/2}} \int_0^\infty \left(e^{-|y-x|^2/4\nu t} + e^{-|y+x|^2/4\nu t} \right) g(x) dx. \tag{F.11}$$

F.2.3 Two distinct solutions for the shear flow problem

We fix an initial condition

$$g(y) = C \exp\left(-\frac{1}{1-|y-y_0|^2} \right), \tag{F.12}$$

with $y_0 = 1.2$ and C such that $\max_y g(y) = 1$. Such function has compact support $\operatorname{supp} g = [0.2, 2.2]$; particularly, $g(0) = 0$. Fig. F.1 shows the graph of g.

First solution. We take the solution of the Dirichlet problem (F.5) and extend it to the whole line through the reflection $u(-y) = u(y)$. Then, we know that this is a solution for the singular system (F.4). Moreover, this solution satisfies the no-slip condition $u = 0$ at $y = 0$. This is actually the physical solution of the problem. See Fig. F.1(a).

Second solution. We take the solution of the Dirichlet problem (F.9) and extend it to the whole line through the reflection $u(-y) = u(y)$. This trivially satisfies the singular model, since in this case $[\partial_y u] = 0$ at all instants of time. Moreover, this solution satisfies the no-slip condition at the initial condition. However, the solution slips at $y = 0$ as time advances. See Fig. F.1(b).

F.2.4 Numerical validation

Let u be one of the two solutions above of the singular system (F.4). Integrating with respect to y, yields

$$\frac{d}{dt}\int_{-\infty}^{\infty} u(y)dy = \nu\int_{-\infty}^{\infty} \partial_y^2 u dy - \nu[\partial_y u]. \tag{F.13}$$

We can obtain an approximation $\widetilde{u}$ by solving the heat equation with appropriate initial conditions (reflections). We do it through pseudospectral methods, in a box $[-L, L]$ for sufficiently large L (this is a good approximation for short times, since the initial condition has compact support). Then, we construct the solution for the singular system by considering the relfection $\widetilde{u}(-y) = \widetilde{u}(y)$, and define the residue

$$\mathrm{res}(t) = \frac{d}{dt}\int_{-L}^{L} \widetilde{u}(y)dy - \nu\int_{-L}^{L} \partial_y^2 \widetilde{u} dy + \nu[\partial_y \widetilde{u}]. \tag{F.14}$$

The global error is computed as the L^2 norm in time

$$\mathrm{error} = \left(\int_0^1 \mathrm{res}(t)^2 dt\right)^{1/2}. \tag{F.15}$$

For the slip solution, the residue can be computed with high accuracy, since the solution is everywhere smooth (the jump is identically zero). In this case, we have error $\approx 10^{-12}$ even for small number of points $N \approx 128$.

For the no-slip solution, we show convergence error $\to 0$ as $N \to \infty$—see Fig. F.2. The slope error $\propto N^{-2}$ relates to the smoothness of the solution u, which is only continuous, with a jump singularity in the first derivative.

Chapter 11

Conclusions

We propose a new strategy for constructing simplified models of fluid dynamics, which restricts the governing equations in their original form to a multi-dimensional logarithmic lattice in Fourier space. This domain receives a specially designed operational structure, which retains most of the usual calculus and algebraic properties. As a consequence, the resulting models preserve all symmetries (some in discrete form, namely scaling invariance and isotropy), inviscid invariants (energy and helicity, for 3D flow; energy and enstrophy, for 2D flow), and also reproduces some fine properties of Euler flow, like incompressibility and Kelvin's Circulation Theorem. The classification of all possible lattices supporting this construction allows us to obtain different dynamical models sharing all the above properties, and so to test the robustness and universality of the results they provide. Because of the strongly decimated domain, the logarithmic models can be easily simulated with great accuracy and covering a large spatial range. Furthermore, the solutions correlate with existing DNS at the correspondent scales [29].

After showing rigorously that analytical properties of plausible finite-time singularities (blowup) for the incompressible 3D Euler equations have similar form on the logarithmic lattice, we presented the numerical evidence of blowup, characterized as a chaotic wave in a renormalized system. Surprisingly very similar asymptotic behavior of solutions was observed for two very different lattice models, probing the robustness of our conclusions, also drawn earlier in [29]. The multi-scale character of the attractor (ranging six decades in Fourier space) reveals the great complexity of the blowup and explains why there is a controversy around the available numerical studies, since actual computational techniques may be insufficient by far for the required resolution. Still, one may think of accessing the blowup through experimental measurements [138, 96, 52].

The viscous incompressible model on a logarithmic lattice exhibits anomalous dissipation in the limit of large Reynolds numbers, similarly to hydrodynamics turbulence [69]. This was demonstrated by measuring the mean energy flux in the inertial range for a sequence of decreasing viscosities. Moreover, statistics of lattice variables behave like Fourier components in the full Navier-Stokes turbulence, whose distributions are Gaussian in the inertial interval and intermittent at viscous scales. Such behavior contrasts with other simplified models, like shell models, which usually display some degree of inertial-range intermittency. The question whether our logarithmic model reproduces a kind of physical-space intermittency was left open. We believe that future analysis of this model may help in better understanding the relation between physical and Fourier space representations in developed turbulence [19].

We showed that logarithmic lattices are able to model systems with solid boundaries. We explored several examples of shear flows to create intuition on the unusual description of flows with walls in Fourier space. The vanishing viscosity problem was approached for two-dimensional flows in the presence of a flat solid boundary. We tracked total dissipation, in the light of Kato's Theorem. As time evolves, a laminar organized regime is followed by a chaotic turbulent state. This resembles the development of small-scale structures in the dipole-wall collision. Nevertheless, the Navier-Stokes solutions seem to converge to Euler's in the infinite Reynolds limit. We argued that this fact does not contradict the reported DNS from literature, since the results are in agreement in the resolution accessible to the state-of-the-art DNS. Further investigation, however, is needed to obtain a better understanding of this challenging problem. Still, the logarithmic lattice model looks like a promising tool for this problem, since it reaches the large Reynolds number $Re = 10^{10}$ with moderate computational effort compared to the expensive DNS [122, 43, 121] limited to $Re = 10^5$.

The systematic technique we presented is applicable to any partial differential equation with quadratic nonlinearities. In this framework, symmetries and quadratic invariants are expected to be automatically preserved due to the designed functional structure on the lattice. This turns the logarithmic models into a general methodology for the study of singularities and regularity in many nonlinear systems. We also developed the library LogLatt [28], an efficient Matlab® computational tool for the numerical calculus on logarithmic lattices. The proposed technique is ready-to-use in other fluid models, like natural convection [113], geostrophic motion [128, 47], porous media [48] and magnetohydrodynamics [15]. We expect logarithmic models can establish important examples of the deep connection between finite time singularities and spontaneous stochasticity in fluid models [112, 111, 148], specially for the SQG

equations [152]. The lower computational cost of the logarithmic models compared to full DNS may be of great use for problems in higher dimensions, like high-dimensional turbulence [75, 117, 144, 155]. With further extensions, there is a hope to apply this technique to compressible turbulence [5, 65] and superfluids [12, 13]; see the example in Appendix C of a possible way to model isentropic compressible flow on logarithmic lattices.

References

[1] J. Aarts, R. Fokkink, and G. Kruijtzer. Morphic numbers. *Nieuw Arch. Wiskd.*, 2:56–58, 2001.

[2] D. S. Agafontsev, E. A. Kuznetsov, and A. A. Mailybaev. Development of high vorticity structures in incompressible 3D Euler equations. *Phys. Fluids*, 27:085102, 2015.

[3] D. S. Agafontsev, E. A. Kuznetsov, and A. A. Mailybaev. Asymptotic solution for high-vorticity regions in incompressible three-dimensional Euler equations. *J. Fluid Mech.*, 813:R1, 2017.

[4] R. Aris. *Vectors, Tensors and the Basic Equations of Fluid Mechanics*. Dover, 1962.

[5] P. Augier, A. V. Mohanan, and E. Lindborg. Shallow water wave turbulence. *J. Fluid Mech.*, 874:1169–1196, 2019.

[6] J. T. Beale, T. Kato, and A. Majda. Remarks on the breakdown of smooth solutions for the 3-D Euler equations. *Comm. Math. Phys.*, 94(1):61–66, 1984.

[7] R. Benzi, L. Biferale, A. Crisanti, G. Paladin, M. Vergassola, and A. Vulpiani. A random process for the construction of multiaffine fields. *Physica D*, 65(4):352–358, 1993.

[8] R. Benzi, L. Biferale, S. Succi, and F. Toschi. Intermittency and eddy viscosities in dynamical models of turbulence. *Phys. Fluids*, 11(5):1221–1228, 1999.

[9] R. Benzi, L. Biferale, R. Tripiccione, and E. Trovatore. (1+ 1)-dimensional turbulence. *Phys. Fluids*, 9(8):2355–2363, 1997.

[10] R. Benzi and U. Frisch. Turbulence. *Scholarpedia*, 5(3):3439, 2010.

[11] L. Biferale. Shell models of energy cascade in turbulence. *Ann. Rev. Fluid Mech.*, 35:441–468, 2003.

[12] L. Biferale, D. Khomenko, V. L'vov, A. Pomyalov, I. Procaccia, and G. Sahoo. Superfluid helium in three-dimensional counterflow differs strongly from classical flows: Anisotropy on small scales. *Phys. Rev. Lett.*, 122(14):144501, 2019.

[13] L. Biferale, D. Khomenko, V. S. L'vov, A. Pomyalov, I. Procaccia, and G. Sahoo. Strong anisotropy of superfluid He 4 counterflow turbulence. *Phys. Rev. B*, 100(13):134515, 2019.

[14] L. Biferale and I. Procaccia. Anisotropy in turbulent flows and in turbulent transport. *Phys. Rep.*, 414(2-3):43–164, 2005.

[15] D. Biskamp. *Nonlinear Magnetohydrodynamics*. Cambridge University Press, 1997.

[16] T. Bohr, M. H. Jensen, G. Paladin, and A. Vulpiani. *Dynamical Systems Approach to Turbulence*. Cambridge University Press, 2005.

[17] M. E. Brachet, M. Meneguzzi, A. Vincent, H. Politano, and P. L. Sulem. Numerical evidence of smooth self-similar dynamics and possibility of subsequent collapse for three-dimensional ideal flows. *Phys. Fluids A*, 4:2845–2854, 1992.

[18] M. P. Brenner, S. Hormoz, and A. Pumir. Potential singularity mechanism for the Euler equations. *Phys. Rev. Fluids*, 1(8):084503, 2016.

[19] C. Brun and A. Pumir. Statistics of Fourier modes in a turbulent flow. *Phys. Rev. E*, 63(5):056313, 2001.

[20] T. Buckmaster, C. De Lellis, P. Isett, and L. Székelyhidi Jr. Anomalous dissipation for 1/5-Hölder Euler flows. *Ann. of Math.*, 182(1):127–172, 2015.

[21] T. Buckmaster, C. De Lellis, L. Székelyhidi, and V. Vicol. Onsager's conjecture for admissible weak solutions. *Comm. Pure Appl. Math.*, 72(2):229–274, 2019.

[22] J. M. Burgers. A mathematical model illustrating the theory of turbulence. *Adv. in Appl. Mech.*, 1:171–199, 1948.

[23] M. D. Bustamante and M. Brachet. Interplay between the Beale-Kato-Majda theorem and the analyticity-strip method to investigate numerically the incompressible Euler singularity problem. *Physical Review E*, 86(6):066302, 2012.

[24] M. Buzzicotti, A. Bhatnagar, L. Biferale, A. S. Lanotte, and S. S. Ray. Lagrangian statistics for Navier–Stokes turbulence under Fourier-mode reduction: fractal and homogeneous decimations. *New J. Phys.*, 18(11):113047, 2016.

[25] M. Buzzicotti, L. Biferale, U. Frisch, and S. S. Ray. Intermittency in fractal Fourier hydrodynamics: Lessons from the Burgers equation. *Phys. Rev. E*, 93(3):033109, 2016.

[26] C. S. Campolina. Fluid Dynamics on Logarithmic Lattices and Singularities of Euler Flow. Master's Thesis, Instituto de Matemática Pura e Aplicada, 2019.

[27] C. S. Campolina. Loglatt: A computational library for the calculus and flows on logarithmic lattices. *arXiv preprint arXiv:2006.00047*, 2020.

[28] C. S. Campolina. LogLatt: A computational library for the calculus on logarithmic lattices, 2020. Freely available for noncommercial use from MATLAB Central File Exchange (https://www.mathworks.com/matlabcentral/fileexchange/76295-loglatt).

[29] C. S. Campolina and A. A. Mailybaev. Chaotic blowup in the 3D incompressible Euler equations on a logarithmic lattice. *Phys. Rev. Lett.*, 121:064501, 2018.

[30] C. S. Campolina and A. A. Mailybaev. Fluid dynamics on logarithmic lattices. *Nonlinearity*, 34(7):4684, 2021.

[31] H. Cartan. *Calcul Différentiel*. Hermann, 1967.

[32] D. Chae. Nonexistence of self-similar singularities for the 3D incompressible Euler equations. *Commun. Math. Phys.*, 273(1):203–215, 2007.

[33] D. Chae. Incompressible Euler Equations: the blow-up problem and related results. In *Handbook of Differential Equations: Evolutionary Equations*, volume 4, pages 1–55. Elsevier, 2008.

[34] D. Chae and R. Shvydkoy. On formation of a locally self-similar collapse in the incompressible Euler equations. *Arch. Ration. Mech. Anal.*, 209(3):999–1017, 2013.

[35] J. Chen and T. Y. Hou. Finite time blowup of 2D Boussinesq and 3D Euler equations with $C^{1,\alpha}$ velocity and boundary. *Communications in Mathematical Physics*, 383(3):1559–1667, 2021.

[36] S. Chen, G. Doolen, J. R. Herring, R. H. Kraichnan, S. A. Orszag, and Z. S. She. Far-dissipation range of turbulence. *Phys. Rev. Lett.*, 70(20):3051, 1993.

[37] A. Cheskidov. Blow-up in finite time for the dyadic model of the Navier-Stokes equations. *Trans. Amer. Math. Soc.*, 360(10):5101–5120, 2008.

[38] A. Cheskidov, P. Constantin, S. Friedlander, and R. Shvydkoy. Energy conservation and Onsager's conjecture for the Euler equations. *Nonlinearity*, 21(6):1233–1252, 2008.

[39] A. Cheskidov and K. Zaya. Regularizing effect of the forward energy cascade in the inviscid dyadic model. *Proc. Amer. Math. Soc.*, 144(1):73–85, 2016.

[40] L. Chevillard, N. Mazellier, C. Poulain, Y. Gagne, and C. Baudet. Statistics of Fourier modes of velocity and vorticity in turbulent flows: Intermittency and long-range correlations. *Phys. Rev. Lett.*, 95(20):200203, 2005.

[41] K. Choi, T. Y. Hou, A. Kiselev, G. Luo, V. Sverak, and Y. Yao. On the finite-time blowup of a one-dimensional model for the three-dimensional axisymmetric Euler equations. *Comm. Pure Appl. Math.*, 70(11):2218–2243, 2017.

[42] A. J. Chorin and J. E. Marsden. *A Mathematical Introduction to Fluid Mechanics*. Springer, 2nd edition, 1990.

[43] H. J. H. Clercx and G. J. F. Van Heijst. Dissipation of coherent structures in confined two-dimensional turbulence. *Physics of Fluids*, 29(11):111103, 2017.

[44] J. S. Cohen. *Computer Algebra and Symbolic Computation: Mathematical Methods*. AK Peters/CRC Press, 2003.

[45] P. Constantin, P. D. Lax, and A. Majda. A simple one-dimensional model for the three-dimensional vorticity equation. *Comm. Pure Appl. Math.*, 38(6):715–724, 1985.

[46] P. Constantin, B. Levant, and E. Titi. Regularity of inviscid shell models of turbulence. *Phys. Rev. E*, 75:016304, 2007.

[47] P. Constantin, A. J. Majda, and E. Tabak. Formation of strong fronts in the 2-D quasigeostrophic thermal active scalar. *Nonlinearity*, 7(6):1495–1533, 1994.

[48] D. Córdoba, F. Gancedo, and R. Orive. Analytical behavior of two-dimensional incompressible flow in porous media. *J. Math. Phys.*, 48(6):065206, 2007.

[49] S. M. Cox and P. C. Matthews. Exponential time differencing for stiff systems. *J. Comput. Phys.*, 176(2):430–455, 2002.

[50] M. De Pietro, L. Biferale, and A. A. Mailybaev. Inverse energy cascade in nonlocal helical shell models of turbulence. *Phys. Rev. E*, 92(4):043021, 2015.

[51] M. De Pietro, A. A. Mailybaev, and L. Biferale. Chaotic and regular instantons in helical shell models of turbulence. *Phys. Rev. Fluids*, 2(3):034606, 2017.

[52] P. Debue, V. Shukla, D. Kuzzay, D. Faranda, E.-W. Saw, F. Daviaud, and B. Dubrulle. Dissipation, intermittency, and singularities in incompressible turbulent flows. *Phys. Rev. E*, 97(5):053101, 2018.

[53] H. Van der Laan. *Le Nombre Plastique: Quinze Leçons sur l'Ordonnance Architectonique*. Brill, Leiden, 1960.

[54] V. N. Desnyansky and E. A. Novikov. The evolution of turbulence spectra to the similarity regime. *Izv. Akad. Nauk SSSR, Fiz. Atmos. Okeana*, 10:127–136, 1974.

[55] P. D. Ditlevsen. Symmetries, invariants, and cascades in a shell model of turbulence. *Phys. Rev. E*, 62:484–489, 2000.

[56] T. Dombre and J. L. Gilson. Intermittency, chaos and singular fluctuations in the mixed Obukhov–Novikov shell model of turbulence. *Physica D*, 111(1–4):265–287, 1998.

[57] D. G. Ebin and J. E. Marsden. Groups of diffeomorphisms and the solution of the classical Euler equations for a perfect fluid. *Bull. Amer. Math. Soc.*, 75(5):962–967, 1969.

[58] J. Eggers and M. A. Fontelos. The role of self-similarity in singularities of partial differential equations. *Nonlinearity*, 22:R1, 2009.

[59] J. Eggers and S. Grossmann. Does deterministic chaos imply intermittency in fully developed turbulence? *Phys. Fluids A*, 3(8):1958–1968, 1991.

[60] T. M. Elgindi and I.-J. Jeong. Finite-time singularity formation for strong solutions to the axi-symmetric 3D Euler equations. *Ann. PDE*, 5(2):16, 2019.

[61] L. C. Evans. *Partial Differential Equations*, volume 19 of *Graduate Studies in Mathematics*. American Mathematical Society, 2nd edition, 2010.

[62] G. L. Eyink. Large-N limit of the "spherical model" of turbulence. *Phys. Rev. E*, 49(5):3990, 1994.

[63] G. L. Eyink. Dissipative anomalies in singular Euler flows. *Physica D*, 237:1956–1968, 2008.

[64] G. L. Eyink and K. R. Sreenivasan. Onsager and the theory of hydrodynamic turbulence. *Rev. Modern Phys.*, 78(1):87–135, 2006.

[65] G. Falkovich and A. G. Kritsuk. How vortices and shocks provide for a flux loop in two-dimensional compressible turbulence. *Phys. Rev. Fluids*, 2(9):092603, 2017.

[66] C. L. Fefferman. Existence and smoothness of the Navier-Stokes equation. In *The millennium prize problems*, pages 57–67. AMS, 2006.

[67] E. Fehlberg. Klassische Runge-Kutta-Formeln vierter und niedrigerer Ordnung mit Schrittweiten-Kontrolle und ihre Anwendung auf Wärmeleitungsprobleme. *Computing*, 6:61–71, 1970.

[68] N. Fehn, M. Kronbichler, P. Munch, and W. A. Wall. Numerical evidence of anomalous energy dissipation in incompressible Euler flows: towards grid-converged results for the inviscid Taylor–Green problem. *Journal of Fluid Mechanics*, 932, 2022.

[69] U. Frisch. *Turbulence: the Legacy of A.N. Kolmogorov*. Cambridge University Press, 1995.

[70] U. Frisch, T. Matsumoto, and J. Bec. Singularities of Euler flow? Not out of the blue! *J. Stat. Phys.*, 113:761–781, 2003.

[71] U. Frisch, A. Pomyalov, I. Procaccia, and S.S. Ray. Turbulence in noninteger dimensions by fractal fourier decimation. *Phys. Rev. Lett.*, 108:074501, 2012.

[72] J. D. Gibbon. The three-dimensional Euler equations: Where do we stand? *Physica D*, 237(14-17):1894–1904, 2008.

[73] E. B. Gledzer. System of hydrodynamic type admitting two quadratic integrals of motion. *Sov. Phys. Doklady*, 18:216, 1973.

[74] D. Goldstein, R. Handler, and L. Sirovich. Modeling a no-slip flow boundary with an external force field. *Journal of Computational Physics*, 105(2):354–366, 1993.

[75] T. Gotoh, Y. Watanabe, Y. Shiga, T. Nakano, and E. Suzuki. Statistical properties of four-dimensional turbulence. *Phys. Rev. E*, 75(1):016310, 2007.

[76] T. Grafke, H. Homann, J. Dreher, and R. Grauer. Numerical simulations of possible finite time singularities in the incompressible Euler equations: comparison of numerical methods. *Physica D*, 237(14):1932–1936, 2008.

[77] R. Grauer, C. Marliani, and K. Germaschewski. Adaptive mesh refinement for singular solutions of the incompressible Euler equations. *Phys. Rev. Lett.*, 80(19):4177, 1998.

[78] S. Grossmann and D. Lohse. Intermittency in the Navier–Stokes dynamics. *Z. Phys. B*, 89(1):11–19, 1992.

[79] S. Grossmann, D. Lohse, and A. Reeh. Developed turbulence: From full simulations to full mode reductions. *Phys. Rev. Lett.*, 77(27):5369, 1996.

[80] Ö. D. Gürcan. Nested polyhedra model of turbulence. *Phys. Rev. E*, 95:063102, 2017.

[81] Ö. D. Gürcan, S. Xu, and P. Morel. Spiral chain models of two-dimensional turbulence. *Phys. Rev. E*, 100:043113, 2019.

[82] T. Y. Hou. Blow-up or no blow-up? A unified computational and analytic approach to 3D incompressible Euler and Navier–Stokes equations. *Acta Numer.*, 18:277–346, 2009.

[83] T. Y. Hou and R. Li. Dynamic depletion of vortex stretching and non-blowup of the 3-D incompressible Euler equations. *J. Nonlinear Sci.*, 16(6):639–664, 2006.

[84] T. Y. Hou and R. Li. Computing nearly singular solutions using pseudo-spectral methods. *J. Comp. Phys.*, 226(1):379–397, 2007.

[85] P. Isett. A proof of Onsager's conjecture. *Ann. of Math.*, 188(3):871–963, 2018.

[86] F. John. *Partial Differential Equations*, volume 1 of *Applied Mathematical Sciences*. Springer, 3rd edition, 1978.

[87] Y. Kaneda, T. Ishihara, M. Yokokawa, K. Itakura, and A. Uno. Energy dissipation rate and energy spectrum in high resolution direct numerical simulations of turbulence in a periodic box. *Phys. Fluids*, 15(2):L21–L24, 2003.

[88] T. Kato. Nonstationary flows of viscous and ideal fluids in R^3. *J. Funct. Anal.*, 9(3):296–305, 1972.

[89] T. Kato. Remarks on zero viscosity limit for nonstationary Navier-Stokes flows with boundary. In *Seminar on nonlinear partial differential equations*, pages 85–98. Springer, 1984.

[90] N. H. Katz and N. Pavlović. Finite time blow-up for a dyadic model of the Euler equations. *Trans. Amer. Math. Soc.*, 357(2):695–708, 2005.

[91] R. M. Kerr. Evidence for a singularity of the three-dimensional, incompressible Euler equations. *Phys. Fluids A*, 5(7):1725–1746, 1993.

[92] R. M. Kerr. Bounds for Euler from vorticity moments and line divergence. *J. Fluid Mech.*, 729:R2, 2013.

[93] A. Kiselev. Small scales and singularity formation in Fluid Dynamics. In *Proc. Int. Cong. of Math.*, volume 2, pages 2329–2356, Rio de Janeiro, 2018.

[94] W. Kramer, H. J. H. Clercx, and G. J. F. Van Heijst. Vorticity dynamics of a dipole colliding with a no-slip wall. *Physics of Fluids*, 19(12):126603, 2007.

[95] I. Kukavica and V. Vicol. Remarks on the inviscid limit problem for the Navier-Stokes equations. *Pure and applied functional analysis*, 7(1), 2022.

[96] D. Kuzzay, E.-W. Saw, F. Martins, D. Faranda, J.-M. Foucaut, F. Daviaud, and B. Dubrulle. New method for detecting singularities in experimental incompressible flows. *Nonlinearity*, 30(6):2381, 2017.

[97] L. D. Landau and E. M. Lifshitz. *Quantum Mechanics: Non-Relativistic Theory*, volume 3. Butterworth-Heinemann, 1981.

[98] L. D. Landau and E. M. Lifshitz. *Fluid Mechanics*, volume 6. Pergamon, 1987.

[99] A. Larios, M. R. Petersen, E. S. Titi, and B. Wingate. A computational investigation of the finite-time blow-up of the 3D incompressible Euler equations based on the Voigt regularization. *Theor. Comput. Fluid Dyn.*, 32(1):23–34, 2018.

[100] J. Leray. Sur le mouvement d'un liquide visqueux emplissant l'espace. *Acta Math.*, 63:193–248, 1934.

[101] R. J. LeVeque. *Finite difference methods for ordinary and partial differential equations: steady-state and time-dependent problems*. SIAM, 2007.

[102] L. Lichtenstein. Über einige Existenzprobleme der Hydrodynamik homogener, unzusammendrückbarer, reibungsloser Flüssigkeiten und die Helmholtzschen Wirbelsätze. *Math. Z.*, 23:89–154, 1925.

[103] J. Lumley. Application of central limit theorems to turbulence problems. In M. Rosenblatt and C. Van Atta, editors, *Statistical Models and Turbulence*, pages 1–26. Springer-Verlag, 1972.

[104] G. Luo and T. Y. Hou. Potentially singular solutions of the 3D incompressible Euler equations. *PNAS*, 111:12968–1297349, 2014.

[105] V. S. L'vov, E. Podivilov, A. Pomyalov, I. Procaccia, and D. Vandembroucq. Improved shell model of turbulence. *Phys. Rev. E*, 58(2):1811, 1998.

[106] V. S. L'vov, E. Podivilov, and I. Procaccia. Hamiltonian structure of the Sabra shell model of turbulence: Exact calculation of an anomalous scaling exponent. *EPL*, 46(5):609–612, 1999.

[107] V. S. L'vov, I. Procaccia, and D. Vandembroucq. Universal scaling exponents in shell models of turbulence: viscous effects are finite-sized corrections to scaling. *Phys. Rev. Lett.*, 81(4):802, 1998.

[108] A. A. Mailybaev. Renormalization and universality of blowup in hydrodynamic flows. *Phys. Rev. E*, 85(6):066317, 2012.

[109] A. A. Mailybaev. Bifurcations of blowup in inviscid shell models of convective turbulence. *Nonlinearity*, 26:1105–1124, 2013.

[110] A. A. Mailybaev. Continuous representation for shell models of turbulence. *Nonlinearity*, 28(7):2497–2514, 2015.

[111] A. A. Mailybaev. Spontaneous stochasticity of velocity in turbulence models. *Multiscale Modeling & Simulation*, 14(1):96–112, 2016.

[112] A. A. Mailybaev. Spontaneously stochastic solutions in one-dimensional inviscid systems. *Nonlinearity*, 29(8):2238, 2016.

[113] A. J. Majda and A. L. Bertozzi. *Vorticity and Incompressible Flow*. Cambridge University Press, 2002.

[114] J. E. Marsden and T. J. R. Hughes. *Mathematical Foundations of Elasticity*. Dover, 1983.

[115] N. Masmoudi. Remarks about the inviscid limit of the Navier–Stokes system. *Communications in mathematical physics*, 270(3):777–788, 2007.

[116] F. J. McGrath. Nonstationary plane flow of viscous and ideal fluids. *Archive for Rational Mechanics and Analysis*, 27(5):329–348, 1968.

[117] T. Miyazaki, W. Kubo, Y. Shiga, T. Nakano, and T. Gotoh. Classical and quantum turbulence. *Physica D*, 239(14):1359–1366, 2010.

[118] R. E. Moore, R. B. Kearfott, and M. J. Cloud. *Introduction to Interval Analysis*, volume 110. Siam, 2009.

[119] C.-Y. Mou and P. B. Weichman. Spherical model for turbulence. *Phys. Rev. Lett.*, 70(8):1101, 1993.

[120] H. Mouri, M. Takaoka, A. Hori, and Y. Kawashima. Probability density function of turbulent velocity fluctuations. *Phys. Rev. E*, 65(5):056304, 2002.

[121] N. Nguyen van yen, M. Waidmann, R. Klein, M. Farge, and K. Schneider. Energy dissipation caused by boundary layer instability at vanishing viscosity. *Journal of Fluid Mechanics*, 849:676–717, 2018.

[122] R. Nguyen van yen, M. Farge, and K. Schneider. Energy dissipating structures produced by walls in two-dimensional flows at vanishing viscosity. *Phys. Rev. Lett.*, 106:184502, 2011.

[123] K. Ohkitani and M. Yamada. Temporal intermittency in the energy cascade process and local Lyapunov analysis in fully developed model of turbulence. *Prog. Theor. Phys.*, 81(2):329–341, 1989.

[124] H. Okamoto, T. Sakajo, and M. Wunsch. On a generalization of the Constantin–Lax–Majda equation. *Nonlinearity*, 21(10):2447, 2008.

[125] L. Onsager. Statistical hydrodynamics. *Il Nuovo Cimento*, 6:279–287, 1949.

[126] P. Orlandi. Vortex dipole rebound from a wall. *Physics of Fluids A: Fluid Dynamics*, 2(8):1429–1436, 1990.

[127] B. R. Pearson, P.-Å. Krogstad, and W. van de Water. Measurements of the turbulent energy dissipation rate. *Phys. Fluids*, 14(3):1288–1290, 2002.

[128] J. Pedlosky. *Geophysical Fluid Dynamics*. Springer, 2013.

[129] C. S. Peskin. Flow patterns around heart valves: a numerical method. *Journal of computational physics*, 10(2):252–271, 1972.

[130] C. S. Peskin. The immersed boundary method. *Acta numerica*, 11:479–517, 2002.

[131] A. Petrossian and J.-F. Pinton. Sound scattering on a turbulent, weakly heated jet. *J. Phys. II*, 7(5):801–812, 1997.

[132] D. Pierotti. Intermittency in the large-N limit of a spherical shell model for turbulence. *Europhys. Lett.*, 37(5):323, 1997.

[133] A. Pumir and E. Siggia. Collapsing solutions to the 3-D Euler equations. *Phys. Fluids A*, 2:220–241, 1990.

[134] A. Pumir and E. D. Siggia. Finite-time singularities in the axisymmetric three-dimension Euler equations. *Phys. Rev. Lett.*, 68(10):1511, 1992.

[135] J. Robinson, J. Rodrigo, and W. Sadowski. *The Three-Dimensional Navier–Stokes Equations: Classical Theory*, volume 157. Cambridge University Press, 2016.

[136] D. Ruelle. Microscopic fluctuations and turbulence. *Phys. Lett. A*, 72(2):81–82, 1979.

[137] E. P. Salathé and L. Sirovich. Boundary-value problems in compressible magnetohydrodynamics. *The Physics of Fluids*, 10(7):1477–1491, 1967.

[138] E.-W. Saw, D. Kuzzay, D. Faranda, A. Guittonneau, F. Daviaud, C. Wiertel-Gasquet, V. Padilla, and B. Dubrulle. Experimental characterization of extreme events of inertial dissipation in a turbulent swirling flow. *Nat. Commun.*, 7:12466, 2016.

[139] M. Schechter. *An Introduction to Nonlinear Analysis*. Cambridge University Press, 2004.

[140] H. Schlichting and J. Kestin. *Boundary Layer Theory*, volume 121. Springer, 1961.

[141] L. F. Shampine and M. W. Reichelt. The matlab ode suite. *SIAM J. Sci. Comput.*, 18(1):1–22, 1997.

[142] L. Sirovich. Initial and boundary value problems in dissipative gas dynamics. *The Physics of Fluids*, 10(1):24–34, 1967.

[143] L. Sirovich. Steady gasdynamic flows. *The Physics of Fluids*, 11(7):1424–1439, 1968.

[144] E. Suzuki, T. Nakano, N. Takahashi, and T. Gotoh. Energy transfer and intermittency in four-dimensional turbulence. *Phys. Fluids*, 17(8):081702, 2005.

[145] H. S. G. Swann. The convergence with vanishing viscosity of nonstationary navier-stokes flow to ideal flow in R_3. *Transactions of the American Mathematical Society*, 157:373–397, 1971.

[146] T. Tao. Finite time blowup for Lagrangian modifications of the three-dimensional Euler equation. *Ann. PDE*, 2:9, 2016.

[147] R. Temam. Local existence of C^∞ solutions of the Euler equations of incompressible perfect fluids. In *Turbulence and Navier Stokes Equations*, pages 184–194. Springer, 1976.

[148] S. Thalabard, J. Bec, and A. A. Mailybaev. From the butterfly effect to spontaneous stochasticity in singular shear flows. *Communications Physics*, 3(1):1–8, 2020.

[149] L. N. Trefethen. *Spectral methods in MATLAB*. SIAM, 2000.

[150] C. A. Truesdell and R. Toupin. *The Classical Field Theories*. Handbuch der Physik III/1. Springer-Verlag, 1960.

[151] C. Uhlig and J. Eggers. Singularities in cascade models of the Euler equation. *Z. Phys. B Con. Mat.*, 103(1):69–78, 1997.

[152] N. Valade, S. Thalabard, and J. Bec. Anomalous dissipation and spontaneous stochasticity in deterministic surface quasi-geostrophic flow. *arXiv:2210.12366*, 2022.

[153] A. F. Vasseur and M. Vishik. Blow-up solutions to 3D Euler are hydrodynamically unstable. *Comm. Math. Phys.*, 378(1):557–568, 2020.

[154] M. K. Verma, A. Kumar, P. Kumar, S. Barman, A. G. Chatterjee, R. Samtaney, and R. A. Stepanov. Energy spectra and fluxes in dissipation range of turbulent and laminar flows. *Fluid Dynamics*, 53(6):862–873, 2018.

[155] T. Yamamoto, H. Shimizu, T. Inoshita, T. Nakano, and T. Gotoh. Local flow structure of turbulence in three, four, and five dimensions. *Phys. Rev. E*, 86(4):046320, 2012.

[156] V. I. Yudovich. Nichtstationäre Strömung einer idealen inkompressiblen Flüssigkeit. *Zh. Vychisl. Mat. Mat. Fiz.*, 3:1032–1066, 1963.

[157] V. E. Zakharov and E. A. Kuznetsov. Hamiltonian formalism for nonlinear waves. *Phys.-Uspekhi*, 40(11):1087–1116, 1997.